

Åsmund Eek

Formation Control of Two Interconnected Underactuated Unmanned Surface Vessels Under Influence of Constant Ocean Currents

Master's thesis in Cybernetics and Robotics

Supervisor: Professor Kristin Y. Pettersen

June 2020



Åsmund Eek

Formation Control of Two Interconnected Underactuated Unmanned Surface Vessels Under Influence of Constant Ocean Currents

Master's thesis in Cybernetics and Robotics
Supervisor: Professor Kristin Y. Pettersen
June 2020

Norwegian University of Science and Technology
Faculty of Information Technology and Electrical Engineering
Department of Engineering Cybernetics

Problem description

The Norwegian Defense Research Establishment (Forsvarets forskningsinstitutt, FFI) is currently considering the use of unmanned surface vessels (USVs) for use in various military applications. Two test platforms, Odin and Frigg, have been developed to study the use of this technology in maritime mine countermeasures (MMCM) operations and as support vessels for autonomous underwater vehicles. The USVs will require a high degree of autonomy, which necessitates robust and inherently safe control algorithms.

In the future MMCM concept, USVs are required to operate together in mine sweeping operations. In these operations, two USVs will cooperate in towing a closed-loop influence sweep, with the intent of triggering any potential mines in an area by simulating a larger ship moving through the water. The USVs are physically connected by the mine sweep cables, and must keep a more or less fixed inter-vessel distance in order to obtain the desired cable positioning.

Specifically, the USVs must operate in such a way that:

- The mine sweep cables follow a predetermined path made up by waypoints
- The USVs keep a constant cross-track distance on either side of the path
- The USVs maintain a constant speed along the path
- Collisions within the formation and with other vessels are avoided
- The formation is stable in the presence of environmental disturbances
- The formation is robust to changes in vessel dynamics caused by the mine sweep cables, which are heavy

A robust formation control algorithm for USVs is crucial in such operations. Not only is the operation safer when the vessels are unmanned and autonomous, it is also very difficult to maintain the desired formation over time when operating the

vessels manually. This thesis will investigate the use of one such formation control algorithm for two interconnected, underactuated USVs (such as Odin and Frigg) in the presence of ocean currents.

Proposed subtasks for this thesis include:

- Perform a literature study in the field of formation control of underactuated marine surface vessels, with particular focus on cases where the vessels are physically interconnected
- Derive a mathematical model of the system, including cable dynamics and environmental disturbances
- Make a well-reasoned choice of formation control algorithm based on the literature study and do potential alterations for use of the algorithm in mine sweeping operations with USVs
- Perform a mathematical analysis of the system, including stability analysis of relevant parts of the algorithm
- Implement the proposed formation control algorithm in a simulated environment including the cable dynamics and environmental disturbances
- Implement the proposed formation control algorithm in a ROS environment and perform full-scale experiments with Odin and Frigg
- Evaluate the performance of the implemented formation control algorithm based on the results from simulated and real-world experiments

The thesis will build upon preliminary work performed in a previous project assignment.

Abstract

In this thesis, a possible formation control method is proposed for the next generation of future Norwegian unmanned Maritime Mine Counter Measures (MMCM) for autonomous mine-sweeps, which is currently researched by the Norwegian Defence Research Establishment (FFI). Having the capability of performing autonomous mine-sweeps reduces the risk for personnel, potentially saving human lives.

A formation control method based on the Null-Space-Based Behavior Control (NSB) principle is proposed for formations of two interconnected underactuated unmanned surface vessels (USVs) in the presence of constant irrotational ocean currents. Inspired by Line-Of-Sight (LOS) ideas, the traditional Closed Loop Inverse Kinematics (CLIK) barycenter task is replaced by a LOS path following method for the barycenter. Two theorems are presented where it is proven that the closed-loop formation and barycenter tasks are UGES and USGES, respectively, under certain conditions. By treating the cable as a state dependent disturbance, the robustness properties of both tasks are then investigated to ensure they remain bounded when connecting the cable.

A 3-DOF simulation model of a floating cable is presented, where the hydrodynamic drag model is extended to incorporate the effects of ocean currents, and verified against experimental data. The developed method is then implemented and simulated, both with and without the cable. In the simulations, the task errors converge to zero for straight-line paths, while they remain bounded during turns.

Finally, the NSB method is implemented in C++/ROS and integrated into the existing autonomous systems of the development vessels Odin and Frigg by FFI. Full-scale experiments, without the sweep, at sea, are then performed to verify the proposed formation control method for the intended application. The tests show promising results, but a steady-state error is observed for the barycenter task's cross-track error. Based on the promising results, further experiments are planned by FFI using the proposed NSB method and the sweep.

Sammendrag

I denne oppgaven blir en mulig formasjonsstyringsmetode foreslått for autonom minerydding for den neste generasjonen av mineryddere for Sjøforsvaret, som for øyeblikket er under utvikling av Forsvarets Forskningsinstitutt (FFI). Ved å utvikle autonome mineryddingsfartøy kan personell fjernes fra risikoområder, som kan spare menneskeliv.

En formasjonsstyringsmetode basert på Null-Space-Based Behavior Control (NSB)-prinsippet blir foreslått for formasjoner av to sammenkoblede underaktuerte ubemannede overflatefarkoster (USV-er) under forstyrrelse av havstrømmer. Inspirert av idéer fra Line-Of-Sight (LOS), blir den tradisjonelle Closed Loop Inverse Kinematics (CLIK) barycenteroppgaven erstattet av en LOS-metode for banefølgning av barycenteret. To teoremer blir presentert hvor det bevises at de lukkede sløyfene for henholdsvis formasjons- og barycenteroppgaven er UGES og USGES under visse betingelser. Videre, ved å behandle kabelen som en tilstandsvarierende forstyrrelse, undersøkes robusthetsegenskapene til begge oppgavene for å sikre at de forblir stabile.

En 3-DOF simuleringsmodell av slepet blir presentert, med en utvidet modell for den hydrodynamiske motstanden for å inkludere havstrømmer, og verifisert mot eksperimentell data. Den foreslåtte metoden blir så implementert og simulert, både med, og uten, kabel, hvor oppgavefeilene konvergerer til null for rette linjer, og forblir avgrenset under svinger.

Til slutt blir NSB-metoden implementert i C++/ROS og integrert inn i de eksisterende autonome systemene til utviklingsfarkostene Odin og Frigg fra FFI. Fullskala eksperimenter til sjøs blir så utført for å verifisere den foreslåtte metoden for det tiltenkte bruksområdet. Eksperimentene viser lovende resultater, men et stasjonæravvik blir observert for cross-track-feilen til barycenteroppgaven. På bakgrunn av de lovende resultatene er videre forsøk med den foreslåtte NSB-metoden og det faktiske slepet planlagt av FFI.

Contents

Problem description	i
Abstract	iii
Sammendrag	iv
Table of Contents	v
List of Abbreviations	viii
List of Figures	x
Preface	xii
1 Introduction	1
1.1 Motivation	1
1.2 Previous Work	2
1.3 Objectives	5
1.4 Contributions	6
1.5 Outline	7
2 Vessel Modeling	9
2.1 Reference Frames	9
2.2 Equations of Motion	10
2.2.1 System Inertia Matrix	11
2.2.2 Coriolis and Centripetal Matrix	11
2.2.3 Damping	12
2.3 Waterjet Dynamics	12
2.3.1 Linearization of Waterjet Dynamics	16
2.4 Maneuvering Controllers	19

2.4.1	Surge Controller	19
2.4.2	Heading Controller	20
3	Cable Modeling	22
3.1	Introduction	22
3.2	Cable dynamics	24
3.2.1	Kinematics	25
3.2.2	Hydrodynamic drag forces	26
3.2.3	Generalized forces	28
3.2.4	Lagrange's equations of motion	28
3.3	Solving the DAE system	29
3.3.1	Practical implementation	34
3.4	Connection with vessel	35
3.4.1	Cable forces	35
3.4.2	PVA of cable end points	36
3.5	Model verification	37
3.5.1	Ocean currents	37
3.5.2	Drag coefficients	39
4	Formation Control	43
4.1	Introduction	43
4.2	NSB mathematics	45
4.2.1	Merging multiple tasks	47
4.3	Maneuvering Controller interface	48
4.4	Tasks	49
4.4.1	Obstacle Avoidance	49
4.4.2	Formation	50
4.4.3	Barycenter	52
4.4.4	Stability of merged formation and barycenter tasks	60
4.5	Closed-loop analysis	61
4.5.1	Formation task	63
4.5.2	Barycenter task	67
4.6	Robustness against non-vanishing perturbations	71
4.7	Path generation	74
5	Simulations	77
5.1	Ideal case	77

5.1.1	Only barycenter task active	78
5.1.2	All tasks active	82
5.2	Realistic vessel model without cable	86
5.2.1	Sinusoidal path	87
5.2.2	Sweep	91
5.3	Realistic vessel model with cable	95
5.3.1	Sinusoidal path	95
5.3.2	Sweep	99
5.4	Discussion	103
6	Experiments	105
6.1	Introduction	105
6.2	Implementation	106
6.2.1	Available sensor measurements	107
6.3	Sweep	108
6.4	Discussion	114
7	Conclusion and Future Work	117
7.1	Conclusion	117
7.2	Further work	118
	References	121
	Appendices	127
A	Stability proofs	129
A.1	Proof of Lemma 4.2	129
A.2	Proof of Lemma 4.3	131
A.2.1	Importance of the choice of lookahead distance in Eq. (4.38)	135
A.3	Proof of Lemma 4.4	138
B	Derivations of expressions	143
B.1	Derivations of Eq. (4.30)	143
B.2	Derivations of Eq. (4.41)	145
B.3	Derivations of Eq. (4.64)	147
C	Vessel model expressions	150

List of Abbreviations

AUV Autonomous Underwater Vehicle

CG Center of Gravity

CLIK Closed Loop Inverse Kinematics

CO Center of Origin

DAE Differential Algebraic Equation

DOF Degree of Freedom

EAC Euler Angle Cable

FFI Norwegian Defence Research Establishment (Forsvarets Forskningsinstitut)

GES Globally Exponentially Stable

GNSS Global Navigation Satellite System

ILOS Integral Line-of-Sight

IMU Inertial Measurement Unit

INS Inertial Navigation System

LCS Layered Control System

LFC Lyapunov Function Candidate

LOS Line-of-Sight

MDS Mass-Damper-Spring system

MMCM Maritime Mine Counter Measures

MPC Model Predictive Control

MSC Motor Schema Control

NED North East Down

NSB Null-Space-Based

ODE Ordinary Differential Equation

PCHIP Piecewise Cubic Hermite Interpolation Polynomial

PDE Partial Differential Equation

PVA Position Velocity Acceleration

RBB Rigid Buoyancy Boat

RBC Rigid Bar Cable

ROS Robot Operating System

RPM Revolutions per Minute

UGAS Uniform Global Asymptotic Stability

UGES Uniform Global Exponential Stability

UGS Uniform Global Stability

ULES Uniform Local Exponential Stability

USGES Uniform Semi-Global Exponential Stability

USV Unmanned Surface Vessel

List of Figures

1.1	The Odin and Frigg USVs considered in this thesis.	1
1.2	Illustration of Odin and Frigg performing a mine-sweep operation.	2
2.1	System overview of waterjet model	13
2.2	Waterjet thrust as a function of relative surge speed and throttle demand.	14
2.3	Linearized waterjet dynamics vs actual dynamics.	18
3.1	Discrete model visualization	24
3.2	Illustration of connection between cable and vessel	35
3.3	Cable affected by constant ocean currents.	38
3.4	Comparison of simulation vs. experiments.	42
4.1	Overview of centralized NSB guidance system	45
4.2	Geometric interpretation of combining velocities through null-space projections	48
4.3	Definition of the path and path following errors.	53
4.4	Illustration of the LOS guidance law for path following for the barycenter.	57
4.5	Waypoint interpolation methods	75
5.1	Path following of the desired sinusiodal path with only the barycenter task active.	79
5.2	NSB errors of the desired sinusiodal path with only the barycenter task active.	80
5.3	Desired vs. actual heading (top), surge (middle) and sway (bottom) of the desired sinusiodal path with only the barycenter task active.	81
5.4	Path following of the desired sinusiodal path with all tasks active.	83
5.5	NSB errors of the desired sinusiodal path with all tasks active.	84

5.6	Desired vs. actual heading (top), surge (middle) and sway (bottom) of the desired sinusoidal path with all tasks active.	85
5.7	Path following of the desired sinusoidal path without cable.	88
5.8	NSB errors of the desired sinusoidal path without cable.	89
5.9	Desired vs. actual heading (top), surge (middle) and sway (bottom) of the desired sinusoidal path without cable.	90
5.10	Path following of a path representing a mine-sweep without cable.	92
5.11	NSB errors of a path representing a mine-sweep without cable.	93
5.12	Desired vs. actual heading (top), surge (middle) and sway (bottom) of a path representing a mine-sweep without cable.	94
5.13	Path following of the desired sinusoidal path with the cable.	96
5.14	NSB errors of the desired sinusoidal path with the cable.	97
5.15	Desired vs. actual heading (top), surge (middle) and sway (bottom) of the desired sinusoidal path with the cable.	98
5.16	Path following of a path representing a mine-sweep with the cable.	100
5.17	NSB errors of a path representing a mine-sweep with the cable.	101
5.18	Desired vs. actual heading (top), surge (middle) and sway (bottom) of a path representing a mine-sweep with the cable.	102
6.1	Photo of Odin and Frigg during the experiments	106
6.2	Overview of implemented decentralized NSB guidance system.	107
6.3	Path following of a path representing a mine-sweep.	110
6.4	Online calculated NSB errors from Odin of a path representing a mine-sweep.	111
6.5	Online calculated NSB errors from Frigg of a path representing a mine-sweep.	112
6.6	Desired vs. actual heading (top), surge (middle) and sway (bottom) of a path representing a mine-sweep.	113
6.7	The simulated vessels and desired path with a PD-controller for heading	115
6.8	NSB errors with a PD-controller for heading	116

Preface

This thesis is submitted in partial fulfillment of the requirements for the degree of Master of Science in Cybernetics and Robotics at the Norwegian University of Science and Technology (NTNU). The work presented in this thesis has been carried out under the supervision of Professor Kristin Y. Pettersen at the Department of Engineering Cybernetics, NTNU, and co-supervisors Else-Line M. Ruud and Dr. Thomas R. Krogstad at the Norwegian Defence Research Establishment (FFI).

This thesis is a continuation of the author's specialization project Eek (2019) conducted during the fall of 2019. Since the specialization project is not published, some sections are either fully, or partially re-used throughout this thesis. A complete list of the sections included from the specialization project is given below:

- Section Section 1.1.
- Parts of Sections 1.2–1.3.
- Most of Chapter 2 (reformulated to combine Chapters 2 and 3 from the specialization project).
- Parts of Sections 4.1–4.3.
- Parts of Sections 4.4.1–4.4.2.
- Parts of Section 4.7.

This thesis has been conducted in collaboration with FFI, and I have received multiple tools from them during this thesis. This includes the MATLAB/Simulink model of *Odin* used to test the formation control methods, which was extended to include the effect of ocean currents and implementation of new maneuvering controllers during the specialization project. Additionally, I received a report describing the current guidance and control system of *Odin*. The waterjet model described in Section 2.3 is taken from that report. In the work of implementing the formation

control method in C++ and ROS, I received a docker image with compiled binaries of the current autonomous control systems and a simulator of Odin and Frigg. This allowed me to test my implementation beforehand, making the process of performing the experiments surprisingly smooth.

The script used to derive the equations of motion of the model presented in Chapter 3 is based on the publicly available code Bhattacharya (2020a). The author of this thesis then added the extended hydrodynamic drag model and the possibility to export the cable model to MATLAB.

Unless otherwise stated, all figures and illustrations have been created by the author.

Acknowledgment

First of all, I would like to thank my supervisors for all of their valuable guidance and feedback during the last year. They have always believed in me and encouraged me to pursue my ideas. I am grateful to Kristin for answering my many questions during the theoretical work, and guide me through the world of Lyapunov. I am also thankful to Else-Line and Thomas for our biweekly meetings, which I have greatly enjoyed.

I would also like to thank Dr. Dennis J.W. Belleter for his invaluable support in the theoretical analysis of the closed-loop barycenter task dynamics. His clarifications and answers, related to the proofs of his article were truly helpful, and I could not have finished the proof of Lemmas 4.3–4.4 without him.

During the experiments, I had two fantastic days at FFI in Horten. Seeing the vessels drive autonomously at the first attempt was worth the countless hours I have dedicated to this project over the last year. Again, I would like to thank Else-Line for her assistance with managing and updating FFI's side of the interface between my node and the autonomous systems of Odin and Frigg. I would also like to thank Jarle Sandrib, Geir Lofsberg, and Fredrik Hermansen at FFI for their valuable help and assistance during the experiments.

Finally, I would like to thank my family and friends for their always great support.

Åsmund Eek
Nannestad, June 2020

1 | Introduction

1.1 Motivation

In 2015, the Norwegian Ministry of Defence initiated the startup of a conceptual phase for future marine systems for minesweeping and clearance. The next generation of Maritime Mine Counter Measures (MMCM) capability will be based upon small crewless surface vessels that can be deployed from a crewed ship outside the mined area, meaning the operation can be performed at a safe distance, reducing the risk for personnel, see Midtgaard and Nakjem (2016). To achieve this, FFI has acquired the vessels *Odin* and *Frigg* as a development platform, see Fig. 1.1.

Odin and *Frigg* are two 10.5 m long vessels powered by a pair of Hamilton waterjets and equipped with sensors for autonomous operation. As they are equipped with a dual waterjet system, they are capable of being fully actuated in three Degrees Of Freedom (DOF): surge, sway, and yaw. However, in the applications considered in this thesis, both waterjets are linked together, rendering the system underactuated with only control forces and moments in surge and yaw. Linking the waterjets together at maneuvering speeds is common as it is more energy-efficient.



(a) *Odin*.

(b) *Frigg*.

Figure 1.1: The *Odin* and *Frigg* USVs considered in this thesis. Courtesy of FFI.

The FFI USV systems Odin and Frigg will operate in minesweeping operations. In these operations, the vessels will tow influence equipment to trigger possible mines in the operational area. The minesweeping equipment can be very heavy or require a large special displacement. It is therefore beneficial for the vessels to cooperate while towing, illustrated in Fig. 1.2. A formation control algorithm is thus required in cases where there is a physical interconnection between the vessels.

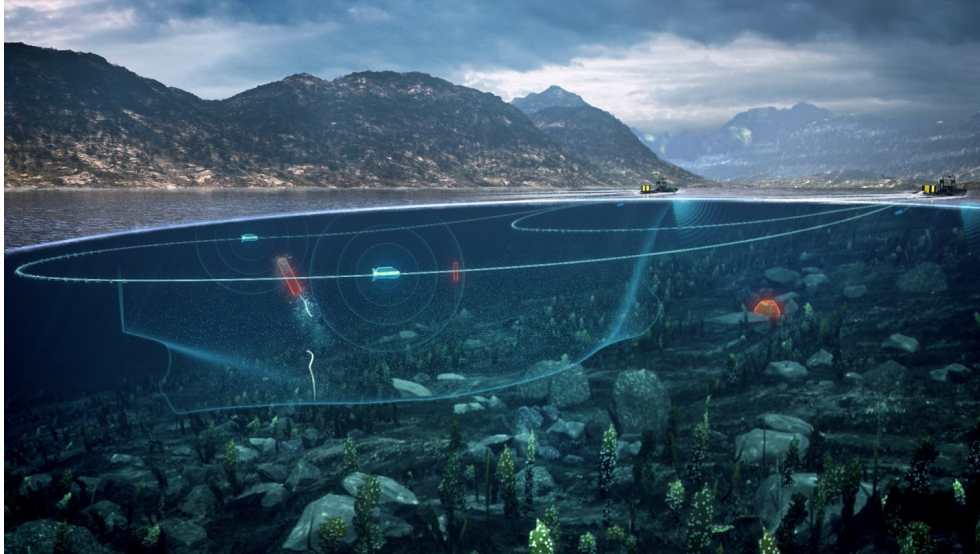


Figure 1.2: Illustration of Odin and Frigg performing a mine-sweep operation. Courtesy of FFI.

1.2 Previous Work

An approach to the formation control problem is presented in Ihle, Jouffroy and Fossen (2006), which introduces a solution based on a set of virtual constraint functions for inter-vessel distances and Lagrangian multipliers. By including feedback from the constraints, the desired formation is obtained. In Ihle, Arcaç and Fossen (2006), a passivity-based method for synchronous path following is presented where the passivity properties of the closed-loop system are preserved. Moreover, in Skjetne et al. (2002), a nonlinear formation control law is presented. Each vessel's position is defined relative to a formation reference point, which should follow the desired path. However, all these papers consider fully actuated vehicles, meaning they cannot immediately be applied to underactuated marine vessels, which is the area of focus in this thesis.

In Kyrkjebø (2007), a leader-follower approach for surface vessels using a virtual vessel concept is presented, while in Lapierre et al. (2003), a leader-follower method for two underactuated underwater vehicles is presented. Here, the follower adapts its speed based on the leader position to obtain the desired formation. The topic of leader-follower methods is also discussed in, e.g., Breivik et al. (2008), where a guided leader-follower approach inspired by concepts from integrator backstepping and cascade theory is presented. Furthermore, in Belleter (2016), constant bearing guidance is used for the follower to track the leader. However, leader-follower methods suffer from the fact that communication is unidirectional, meaning the leader will not adapt its speed according to the follower.

The problem of straight-line path following formations of marine vessels is studied in Børhaug et al. (2006, 2011); Belleter and Pettersen (2014). In Børhaug et al. (2006, 2011), the case without ocean currents is investigated, and an UGAS and ULES decentralized control strategy is proposed. The desired formation is obtained through each vessel in the formation using an ILOS guidance law to follow the desired path, while the desired along-path distance between each vessel is obtained with a nonlinear velocity control law. The topic is further studied in Belleter and Pettersen (2014), which combines the results from Børhaug et al. (2008); Caharija et al. (2012) with Børhaug et al. (2011) to create a formation control law allowing straight-line path following for formations of marine vessels under the influence of constant ocean currents. However, all of these methods are restricted to straight-line paths, and cannot be applied for curved paths.

A behavioral-based control approach using the Null-Space-Based (NSB) control scheme is presented in Arrichiello et al. (2006a,b). Here, a platoon of underactuated marine vessels is considered. This centralized guidance system decomposes the control objective into different tasks, where each task is assigned a priority, which is solved independently of each other using a Closed Loop Inverse Kinematics (CLIK) algorithm. The solutions of each task are then combined by projecting the solution of one task into the null-space of the higher priority task. Similar approaches are widely studied for other autonomous vehicles, such as mobile robotics applications, see Antonelli and Chiaverini (2003); Antonelli et al. (2005); Antonelli and Chiaverini (2006).

Although the topic of formation control, in general, is well-studied, the scenario when the vessels are physically interconnected is less studied.

The task of using autonomous vessels connected with a boom for automatic oil spill confinement is studied in Giron-Sierra et al. (2014, 2015). In Giron-Sierra

et al. (2014), experimental results are obtained with two scaled USVs towing a boom. Further full-scale experiments with two 2.4 m USVs was then performed in Giron-Sierra et al. (2015). However, both these papers utilized a leader-follower approach, which is undesirable due to the unidirectional communication.

In Pereda et al. (2011), the NSB method is considered for the same application as above - automatic oil spill confinement. Although the paper considers the formation control of two interconnected vessels, the boom and the actual formation control simulations are decoupled during the simulation studies as the boom simulations are computationally intensive. Hence, the formation control method was never actually tested in an interconnected scenario. Although this paper originates from the same research group as Giron-Sierra et al. (2014, 2015), no experimental results with the NSB method was, to the author's knowledge, performed, for unknown reasons.

The NSB method is further utilized in Arrichiello et al. (2010, 2011) for autonomous caging and transporting purposes. Experimental results were obtained with two 2.1 m long USVs connected on a floating rope. However, in this paper, no rigid formation task is selected, allowing the inter-vessel distance to fluctuate between a minimum and maximum threshold, which is not desirable during a mine-sweep.

Related to the experiments Arrichiello et al. (2010, 2011) is the paper Bhattacharya et al. (2011), which develops a model of a floating rope in 3-DOF. Here, each endpoint of the rope is assumed connected to a vessel. However, during the simulation of the rope dynamics, predetermined trajectories of each vessel are used. Hence, the simulations fail to capture the closed-loop response with a formation control method with the rope.

Considering the actual application of mine-sweep with Odin and Frigg, some research has been performed by FFI. Although the work is not yet published, a simple leader-follower method has been implemented and tested, where the leader was using an ILOS method for straight-line path following. However, as mentioned before, the unidirectional communications result in suboptimal performance, especially during turns, where the leader is unable to adapt its speed according to the follower. Therefore, the need for a cooperative method has been concluded by FFI, setting the background of this thesis.

During the author's specialization project Eek (2019) in the fall of 2019, the performance of the ILOS from Belleter and Pettersen (2014) and a NSB method inspired from Pereda et al. (2011), were compared for straight-line path following for formations of two USVs in the presence of ocean currents. Although no physical

connection between the vessels was considered here, the work was still useful to determine which control method was most suited for the application. The report concluded that the NSB method is more suited due to its ability to maintain the inter-vessel distance, which is crucial when the vessels are physically connected. However, notably slower convergence to the desired path was achieved by the NSB than the ILOS method. Hence, suggestions were made to improve the transient phase by replacing the traditional Closed Loop Inverse Kinematics (CLIK) with a LOS method for the barycenter task, for which, a possible approach is presented in this thesis.

1.3 Objectives

In particular, this thesis will address the coordination between the two vessels and how they should maneuver to follow the desired path while maintaining an inter-vessel formation. Furthermore, the vessels will be connected by a physical cable, representing the sweep.

During a mine-sweep, both vessels should make the barycenter, which is the centroid of the two vessels, follow a predetermined path, denoted by waypoints, while driving with a constant along-path speed. Simultaneously, the vessels should keep a rigid formation perpendicular to the path, such that the inter-vessel distance remains constant. Moreover, the cable is connected along the centerline, at the stern, of each vessel.

On request from FFI, all numerical values of the different parameters for Odin and Frigg are omitted in this thesis. As a result, only the structure of the various matrices and parameters are given in Chapter 2 without any numerical values. The same applies to the waterjet model, where some of the figures are plotted without numerical values. For the cable model in Chapter 3, only the total number of rigid links used in the simulation model are given, while no numerical values for the total mass, length, and drag coefficients are given for the same reason. Additionally, the desired inter-vessel distance for the formation task function value is not given in Chapter 5 and Chapter 6.

Finally, it should be noted that all parameters used for the overall objectives, such as inter-vessel distance, along-path speed, and cable length, do not necessarily reflect the values used during the actual mine-sweep application, and is chosen in the thesis to test the methods in similar scenarios.

1.4 Contributions

The main contributions of the work presented in this thesis are as follows:

- Research of previous work on the topic of formation control of underactuated marine vessels.
- Extending the hydrodynamic drag model from Bhattacharya et al. (2011) to include effects from ocean currents.
- Using the script from Bhattacharya (2020a) as a base, the improved cable model was generated, and a method to export the model to MATLAB was created.
- Verification of the new hydrodynamic drag model and the resulting model against experimental data.
- Inspired by Belleter et al. (2019), a novel approach using ideas from traditional LOS methods for the barycenter task is proposed.
- Using the vessel model and maneuvering controllers proposed in Moe et al. (2016), the stability properties of both the formation and barycenter tasks, without the cable, are investigated in detail, and two theorems are presented.
- Investigating the robustness properties against non-vanishing perturbations of the NSB tasks. As the cable may be seen as a disturbance, this is important to understand how the addition of the cable may affect the NSB performance.
- Implementation of the proposed formation method in MATLAB/Simulink.
- A simulation study evaluating the performance of the proposed formation method in the following scenarios: (1) ideal case with the vessel model and controllers from Moe et al. (2016), (2) using the vessel model in Chapter 2 without the cable and (3) using the vessel model in Chapter 2 with the cable.
- Implementation of the proposed formation method in C++. The method was then integrated into the existing autonomous systems of Odin and Frigg by FFI using ROS.
- Evaluation and verification of the proposed formation control method through full-scale experiments on board Odin and Frigg.

1.5 Outline

This thesis is divided into seven chapters and three appendices, described below:

Chapter 2 presents the mathematical model used to describe the dynamics of marine vessels, along with the nonlinear actuator model of the waterjets, which is equipped by Odin. Additionally, a linearized model of the waterjet dynamics is derived. Finally, the maneuvering controllers for surge and heading is presented.

Chapter 3 presents the mathematical model used to describe the dynamics of the cable. First, the equation of motions is derived using Lagrangian mechanics, including an extended hydrodynamic model capturing the effects of ocean currents. Then, the implementation aspect of how to solve the resulting DAE system in MATLAB is discussed. Next, the equations used to connect the cable with the vessels are presented. Finally, the resulting model is verified against experimental data.

Chapter 4 first gives an overview of the background of behavioral methods, and the NSB mathematics is given. Then, the details of the three tasks constituting the NSB method are presented, including a novel LOS path following approach for the barycenter task. Next, the closed-loop stability of both the formation and barycenter tasks, along with the robustness properties against non-vanishing perturbations is investigated. Finally, the interpolation method using to generate the path is presented.

Chapter 5 contains several simulation studies to evaluate the NSB method under different scenarios. First, the theoretical stability analysis is illustrated using the vessel model and controllers from Moe et al. (2016). Then, more scenarios are evaluated using the vessel model and controllers from Chapter 2 both with and without the cable. Finally, the simulation results are discussed.

Chapter 6 starts by discussing the C++ implementation of the NSB method, and the ROS interface with the existing autonomous system on board Odin and Frigg. Then, the results from full-scale experiments are presented. Finally, the experimental results are discussed.

Chapter 7 gives a conclusion drawn from the results and suggests further work.

Appendix A presents the theoretical proofs of Lemmas 4.2–4.4, which is not included in the main body for readability.

Appendix B contains detailed derivations of various mathematical expressions that are left out of the main body for readability.

Appendix C gives the expressions for the vessel model from Moe et al. (2016).

2 | Vessel Modeling

The purpose of this chapter is to introduce the mathematical modeling that describes the equations of motion of an underactuated marine vessel. This is beneficial, as it allows accurate replication of the actual vessel behavior, making it possible to see how methods will perform in real-life by simulations. Furthermore, having a mathematical model of the system is advantageous during the design and tuning of maneuvering controllers.

The model considered describes the dynamics of a displacement vessel, meaning it will only be valid for low-speed applications, as Odin is a Rigid Buoyancy Boat (RBB). This further implies that for high-speed applications, the dynamics changes towards those of a planing vessel, rendering this model invalid.

First, the notation and reference frames used throughout this thesis are given. Next, the 3-DOF equations of motion are stated. Then, the equations describing the waterjet dynamics are presented. Finally, the maneuvering controllers used for the simulation model of Odin is presented. All notation and results in this chapter, except Section 2.3 and Section 2.4, are based on Fossen (2011) unless stated otherwise.

On request from FFI, all numerical values of the different parameters for Odin are omitted. Consequently, only the structure of the various matrices and parameters are given in this chapter without any numerical values.

The theory presented in this chapter, except the addition of the reaction forces in Eq. (2.1b), was initially written in (Eek; 2019, Chapters 2 and 3) and restated here for completeness.

2.1 Reference Frames

In this section the reference frames used throughout this thesis to analyze the 3-DOF motion of a marine vessel are presented.

NED The north-east-down (NED) coordinate system $\{n\} = (x_n, y_n, z_n)$ is located

with the origin o_n at a given longitude and latitude. It is defined as the tangent plane on the Earth's surface where the x-axis points towards the North, y-axis towards the East, while the z-axis points down. When operating in a local area, with an approximately constant longitude and latitude, the frame can be assumed inertial, and Newton's laws still apply.

BODY The body-fixed coordinate system $\{b\} = (x_b, y_b, z_b)$ is fixed with the origin o_b in the vessel's Center of Origin (CO) and hence moves along with the vessel. In this thesis, the Center of Origin is chosen to coincide with the Center of Gravity (CG). Each of the axes, defined as positive forward, starboard, and downward, coincides with the inertia's principal axes.

FLOW The flow coordinate system $\{\text{flow}\} = (x_{\text{flow}}, y_{\text{flow}}, z_{\text{flow}})$ is defined as a rotation of $\{b\}$ such that x_{flow} points directly into the relative freestream flow. Due to its convenience, it is often used for calculating hydrodynamic forces.

CABLE The body-fixed coordinate system $\{c\} = (x_c, y_c, z_c)$ is fixed at the point C where the cable is attached to the vessel, with its axes defined parallel to $\{b\}$. When calculating the forces applied from the cable on the vessel, they will be given in this frame.

2.2 Equations of Motion

This section will present the equations of motion used to describe the dynamics of a marine vessel in 3-DOF, expressed in CG. As Odin is a RBB, its dynamics change from low to high speeds. As a result, the model presented here will only be valid for low-speed applications where Odin can be considered a displacement vessel.

According to Fossen (2011), the rigid-body dynamics of a marine vessel under the influence of irrotational constant ocean current can be expressed as

$$\dot{\eta}^n = \mathbf{R}_{z,\psi} \mathbf{v}_r^b + \mathbf{V}_c \quad (2.1a)$$

$$\mathbf{M} \dot{\mathbf{v}}_r^b + \mathbf{C}(\mathbf{v}_r^b) \mathbf{v}_r^b + \mathbf{D}(\mathbf{v}_r^b) \mathbf{v}_r^b = \boldsymbol{\tau}_{\text{env}}^b + \boldsymbol{\tau}_{\text{cable}}^b + \boldsymbol{\tau}^b, \quad (2.1b)$$

where $\mathbf{R}_{z,\psi} \in \mathbb{R}^{3 \times 3}$ is the rotation matrix from $\{b\}$ to $\{n\}$ which in 3-DOF is equal to the principal rotation about the z-axis, $\mathbf{V}_c \in \mathbb{R}^3$ the ocean currents, $\mathbf{M} \in \mathbb{R}^{3 \times 3}$ the system inertia matrix, $\mathbf{C}(\mathbf{v}_r^b) \in \mathbb{R}^{3 \times 3}$ the rigid-body Coriolis and centripetal matrix including added mass due to the rotation of $\{b\}$ about $\{n\}$, $\mathbf{D}(\mathbf{v}_r^b) \in \mathbb{R}^{3 \times 3}$ a

damping matrix containing both linear potential damping and nonlinear damping terms, $\boldsymbol{\tau}_{\text{env}} \in \mathbb{R}^3$ are disturbances caused by environmental forces such as ocean current, $\boldsymbol{\tau}_{\text{cable}} \in \mathbb{R}^3$ are the reaction forces exerted by the cable on the vessel caused by the vessels towing the cable and $\mathbf{v}_r^b \in \mathbb{R}^3$ the relative velocity vector in $\{b\}$.

Assumption 2.1. *The ocean current in the inertial frame is assumed to be constant and irrotational, i.e. $\mathbf{V}_c \triangleq [V_x \ V_y \ 0]^T$. Furthermore, there exists a constant $V_{\max} > 0$ such that $\|\mathbf{V}_c\| = \sqrt{V_x^2 + V_y^2} < V_{\max}$, i.e. the ocean current is bounded.*

2.2.1 System Inertia Matrix

The system inertia matrix, is given as the sum of the rigid-body mass matrix and hydrodynamic added mass

$$\mathbf{M} = \mathbf{M}_{\text{RB}} + \mathbf{M}_{\text{A}}, \quad (2.2)$$

given by

$$\mathbf{M}_{\text{RB}} = \begin{bmatrix} m & 0 & 0 \\ 0 & m & 0 \\ 0 & 0 & I_z \end{bmatrix}, \quad \mathbf{M}_{\text{A}} = \begin{bmatrix} -X_{\dot{u}} & 0 & 0 \\ 0 & -Y_{\dot{v}} & -Y_{\dot{r}} \\ 0 & -N_{\dot{v}} & -N_{\dot{r}} \end{bmatrix}, \quad (2.3)$$

where I_z is the moment of inertia about the z-axis.

2.2.2 Coriolis and Centripetal Matrix

The Coriolis and centripetal matrix, can be expressed as a sum of rigid-body and hydrodynamic terms, where the rigid-body part can be expressed using a Lagrangian parameterization Fossen (2011)

$$\mathbf{C}_{\text{RB}}(\mathbf{v}_r) = \begin{bmatrix} 0 & 0 & -mv_r \\ 0 & 0 & mu_r \\ mv_r & -mu_r & 0 \end{bmatrix} \quad (2.4a)$$

$$\mathbf{C}_{\text{A}}(\mathbf{v}_r) = \begin{bmatrix} 0 & 0 & Y_{\dot{v}}v_r + Y_{\dot{r}}r \\ 0 & 0 & -X_{\dot{u}}u_r \\ -Y_{\dot{v}}v_r - Y_{\dot{r}}r & X_{\dot{u}}u_r & 0 \end{bmatrix}. \quad (2.4b)$$

2.2.3 Damping

The total damping matrix $\mathbf{D}(\mathbf{v}_r)$, consists of a sum of linear and nonlinear damping terms

$$\mathbf{D}(\mathbf{v}_r) = \mathbf{D} + \mathbf{D}_N(\mathbf{v}_r). \quad (2.5)$$

The linear damping terms \mathbf{D} are dominating at low velocities and are present due to potential damping and possible skin friction, while the nonlinear terms $\mathbf{D}_N(\mathbf{v}_r)$ are modelled as quadratic terms and are due to viscous forces and wave drift, see Fossen (2011)

$$\mathbf{D} = \begin{bmatrix} -X_u & 0 & 0 \\ 0 & -Y_v & -Y_r \\ 0 & -N_v & -N_r \end{bmatrix} \quad (2.6a)$$

$$\mathbf{D}_N(\mathbf{v}_r) = \begin{bmatrix} -X_{|u|u}|u_r| & 0 & 0 \\ 0 & -Y_{|v|v}|v_r| & 0 \\ 0 & 0 & -N_{|r|r}|r_r| \end{bmatrix}. \quad (2.6b)$$

2.3 Waterjet Dynamics

This section will provide a simplified mathematical model of the dynamics of each of the two waterjets which powers Odin. The model presented in this section, except Section 2.3.1, is developed by FFI. The simulation model consists of two parts, namely thrust modeling and force and moment calculations. The model inputs are the relative velocity \mathbf{v}_r of the vessel, in addition to the waterjet demands

$$\mathbf{u} = \begin{bmatrix} u_{\text{nozzle}} \\ u_{\text{throttle}} \\ u_{\text{bucket}} \end{bmatrix}, \quad (2.7)$$

which are the demanded nozzle angle, throttle and reverse bucket level respectively. An overview of the model is given in Fig. 2.1.

First, the throttle demand $u_{\text{throttle}} \in [0, 100]$ is converted to the desired waterjet shaft revolutions per minute (RPM) through the mapping

$$\omega_{\text{rpm},d} = \omega_{\text{min}} + \frac{u_{\text{throttle}}}{100} (\omega_{\text{max}} - \omega_{\text{min}}), \quad (2.8)$$

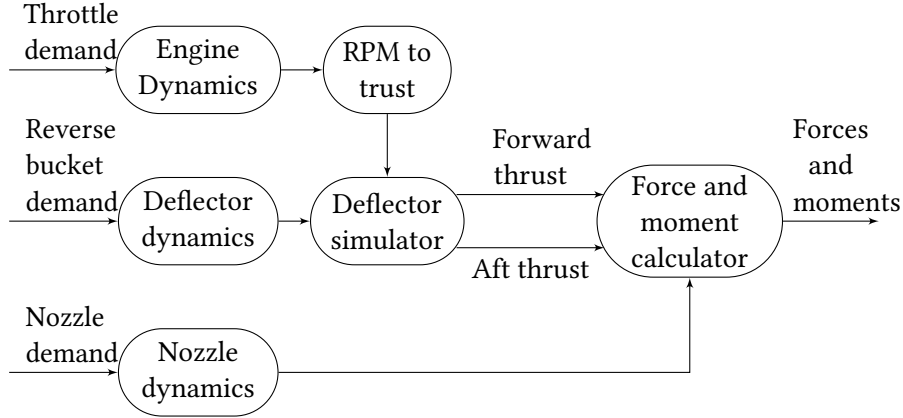


Figure 2.1: System overview of waterjet model

where ω_{\min} and ω_{\max} is the minimum and maximum RPM of the waterjet respectively. To imitate the behavior of a physical actuator, which has constraints on how fast the shaft rotation can be changed, a constraint on the maximum allowed RPM change per time step is added through a rate limiter

$$\omega_k = \begin{cases} \omega_{k-1} + \dot{\omega}_{\max}, & \|\omega_{\text{rpm},d} - \omega_{k-1}\| > \dot{\omega}_{\max} \\ \omega_{\text{rpm},d}, & \|\omega_{\text{rpm},d} - \omega_{k-1}\| < \dot{\omega}_{\max} \end{cases}, \quad (2.9)$$

where $\dot{\omega}_{\max}$ is the maximum allowed change per time step and ω_k and ω_{k-1} are the shaft RPM values at the current and previous time step.

The thrust model which converts the waterjet shaft RPM to thrust is modeled as a second-order polynomial function

$$T_{\text{wj}} = \frac{1}{2} \alpha_{\text{rpm}} (a_0 + a_1 u_r + a_2 u_r^2), \quad (2.10)$$

where u_r is the relative surge speed of the vessel and α_{rpm} a scaling factor given by

$$\alpha_{\text{rpm}}(\omega_{\text{rpm}}) = b_0 + b_1 \omega_{\text{rpm}} + b_2 \omega_{\text{rpm}}^2. \quad (2.11)$$

The resulting thrust is not only dependent on the shaft RPM but also on the relative velocity of the vessel. The reason is that the waterjet works by taking water from an intake underneath the vessel in front of the actuator which is accelerated through the waterjet and discharged through the nozzle to create a forward propulsive force by Newton's third law of motion. The resulting thrust as a function of relative surge speed and throttle demand can be seen in Fig. 2.2.

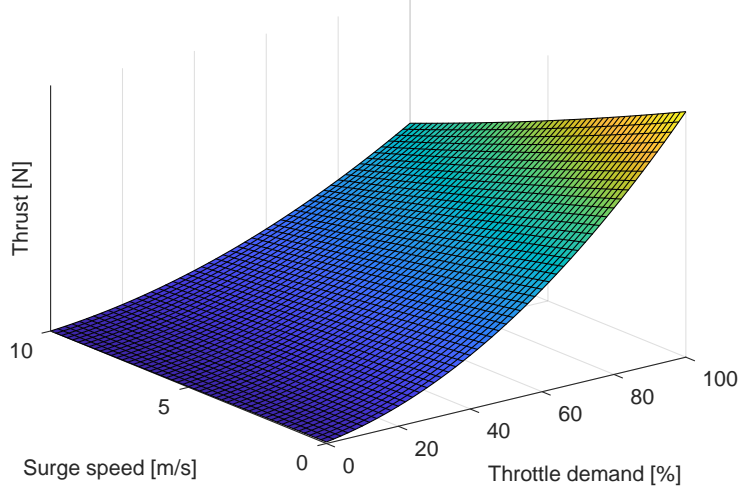


Figure 2.2: Waterjet thrust as a function of relative surge speed and throttle demand. The thrust is plotted without numerical data on request by FFI.

Next, the forces and moments are modeled as a function of the reverse bucket position and the nozzle angle. The nozzle demand $u_{\text{nozzle}} \in [-100, 100]$ is mapped to the desired nozzle angle of the waterjet using a similar mapping as the throttle

$$\delta_{\text{nozzle},d} = \delta_{\text{min}} + \left(\frac{u_{\text{nozzle}}}{100} + 1 \right) \left(\frac{\delta_{\text{max}} - \delta_{\text{min}}}{2} \right), \quad (2.12)$$

where δ_{min} and δ_{max} is the minimum and maximum nozzle angle respectively. In the case where the operation area of the nozzle angle is centered around zero i.e $\delta_{\text{min}} = -\delta_{\text{max}}$, (2.12) reduces to (2.8). The desired nozzle angle is then modelled with a rate limiter equal to (2.9)

$$\delta_k = \begin{cases} \delta_{k-1} + \dot{\delta}_{\text{max}}, & \|\delta_{\text{nozzle},d} - \delta_{k-1}\| > \dot{\delta}_{\text{max}} \\ \delta_{\text{nozzle},d}, & \|\delta_{\text{nozzle},d} - \delta_{k-1}\| < \dot{\delta}_{\text{max}} \end{cases}, \quad (2.13)$$

where $\dot{\delta}_{\text{max}}$ is the maximum allowed change in nozzle angle per time step and δ_k and δ_{k-1} are the nozzle angles at the current and previous time step.

As the operation area of the nozzle angle is limited, the waterjet is not able to generate negative thrust using only the throttle and nozzle. By using the deflector, the jet stream splits into three components: one aft jet and two directed forward and to the sides, allowing the vessel to slow down. The reverse bucket demand

$u_{\text{bucket}} \in [-100, 100]$ is mapped to desired bucket position as

$$\gamma_{\text{bucket},d} = -1 + \left(\frac{u_{\text{bucket}}}{100} + 1 \right), \quad (2.14)$$

where the deflector is fully lowered when $\gamma_{\text{bucket},d} = -1$ and fully raised when $\gamma_{\text{bucket},d} = 1$. Again, the reverse bucket dynamics are passed through the rate limiter

$$\gamma_k = \begin{cases} \gamma_{k-1} + \dot{\gamma}_{\text{max}}, & \|\gamma_{\text{bucket},d} - \gamma_{k-1}\| > \dot{\gamma}_{\text{max}} \\ \gamma_{\text{bucket},d}, & \|\gamma_{\text{bucket},d} - \gamma_{k-1}\| < \dot{\gamma}_{\text{max}} \end{cases}, \quad (2.15)$$

where $\dot{\gamma}_{\text{max}}$ is the maximum allowed change in reverse bucket position per time step and γ_k and γ_{k-1} the reverse bucket positions at the current and previous time step.

Using the deflector position γ the expression for the reverse and forward thrust component caused by the deflected jetstream is

$$T_{\text{rev}} = \begin{cases} T_{\text{wj}} (-b\gamma_{\text{bucket}} + b), & \gamma_{\text{bucket}} \geq 0 \\ T_{\text{wj}} [(b-1)\gamma_{\text{bucket}} + b], & \gamma_{\text{bucket}} < 0 \end{cases} \quad (2.16)$$

$$T_{\text{fwd}} = T_{\text{wj}} - T_{\text{rev}}, \quad (2.17)$$

where b is a constant. It can be observed that when $\gamma_{\text{bucket}} = 0$, i.e. when the reverse bucket is in neutral position, the forward and reverse thrust components cancel each other. Finally, the x component of the force generated by the waterjet can be calculated as

$$f_x = f_{x,\text{nozzle}} + f_{x,\text{portduct}} + f_{x,\text{stbduct}} \quad (2.18)$$

$$f_{x,\text{nozzle}} = T_{\text{fwd}} \cos(\delta_{\text{nozzle}}) \quad (2.19)$$

$$f_{x,\text{portduct}} = \frac{1}{2} T_{\text{rev}} \cos(\beta_1) \cos(\beta_2) \left(1 - \frac{\delta_{\text{nozzle}}}{\delta_{\text{max}}} \right) \quad (2.20)$$

$$f_{x,\text{stbduct}} = \frac{1}{2} T_{\text{rev}} \cos(-\beta_1) \cos(\beta_2) \left(1 + \frac{\delta_{\text{nozzle}}}{\delta_{\text{max}}} \right), \quad (2.21)$$

and similarly with the y component

$$f_y = f_{y,\text{nozzle}} + f_{y,\text{portduct}} + f_{y,\text{stbduct}} \quad (2.22)$$

$$f_{y,\text{nozzle}} = T_{\text{fwd}} \sin(\delta_{\text{nozzle}}) \quad (2.23)$$

$$f_{y,\text{portduct}} = \frac{1}{2} T_{\text{rev}} \sin(\beta_1) \cos(\beta_2) \left(1 - \frac{\delta_{\text{nozzle}}}{\delta_{\text{max}}} \right) \quad (2.24)$$

$$f_{y,\text{stbduct}} = \frac{1}{2} T_{\text{rev}} \sin(-\beta_1) \cos(\beta_2) \left(1 + \frac{\delta_{\text{nozzle}}}{\delta_{\text{max}}} \right), \quad (2.25)$$

where β_1 and β_2 are the angles the jetstream is deflected to port/starboard and down when the reverse bucket is in use. The generated moment about the z-axis generated is equal to

$$m_z = l_x f_y - l_y f_x, \quad (2.26)$$

where l_i are the lever arm for the x and y forces respectively. Finally, the generalized force vector generated by a single waterjet can be expressed as

$$\boldsymbol{\tau}^b = \begin{bmatrix} f_x \\ f_y \\ m_z \end{bmatrix}. \quad (2.27)$$

2.3.1 Linearization of Waterjet Dynamics

In this section, a linearized version of the waterjet dynamics between the nozzle angle demand and the generated z moment is derived to simplify the controller design for the heading autopilot. Inspired by the modeling of rudder dynamics in Fossen (2011), a similar expression on the form

$$\tau_3 = -N_{u_{\text{nozzle}}} u_{\text{nozzle}}, \quad (2.28)$$

is derived. Many different methods are developed for control of ships equipped with main propellers and aft rudders as they are common actuators for conventional marine craft. By approximating the dynamics for the waterjet similarly, it opens up the possibilities to utilize those methods, such as pole-placement algorithms for tuning of heading PID controllers for Odin.

Looking at the waterjet dynamics in Section 2.3, it can be noticed that while the total dynamics are nonlinear, most of the nonlinearities arise from the thrust model (2.10) and the reverse bucket thrust components in (2.18) and (2.22). In fact, with the reverse bucket duct fully raised and for small nozzle angles, the nonlinear dynamics are less dominant and a linear approximation such as (2.28) could represent the actual behavior quite well in those cases.

Assumption 2.2. *Both waterjets are equal and positioned symmetric about the xz-plane (port/starboard) of the vessel.*

Assumption 2.3. *The marine vessel is operating at a constant surge speed u_0 such*

that the throttle demand required to maintain the speed satisfies $u_{\text{throttle}} \geq 10$ implying $u_{\text{duct}} = 100$, i.e. fully raised according to (2.36).

Assumption 2.4. The nozzle angle is centered around zero with a relatively small maximum angle δ_{max} .

Under Assumption 2.2, the total moment generated about the z-axis is equal to

$$\tau_3 = m_z = 2l_x f_y, \quad (2.29)$$

as the moment generated by the x-components from each of the waterjets cancel each other. Further, Assumption 2.3 implies that the latter two terms in (2.22) vanishes due to the reverse duct being fully raised. By using the approximation $\sin(x) \approx x$ with Assumption 2.4, a linear approximation to the generated moment about the z-axis by the nozzle angle can be expressed as

$$\tau_3 = 2l_x T_{\text{fwd},i} \frac{\delta_{\text{max}}}{100} u_{\text{throttle}}, \quad (2.30)$$

where $T_{\text{fwd},i}$ is the forward thrust generated by each of the waterjets.

To calculate the forward thrust T_{fwd} required to operate at the constant surge speed u_0 , the forward speed model is used

$$T_{\text{fwd}} = \sum_i T_{\text{fwd},i} = -X_u u_0 - X_{|u|u} |u_0| u_0. \quad (2.31)$$

This means the linear relationship between the nozzle angle demand and the generated moment about the z-axis can be related through the constant

$$N_{u_{\text{nozzle}}} = \frac{(X_u u_0 + X_{|u|u} |u_0| u_0) l_x \delta_{\text{max}}}{100}. \quad (2.32)$$

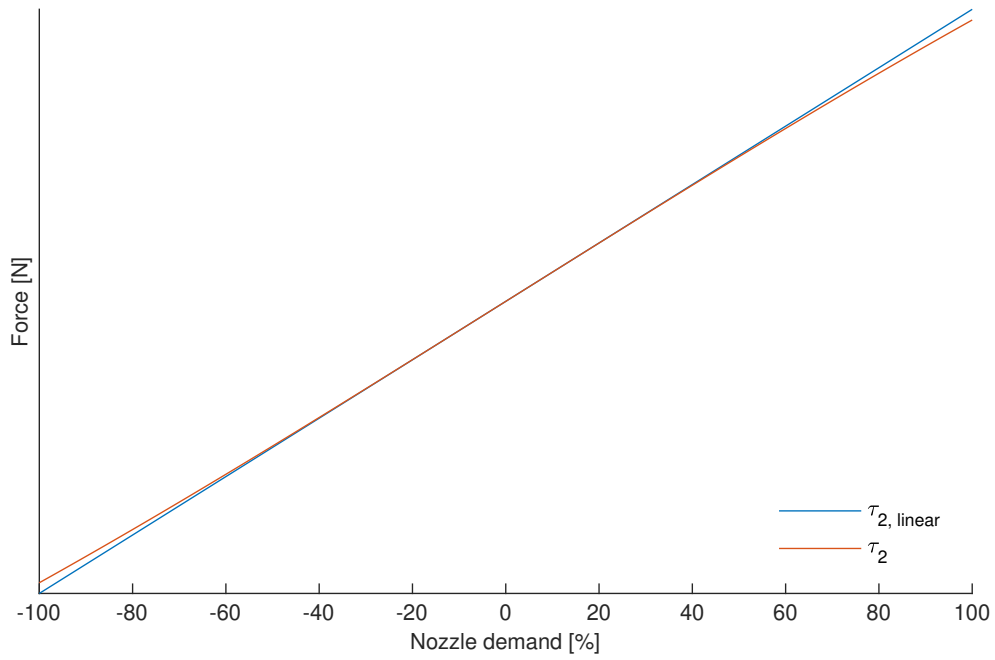
Similarly, the relationship between the nozzle angle demand and the generated y force can be linearized as

$$\tau_2 = -Y_{u_{\text{nozzle}}} u_{\text{nozzle}}, \quad (2.33)$$

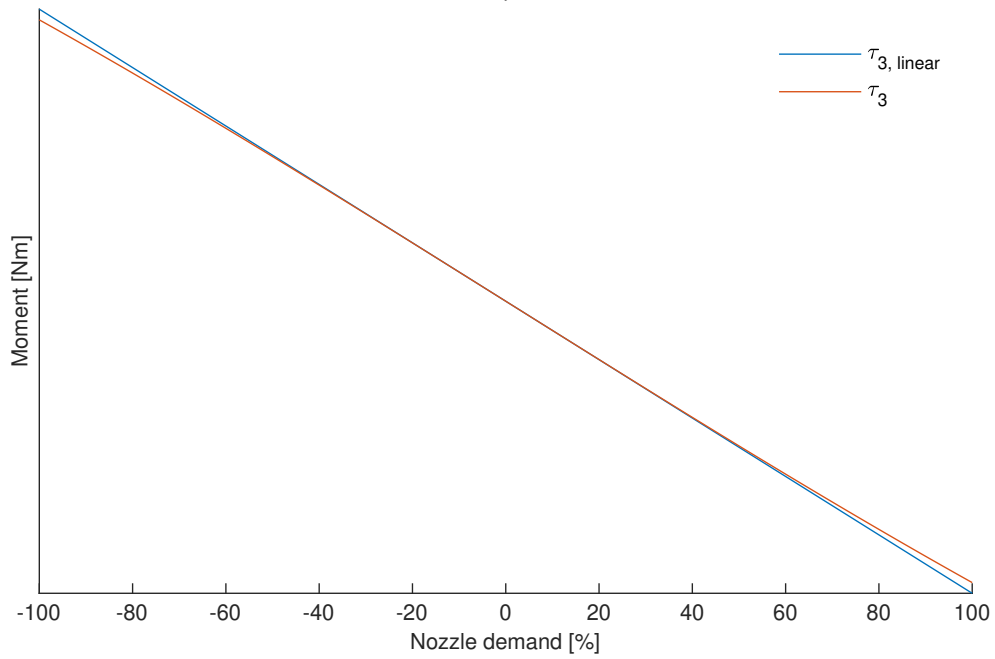
with

$$Y_{u_{\text{nozzle}}} = \frac{(X_u u_0 + X_{|u|u} |u_0| u_0) \delta_{\text{max}}}{100}. \quad (2.34)$$

The linearized waterjet dynamics are plotted against the actual dynamics in Fig. 2.3. It can be noticed that the linearization resembles the actual generated forces and moments well, even for large values of u_{nozzle} , meaning the linearized model is a good approximation.



(a) Sway force



(b) Yaw moment

Figure 2.3: Linearized waterjet dynamics vs actual dynamics. Plotted without numerical data on request by FFI.

2.4 Maneuvering Controllers

This section will present the maneuvering controllers for heading and surge using simplified control design methods. The controllers are not tuned for the real vessel, but the simulation model of Odin. Even though the simulation model presented earlier in this chapter is designed to represent the actual vessel dynamics, a perfect model is impossible. Therefore, it is desirable to have well-tuned maneuvering controllers for the simulation model than using the actual values from Odin, which will perform sub-optimal in simulations.

The maneuvering controllers presented in this section operate directly on the desired throttle and steering demands of the waterjet, instead of desired force allocation. This is due to the complexity and uncertainties in both the waterjet model and the vessel parameters. An implication of this is that more advanced control techniques such as acceleration feed-forward and feedback-linearization are not possible as the mapping from desired force/torque to desired throttle and steering demands is unknown.

The autopilots presented here were first introduced in Eek (2019), and briefly repeated here for convenience. The reader is referred to Eek (2019) for more details.

2.4.1 Surge Controller

The selected controller for the surge speed is a PI controller, with anti-windup using the tracking back calculation scheme. Due to the aforementioned reasons, the controller operates directly on the desired throttle demand

$$u_{\text{throttle}} = -K_p(u - u_d) - K_i \int_0^t (u - u_d) d\tau - \frac{1}{T_t} \int_0^t (u_{\text{throttle}} - u_{\text{throttle,unsat}}) d\tau, \quad (2.35)$$

where $u_{\text{throttle,unsat}} \in \mathbb{R}$ is the unsaturated value of u_{throttle} and T_t the tracking time constant chosen to be equal to the integral time constant of the PI controller. In Eek (2019) it was shown that by choosing $K_p = 150$ and the integral time-constant $T_i = 5$ satisfactory performance of the surge dynamics were obtained.

The reason for operating directly on the desired throttle demand is that it eliminates the need for an additional control allocation method, which would have been complicated due to the nonlinear nature and model uncertainties of the waterjet model. By operating directly on u_{throttle} , the need for a control allocation block is bypassed, simplifying the control system design.

As mentioned in Section 2.3, the waterjet is equipped with a reverse bucket duct,

which can be lowered to deflect the water stream forward to generate a negative thrust. When the throttle demand $u_{\text{throttle}} < 0$, this deflector will be lowered down

$$u_{\text{duct}} = \begin{cases} 100, & u_{\text{throttle}} \geq 10 \\ -100, & u_{\text{throttle}} \leq -10 \\ 10 \cdot u_{\text{throttle}}, & \text{otherwise} \end{cases} \quad (2.36)$$

$$u_{\text{throttle}} = \begin{cases} 100, & u_{\text{throttle}} \geq 100 \\ |u_{\text{throttle}}|, & \text{otherwise} \end{cases} . \quad (2.37)$$

To generate a negative thrust demand when lowering the deflector, a positive throttle demand is still required. Therefore, the throttle demand absolute value of u_{throttle} is sent to the actuators instead of u_{throttle} directly. This is similar to the current method used for Odin, and is thus chosen to resemble this behavior.

2.4.2 Heading Controller

The heading controller design presented in here is based on the first-order Nomoto model

$$(I_z - N_{\dot{r}})\ddot{\psi} + N_r\dot{\psi} = \tau_3, \quad (2.38)$$

which describes the sway-yaw dynamics decoupled from the surge. Odin is capable of having full actuation in all three degrees of freedom as it is equipped with two waterjets. However, in this thesis, they are linked together, meaning the same commands are sent to both waterjets. The implication of this is that Odin, for the applications targeted in this thesis, will be under-actuated without directly controlling the sway dynamics.

2.4.2.1 Reference Model

To ensure that the vessel is able to follow the desired heading reference at any moment in time, a position reference model from Fossen (2011) is used. The reference model is motivated by the dynamics of a mass-damper-spring (MDS) system to generate the desired heading reference

$$\psi_d^{(3)} + (2\zeta + 1)\omega_n\ddot{\psi}_d + (2\zeta + 1)\omega_n^2\dot{\psi}_d + \omega_n^3\psi_d = \omega_n^3\psi_r, \quad (2.39)$$

where ψ_d is the desired heading, ψ_r the reference signal and ζ and ω_n the relative damping ration and natural frequency respectively. Using a reference model such

as (2.39) ensures that the control system receives smooth reference signals for the desired heading ψ_d and its derivative \dot{r}_d .

2.4.2.2 PID Controller

To control the heading of the vessel a standard PID controller will be utilized on the form

$$u_{\text{nozzle}} = -K_p(\psi - \psi_d) - K_i \int_0^t (\psi - \psi_d) d\tau - K_d(r - r_d) - \frac{1}{T_t} \int_0^t (u_{\text{nozzle}} - u_{\text{nozzle,unsat}}) d\tau, \quad (2.40)$$

where u_{nozzle} is the nozzle demand to the waterjet, r the yaw rate of the vessel, r_d the desired yaw rate, and $u_{\text{nozzle,unsat}}$ the unsaturated nozzle demand. By inserting the PID controller (2.40) with expression for the linearized waterjet dynamics in Section 2.3.1 into the Nomoto model (2.38) gives the closed loop form

$$\underbrace{-\frac{N_{\dot{r}} - I_z}{N_{u_{\text{nozzle}}}}}_{m} \ddot{\psi} + \underbrace{\frac{N_r}{N_{u_{\text{nozzle}}}}}_{d} \dot{\psi} = u_{\text{nozzle}}. \quad (2.41)$$

Then, the pole-placement algorithm from (Fossen; 2011, Table 12.2) was used to tune the heading PID controller by selecting a proper bandwidth and relative damping ratio. The tracking back-calculation time constant T_t was further chosen according to the rule-of-thumb given in Markaroglu et al. (2006) as

$$T_t = \sqrt{T_i \cdot T_d}, \quad (2.42)$$

where T_i and T_d is the integral and derivative time constants of (2.40). The different control parameters were in Eek (2019) chosen as $\omega_n = 3$, $\zeta = 1$ for the PID parameters and the natural frequency $\omega_{n,\text{ref}} = 2$ for the reference model.

3 | Cable Modeling

In this chapter, a discrete mathematical model describing the equations of motion of a flexible floating cable is presented using analytical mechanics. First, a model based on Bhattacharya et al. (2011) is presented, where a new hydrodynamic drag model is proposed to incorporate the effects of ocean currents. Then, a solution to the differential-algebraic equation system DAE is presented, such that it can be simulated using MATLAB. Next, the cable model presented in this chapter is connected with the vessel model presented in Chapter 2. Finally, the cable model is verified through several simulations verifying the extended hydrodynamic drag model when exposed to ocean currents, and that the simulated loads on the vessels from the cable model match experimental data.

The model and theory presented in this chapter, except Section 3.4 and Section 3.5, is based on Bhattacharya et al. (2011) unless stated otherwise. However, the hydrodynamic drag model Section 3.2.2 has been extended to incorporate the effects of ocean currents by the author of this thesis.

3.1 Introduction

The ability to express the cable dynamics as a mathematical model through the equations of motion is advantageous. It allows validation of the formation control methods presented later in the thesis in simulations under realistic scenarios instead of having to resort to experiments. Thus, several studies have been performed with the goal of modeling and simulation of a cable.

In Jiménez et al. (2005) Newtonian and canonical methods were used to study the motion of a rope falling from a table. However, the model only considers a one-dimensional system. Further, as the study considers a rope in the air, it does not incorporate hydrodynamic drag forces.

Two other models (1) Euler Angle Cable (EAC) and (2) Rigid Bar Cable (RBC) for underwater cable dynamics are proposed in Johansen (2007), for the application of

fish trawler systems. The first model shows good coincidence between simulations and experiments at the cost of higher computational complexity. In contrast, the latter model can be considered as a trade-off between accuracy and computational speed to be better suited for real-time simulations. However, both these models describe the cable dynamics in 3D, which is unnecessary for the 3-DOF applications considered in this thesis.

In Arrichiello et al. (2018), the dynamics of a flexible cable towed by an Autonomous Underwater Vehicle (AUV) is modeled similarly as an industrial manipulator using the Newton-Euler recursive Algorithm. However, similarly to the latter method, Arrichiello et al. (2018) also considers 3D cable dynamics.

Kheiri et al. (2013) presents a nonlinear model for a towed, neutrally buoyant flexible slender cylinder in the horizontal plane. The inviscid and viscous dynamic forces are both modeled to third-order accuracy. The resulting PDE is then transformed into a discrete ODE. However, the authors experienced several stability issues with the derived model under various scenarios. Further, the accuracy obtained by this model was found to be superfluous for the application considered in this thesis.

In Pereda et al. (2011), a discrete model for a cable towed behind two marine vessels for oil spill confinement is presented. Here, the dynamics of each link are modeled using Newton's 2. law, and the continuity of the cable is ensured through a closing condition forcing all links to remain connected. While the model presented in Pereda et al. (2011) only includes linear hydrodynamic drag forces, it is further extended to incorporate quadratic damping in Jimenez and Giron-Sierra (2018). However, as the linear and angular accelerations are calculated individually for each link, the model is sensitive to numerical errors, causing the closing condition to diverge, i.e., the links will not necessarily remain connected to each other. During the simulation, an extra correction after each iteration must thus be performed attaching the links again, see Jimenez (2016), making the method sub-optimal seen from efficiency and implementation point of view.

Bhattacharya et al. (2011) also consider a similar scenario with oil spill confinement, and present several models describing the dynamics of a cable towed behind two marine vessels, including a continuous PDE based on a nonlinear wave equation. However, for the applications considered here, the two discrete methods (1) *force controlled system* and (2) *position controlled system*, also presented in the paper, are of more interest. The first model takes the forces applied by the two vessels as input and outputs the link angle, i.e., the angle the link forms with the global inertia frame, and the cable end positions, while the second model takes the cable end positions

as input and outputs the link angles and forces that would have been applied from the vessels to obtain such a position. The latter approach matches well with the application considered in this thesis as the cable ends will be connected to each vessel and thus have a known position which can be used as an input to the model. Further, by using Newton's third law, the calculated forces given as the output will correspond to the forces applied by the cable on each vessel, i.e., how towing the cable will affect the dynamics of each vessel slowing it down. However, neither of the models from Bhattacharya et al. (2011) considers how the cable dynamics will be affected by ocean currents.

3.2 Cable dynamics

In the modeling of the dynamics of the flexible floating cable, an approximate discrete model from Bhattacharya et al. (2011) is used, where the cable is approximated by n rigid cylindrical links connected by revolute joints, see Fig. 3.1a. More specifically, the model presented here is based on the *Position Controlled System* model in Bhattacharya et al. (2011). The endpoints of the cable are assumed rigidly attached to each boat, implying the endpoint positions $\{x_L, y_L, x_R, y_R\}$, and their derivatives are known, while the link angles θ_i and the forces applied by the two vessels $\{f_{Lx}, f_{Ly}, f_{Rx}, f_{Ry}\}$ are unknown.

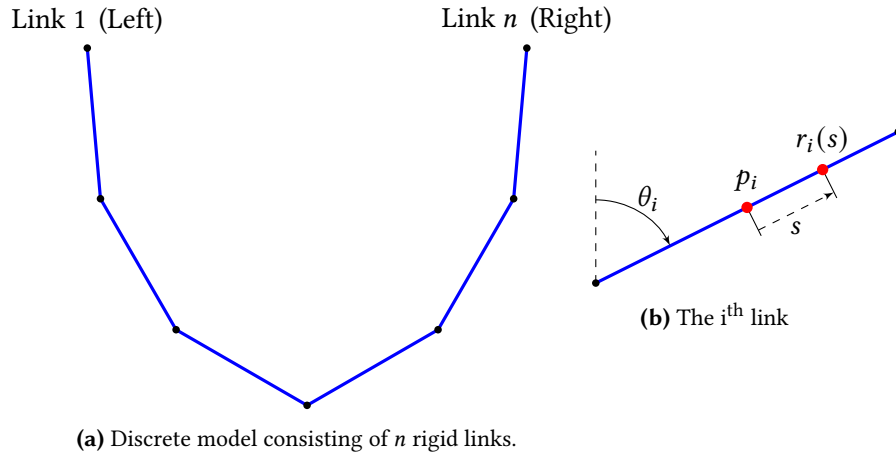


Figure 3.1: Discrete model visualization

Assumption 3.1. *When modeling the cable dynamics, only 3-DOF motion in the horizontal plane, i.e. position in x - and y -direction along with the link angle, will be considered.*

An implication of Assumption 3.1 is that both gravity and buoyancy forces will be neglected when deriving the equations of motion of the cable. Thus, no potential forces will affect system dynamics. This assumption will also imply that the cable is assumed to float at the ocean surface at all times. In reality, this is not true as it will sink a bit when towed and thus be located below the surface. However, this assumption is made to simplify the modeling of cable dynamics and match the 3-DOF assumption in Chapter 2.

To derive the equations of motion, the system is expressed in terms of the generalized coordinates by modelling each link as a rigid cylinder with length L_i and mass m_i .

$$q_i \in \{\theta_1, \theta_2, \dots, \theta_n\}, \quad (3.1)$$

where θ_i is the link angle of link $i \in 1, \dots, n$ and is defined as the angle that the link forms with the x axis of the NED reference frame. Then, the hydrodynamic forces and torques are expressed in terms of generalized forces, before the Lagrange's equations of motion are found.

Remark 3.1. *In Bhattacharya et al. (2011), a different global inertial frame is used with a horizontal x -axis, vertical y -axis, and the z -axis pointing up, out of the paper, completing the right-hand rule. However, the validity of the model is not affected, meaning the model presented here will be identical, only differing in the definition of θ_i , see Fig. 3.1b and (Bhattacharya et al.; 2011, Fig. 4b).*

3.2.1 Kinematics

First, to derive the forward kinematics of the cable, the position of the center of mass of link i can be expressed as

$$\mathbf{p}_i = \begin{bmatrix} x_L \\ y_L \end{bmatrix} + \sum_{j=1}^{i-1} L_j \begin{bmatrix} \cos(\theta_j) \\ \sin(\theta_j) \end{bmatrix} + \frac{L_i}{2} \begin{bmatrix} \cos(\theta_i) \\ \sin(\theta_i) \end{bmatrix}, \quad (3.2)$$

where L_j is the length of link j , and $\{x, y\}_L$ is the NED position of the base link, connected to the left vessel. Similarly, the position of the end link, connected to the right vessel can be expressed as

$$\begin{bmatrix} x_R \\ y_R \end{bmatrix} = \begin{bmatrix} x_L \\ y_L \end{bmatrix} + \sum_{j=1}^n L_j \begin{bmatrix} \cos(\theta_j) \\ \sin(\theta_j) \end{bmatrix}. \quad (3.3)$$

Further, by taking the time derivative of (3.2), the velocity of the center of mass

of link i can be expressed as

$$\mathbf{v}_i = \begin{bmatrix} \dot{x}_L \\ \dot{y}_L \end{bmatrix} + \sum_{j=1}^{i-1} L_j \dot{\theta}_j \begin{bmatrix} -\sin(\theta_j) \\ \cos(\theta_j) \end{bmatrix} + \frac{L_i}{2} \dot{\theta}_i \begin{bmatrix} -\sin(\theta_i) \\ \cos(\theta_i) \end{bmatrix}. \quad (3.4)$$

3.2.2 Hydrodynamic drag forces

In Bhattacharya et al. (2011), the hydrodynamic drag forces and torques are modeled using a linear drag model. The drag effects are modeled by splitting the velocity into two components (1) parallel to the link, meaning it is parallel to the y-axis (\mathbf{v}_i^{\parallel}) and (2) perpendicular to the link, rendering it parallel to the x-axis (\mathbf{v}_i^{\perp}). At low-speed operations, the drag is assumed to be linear to the speed, but with different drag coefficients for the parallel and perpendicular components. The net external hydrodynamic drag forces and torque on the i^{th} link are then calculated by taking the integral of the drag force and torque per unit length across the whole link.

However, the hydrodynamic drag model presented in Bhattacharya et al. (2011) has a shortcoming where the effects of ocean current are neglected when calculating the hydrodynamic drag forces and torque. When the model presented in Bhattacharya et al. (2011) is simulated in scenarios where ocean currents are present, the accuracy of the model would not be satisfactory as the hydrodynamic drag effects would fail to include the hydrodynamic effects due to the ocean current, and thus would not be realistic. For instance, consider the case where a stationary cable, with zero absolute velocity to the inertia frame, with both ends connected to rigid stationary objects, is located in an environment exposed to ocean currents. With the model presented in Bhattacharya et al. (2011), the resulting hydrodynamic forces and torques would be zero as the cable has no absolute velocity to the inertia frame. However, the cable would still have a non-zero relative velocity to the freestream flow around the cable, resulting in non-zero hydrodynamic drag forces and torques in the real world. In other words, the model presented in Bhattacharya et al. (2011) would fail to capture these hydrodynamic drag effects as the absolute velocity, which in this case, would be zero.

Consider the following scenario, which further highlights the importance of including the hydrodynamic effects due to the ocean current. A cable with both ends free, i.e., neither cable ends are connected to anything, and with zero initial velocity, is located in an environment exposed to ocean currents. Thinking logically, as the cable is not connected to anything, it should drift with the ocean current. However, as in the last scenario, the model presented in Bhattacharya et al. (2011) would be

unaffected by the ocean currents, and remain at the same position at all times, again since the absolute velocity is zero resulting in zero hydrodynamic drag forces and torques. By extending the drag model to include the relative velocities, the effects of the ocean currents would be captured, and the cable would begin to drift.

To extend the model presented in Bhattacharya et al. (2011) to include effects caused by ocean currents, a new proposal of how to calculate the hydrodynamic forces and torque is presented in this thesis. Instead of using the absolute velocities when calculating the hydrodynamic forces and torques, a modified approach by using the relative velocities is proposed

$$\mathbf{F}_i = \begin{bmatrix} F_{i,x} \\ F_{i,y} \end{bmatrix} = - \int_{-L_i/2}^{-L_i/2} \left(c_V \mathbf{v}_{r,i}^{\parallel}(s) + c_S \mathbf{v}_{r,i}^{\perp}(s) \right) ds \quad (3.5a)$$

$$\tau_i = - \int_{-L_i/2}^{-L_i/2} \dot{\mathbf{r}}_i(s) \times \left(c_V \mathbf{v}_{r,i}^{\parallel}(s) + c_S \mathbf{v}_{r,i}^{\perp}(s) \right) ds, \quad (3.5b)$$

where the absolute velocities in the expression from (Bhattacharya et al.; 2011, Eq. 8) are replaced with the relative velocities

$$\mathbf{v}_{r,i}^{\parallel} = \left[\hat{\mathbf{u}}_i^{\parallel} \cdot \left(\dot{\mathbf{r}}_i(s) - \begin{bmatrix} V_x \\ V_y \end{bmatrix} \right) \right] \hat{\mathbf{u}}_i^{\parallel} \quad (3.6a)$$

$$\mathbf{v}_{r,i}^{\perp} = \left[\hat{\mathbf{u}}_i^{\perp} \cdot \left(\dot{\mathbf{r}}_i(s) - \begin{bmatrix} V_x \\ V_y \end{bmatrix} \right) \right] \hat{\mathbf{u}}_i^{\perp}, \quad (3.6b)$$

where $\hat{\mathbf{u}}_i^{\parallel} = \begin{bmatrix} \cos(\theta_i) \\ \sin(\theta_i) \end{bmatrix}$ and $\hat{\mathbf{u}}_i^{\perp} = \begin{bmatrix} -\sin(\theta_i) \\ \cos(\theta_i) \end{bmatrix}$ are the parallel and perpendicular unit velocity components of the link, and V_x and V_y are the ocean components in x and y direction given in NED. The velocity of $\mathbf{r}_i(s)$ is still modeled as in Bhattacharya et al. (2011) and is given by

$$\dot{\mathbf{r}}_i(s) = \frac{d}{dt} \left(\mathbf{p}_i + s \begin{bmatrix} \cos(\theta_i) \\ \sin(\theta_i) \end{bmatrix} \right) = \mathbf{v}_i + s \begin{bmatrix} -\sin(\theta_i) \\ \cos(\theta_i) \end{bmatrix} \dot{\theta}_i. \quad (3.7)$$

Note how, by using the relative instead of the absolute velocity, effects caused by the ocean current now will be captured by the drag model. The contributing factors for the hydrodynamic drag forces and torques are no longer the cable's movement to the inertia frame, but rather the freestream flow surrounding the cable. In the

trivial case with no ocean currents, the proposed drag model (3.5) reduces to the drag model presented in Bhattacharya et al. (2011).

3.2.3 Generalized forces

When deriving the equations of motion for a mechanical system using analytical mechanics, all external non potential forces must be expressed in terms of generalized forces. The generalized force associated with the generalized coordinate q_i is defined in Egeland and Gravdahl (2002) as

$$Q_i \triangleq \sum_{k=1}^n \frac{\partial \mathbf{r}_k}{\partial q_i} \cdot \mathbf{F}_k, \quad (3.8)$$

where \mathbf{r}_k is the contact point of the force \mathbf{F}_k . Using (3.8) the generalized force for each of the generalized coordinates may then be expressed as

$$\begin{aligned} Q_{\theta_i} &= \begin{bmatrix} f_{Lx} \\ f_{Ly} \end{bmatrix} \cdot \frac{\partial \begin{bmatrix} x_L \\ y_L \end{bmatrix}}{\partial \theta_i} + \begin{bmatrix} f_{Rx} \\ f_{Ry} \end{bmatrix} \cdot \frac{\partial \begin{bmatrix} x_R \\ y_R \end{bmatrix}}{\partial \theta_i} + \sum_{j=1}^n \mathbf{F}_j \cdot \frac{\partial \mathbf{p}_j}{\partial \theta_i} \\ &= -f_{Rx} L_i \sin(\theta_i) + f_{Ry} L_i \cos(\theta_i) + \tau_i + \sum_{j=1}^n \mathbf{F}_j \cdot \frac{\partial \mathbf{p}_j}{\partial \theta_i}. \end{aligned} \quad (3.9)$$

Equally, the generalized force for the left cable end may be expressed as

$$\begin{aligned} Q_{x_L} &= \begin{bmatrix} f_{Lx} \\ f_{Ly} \end{bmatrix} \cdot \frac{\partial \begin{bmatrix} x_L \\ y_L \end{bmatrix}}{\partial x_L} + \begin{bmatrix} f_{Rx} \\ f_{Ry} \end{bmatrix} \cdot \frac{\partial \begin{bmatrix} x_R \\ y_R \end{bmatrix}}{\partial x_L} + \sum_{j=1}^n \mathbf{F}_j \cdot \frac{\partial \mathbf{p}_j}{\partial x_L} \\ &= f_{Lx} + f_{Rx} + \sum_{j=1}^n \mathbf{F}_{j,x} \end{aligned} \quad (3.10a)$$

$$Q_{y_L} = f_{Ly} + f_{Ry} + \sum_{j=1}^n \mathbf{F}_{j,y}. \quad (3.10b)$$

3.2.4 Lagrange's equations of motion

Lagrange's equations of motion is then formulated using the *Lagrangian*

$$\mathcal{L} = K - P, \quad (3.11)$$

defined as the difference in kinetic and potential energy. As only the motion in the horizontal plane is considered Assumption 3.1, no potential forces are affecting the system. Thus the *Lagrangian* simplifies to the kinetic energy of the whole system

$$\mathcal{L} = K = \sum_{i=1}^n \left(\frac{1}{2} m_i \|\mathbf{v}_i\|_2^2 + \frac{1}{2} \frac{m_i L_i^2}{12} \dot{\theta}_i^2 \right), \quad (3.12)$$

where $I_i = \frac{1}{12} m_i L_i^2$ is the moment of inertia for each link about its center. The equations of motion describing the cable dynamics are then given by the Euler-Lagrange equation

$$\frac{d}{dt} \left(\frac{\partial \mathcal{L}}{\partial \dot{\sigma}} \right) - \frac{\partial \mathcal{L}}{\partial \sigma} - Q_\sigma = 0 \quad (3.13)$$

for all $\sigma \in \{x_L, y_L, \theta_1, \theta_2, \dots, \theta_n\}$.

It should be noted how (3.13) does not include any terms consisting of the right cable end position x_R, y_R or their derivatives. Instead, the dynamics of the right cable end position is expressed through taking the time derivative of (3.3) to obtain the velocity constraint

$$\begin{bmatrix} \dot{x}_R \\ \dot{y}_R \end{bmatrix} - \begin{bmatrix} \dot{x}_L \\ \dot{y}_L \end{bmatrix} - \sum_{j=1}^n L_j \dot{\theta}_j \begin{bmatrix} -\sin(\theta_j) \\ \cos(\theta_j) \end{bmatrix} = 0, \quad (3.14)$$

and by taking the time derivative again, the acceleration constraint is obtained

$$\begin{bmatrix} \ddot{x}_R \\ \ddot{y}_R \end{bmatrix} - \begin{bmatrix} \ddot{x}_L \\ \ddot{y}_L \end{bmatrix} - \sum_{j=1}^n L_j \left(\ddot{\theta}_j \begin{bmatrix} -\sin(\theta_j) \\ \cos(\theta_j) \end{bmatrix} - \dot{\theta}_j^2 \begin{bmatrix} \cos(\theta_j) \\ \sin(\theta_j) \end{bmatrix} \right) = 0. \quad (3.15)$$

Together, (3.13) and (3.15) form $n + 4$ equations, which are 2nd order ODEs in link angles θ_i and algebraic in the forces $\{f_{Lx}, f_{Ly}, f_{Rx}, f_{Ry}\}$. As the system contains both differential and algebraic equations, it is not an ODE, but rather a differential algebraic equation system (DAE).

3.3 Solving the DAE system

This section will present a method of transforming the DAE system obtained when modeling the cable dynamics in the last section into a structure that will allow it to be solved using MATLAB. Bhattacharya et al. (2011) does not explain the exact steps of the method, and it is not covered in detail in the paper. However, the implementation of the method used in Bhattacharya et al. (2011) may be found in the corresponding

code to the paper, which is published on Bhattacharya's web page Bhattacharya (2020b). The method presented here may be seen as an attempt to formalize the implementation in Bhattacharya (2020a).

In general, DAE systems differ from ODEs in that they include an algebraic constraint that restricts the solution to the constraint manifold, which makes them generally more challenging to solve. DAEs often arise when modeling many different systems, including mechanical systems, see, for instance, Gerdt (2015).

All DAEs may be converted into a system of ODEs by eliminating the algebraic equations through differentiating the equations. The number of derivatives needed to eliminate all algebraic equations is a measurement of the DAEs complexity and is called the *differential index*, see Egeblad and Gravdahl (2002). Naturally, a DAE system with a higher index will be more complicated to convert into an ODE than one with a lower index. In Shmoylova et al. (2013), it was stated that a mechanical system with holonomic constraints is typically an index-3 system. This is also the case with the system (3.13) and (3.3) where the holonomic constraint, the latter equation, was differentiated twice to obtain the acceleration constraint (3.15), transforming the system into an index-1 system. Therefore, taking the derivative once more will transform the system into an ODE, implying the original system was an index-3 system.

When solving higher-order DAEs, a common approach is to convert it into an index-1 system using index reduction methods, e.g., Iwata et al. (2019). The importance of index reduction methods can be emphasized by the fact that the ODE solvers in MATLAB only solve index-1 DAEs, implying higher-order systems must be transformed into index-1 systems to be able to solve them using MATLAB, the reader is referred to The Mathworks (2020a) for more details.

To solve the system of equations describing the DAE system presented in last section, define the two sets of variables

$$\xi \triangleq [f_{Lx}, f_{Ly}, f_{Rx}, f_{Ry}, \ddot{\theta}^T]^T \quad (3.16a)$$

$$\zeta \triangleq [p_L^T, \dot{p}_L^T, \ddot{p}_L^T, p_R^T, \dot{p}_R^T, \ddot{p}_R^T, \theta^T, \dot{\theta}^T, V_x, V_y]^T \quad (3.16b)$$

where $\xi \in \mathbb{R}^{n+4}$ contains all the unknown algebraic variables and the second derivatives of the link angles, and $\zeta \in \mathbb{R}^{2n+8}$ the remaining variables. It is then possible to write the DAE as

$$\mathbf{0} = \mathbf{g}(\xi, \zeta), \quad (3.17)$$

where $\mathbf{g} = [g_{xL}, g_{yL}, g_{xR}, g_{yR}, g_{\theta_1}, \dots, g_{\theta_n}]^T$ contains all the equations given by (3.13)

and (3.15).

To rewrite (3.17), it can be observed how the variables in ξ never appear together in the same term. This is the case as all terms consisting of the forces $f_{(\cdot)}$ originate from the last term in (3.13) through the generalized forces, while all terms consisting of the second derivatives of the link angles originate from the first term. It is, therefore, possible to rewrite the system in the form

$$\mathbf{M}(\boldsymbol{\theta}) \xi - \mathbf{f}(\zeta) = 0, \quad (3.18)$$

where \mathbf{f} contains all the terms independent of ξ and each element in the first matrix is calculated as

$$\mathbf{M} = \{m_{ij}\} = \left\{ \frac{\partial \mathbf{g}_i}{\partial \xi_j} \right\} \in \mathbb{R}^{(n+4) \times (n+4)}, \quad (3.19)$$

i.e. the Jacobian of \mathbf{g} with respect to ξ , where $\{\mathbf{g}, \xi\}_k$ denotes the k^{th} element of the vector.

Hence, (3.18) may be solved by inverting \mathbf{M}

$$\xi = \mathbf{M}(\boldsymbol{\theta})^{-1} \mathbf{f}(\zeta). \quad (3.20)$$

By using (3.20) it is then possible to solve and integrate (3.13) and (3.15) for $\{f_{Lx}, f_{Ly}, f_{Rx}, f_{Ry}, \boldsymbol{\theta}^T\}$ given trajectories of both cable end positions and their derivatives and a given initial configuration of link angles $\boldsymbol{\theta}$ and angular link velocities $\dot{\boldsymbol{\theta}}$ satisfying the continuity constraint (3.3) and velocity constraint (3.14) respectively.

Example 3.1 | Example with $n = 2$

To demonstrate how the model presented above can be solved, let's consider the simple case where $n = 2$. Note, even in this simple case, the expressions of the hydrodynamic forces and torque (3.5) are too complicated to be calculated by hand, and the exact expressions will thus not be included in this example.

The first step when deriving the equations of motion using Lagrangian mechanics is to express the position of the center of mass for each link using the generalized coordinates. In this case, the generalized coordinates can be chosen as the two link angles θ_1 and θ_2 . The position of the center of mass for each link may then be found

to be

$$\mathbf{p}_1 = \begin{bmatrix} x_L + \frac{1}{2}L \cos \theta_1 \\ y_L + \frac{1}{2}L \sin \theta_1 \end{bmatrix}, \quad \mathbf{p}_2 = \begin{bmatrix} x_L + L \cos \theta_1 + \frac{1}{2}L \cos \theta_2 \\ y_L + L \sin \theta_1 + \frac{1}{2}L \sin \theta_2 \end{bmatrix}, \quad (3.21)$$

with the corresponding velocities

$$\mathbf{v}_1 = \begin{bmatrix} \dot{x}_L - \frac{1}{2}L\dot{\theta}_1 \sin \theta_1 \\ \dot{y}_L + \frac{1}{2}L\dot{\theta}_1 \cos \theta_1 \end{bmatrix}, \quad \mathbf{v}_2 = \begin{bmatrix} \dot{x}_L - L\dot{\theta}_1 \sin \theta_1 + \frac{1}{2}L\dot{\theta}_2 \sin \theta_2 \\ \dot{y}_L + L\dot{\theta}_1 \cos \theta_1 + \frac{1}{2}L\dot{\theta}_2 \cos \theta_2 \end{bmatrix}. \quad (3.22)$$

Next, consider the generalized forces affecting each of the generalized coordinates, in addition to the left cable end

$$Q_{\theta_1} = -f_{Rx}L \sin \theta_1 + f_{Ry}L \cos \theta_1 + F_{drag,\theta_1}(\zeta) \quad (3.23a)$$

$$Q_{\theta_2} = -f_{Rx}L \sin \theta_2 + f_{Ry}L \cos \theta_2 + F_{drag,\theta_2}(\zeta) \quad (3.23b)$$

$$Q_{x_L} = f_{Lx} + f_{Rx} + F_{drag,x_L}(\zeta) \quad (3.23c)$$

$$Q_{y_L} = f_{Ly} + f_{Ry} + F_{drag,y_L}(\zeta), \quad (3.23d)$$

where $F_{drag,(\cdot)}$ are the generalized force components due to hydrodynamic drag forces and torques. Then, the kinetic energy for the system may be found to be

$$\begin{aligned} K &= \frac{1}{2}m \left[\left(\dot{x}_L - \frac{1}{2}L\dot{\theta}_1 \sin \theta_1 \right)^2 + \left(\dot{y}_L + \frac{1}{2}L\dot{\theta}_1 \cos \theta_1 \right)^2 \right] \\ &+ \frac{1}{2}m \left[\left(\dot{x}_L - L\dot{\theta}_1 \sin \theta_1 + \frac{1}{2}L\dot{\theta}_2 \sin \theta_2 \right)^2 + \left(\dot{y}_L + L\dot{\theta}_1 \cos \theta_1 + \frac{1}{2}L\dot{\theta}_2 \cos \theta_2 \right)^2 \right] \\ &+ \frac{1}{24}mL^2 \left(\dot{\theta}_1^2 + \dot{\theta}_2^2 \right). \end{aligned} \quad (3.24)$$

After differentiating the kinetic energy according to the Euler-Lagrange equation, and some algebraic simplifications the following system of equations is obtained:

$$\begin{aligned} 0 &= -f_{Lx} - f_{Rx} + 2m\ddot{x}_L - \frac{3}{2}mL\dot{\theta}_1^2 \cos \theta_1 - \frac{1}{2}mL\dot{\theta}_2^2 \cos \theta_2 \\ &\quad - \frac{3}{2}mL\ddot{\theta}_1 \sin \theta_1 - \frac{1}{2}mL\ddot{\theta}_2 \sin \theta_2 - F_{drag,x_L}(\zeta) \end{aligned} \quad (3.25a)$$

$$\begin{aligned} 0 &= -f_{Ly} - f_{Ry} + 2m\ddot{y}_L - \frac{3}{2}mL\dot{\theta}_1^2 \sin \theta_1 - \frac{1}{2}mL\dot{\theta}_2^2 \sin \theta_2 \\ &\quad + \frac{3}{2}mL\ddot{\theta}_1 \cos \theta_1 + \frac{1}{2}mL\ddot{\theta}_2 \cos \theta_2 - F_{drag,y_L}(\zeta) \end{aligned} \quad (3.25b)$$

$$0 = -\ddot{x}_L + \ddot{x}_R + L\dot{\theta}_1^2 \cos \theta_1 + L\dot{\theta}_2^2 \cos \theta_2 + L\ddot{\theta}_1 \sin \theta_1 + L\ddot{\theta}_2 \sin \theta_2 \quad (3.25c)$$

$$0 = -\ddot{y}_L + \ddot{y}_R + L\dot{\theta}_1^2 \sin \theta_1 + L\dot{\theta}_2^2 \sin \theta_2 - L\ddot{\theta}_1 \cos \theta_1 - L\ddot{\theta}_2 \cos \theta_2 \quad (3.25d)$$

$$0 = -f_{Ry}L \cos \theta_1 + f_{Rx}L \sin \theta_1 + \frac{3}{2}m\ddot{y}_L \cos \theta_1 + \frac{4}{3}mL\ddot{\theta}_1 - \frac{3}{2}m\ddot{x}_L \sin \theta_1 \\ + \frac{1}{2}mL\ddot{\theta}_2 \cos (\theta_1 - \theta_2) + \frac{1}{2}mL\dot{\theta}_2^2 \sin (\theta_1 - \theta_2) - F_{drag,\theta_1}(\xi) \quad (3.25e)$$

$$0 = -f_{Ry}L \cos \theta_2 + f_{Rx}L \sin \theta_2 + \frac{1}{2}m\ddot{y}_L \cos \theta_2 + \frac{1}{3}mL\ddot{\theta}_2 - \frac{1}{2}m\ddot{x}_L \sin \theta_2 \\ + \frac{1}{2}mL\ddot{\theta}_1 \cos (\theta_1 - \theta_2) - \frac{1}{2}mL\dot{\theta}_1^2 \sin (\theta_1 - \theta_2) - F_{drag,\theta_2}(\xi), \quad (3.25f)$$

where the equations in (3.25) correspond to the equations for x_L , y_L , x_R , y_R , θ_1 and θ_2 respectively. The matrix \mathbf{M} is then calculated by taking the Jacobian of (3.25) with respect to ξ to obtain

$$\mathbf{M}(\xi) = \begin{bmatrix} -1 & 0 & -1 & 0 & -\frac{3}{2}mL \sin \theta_1 & -\frac{1}{2}mL \sin \theta_2 \\ 0 & 1 & 0 & -1 & \frac{3}{2}mL \cos \theta_1 & \frac{1}{2}mL \cos \theta_2 \\ 0 & 0 & 0 & 0 & L \sin \theta_1 & L \sin \theta_2 \\ 0 & 0 & 0 & 0 & -L \cos \theta_1 & -L \cos \theta_2 \\ 0 & 0 & L \sin \theta_1 & -L \cos \theta_1 & \frac{4}{3}mL^2 & \frac{1}{2}mL \cos (\theta_1 - \theta_2) \\ 0 & 0 & L \sin \theta_2 & -L \cos \theta_2 & \frac{1}{2}mL \cos (\theta_1 - \theta_2) & \frac{1}{3}mL^2 \end{bmatrix}. \quad (3.26)$$

The vector \mathbf{f} , which holds the remaining terms must then be equal to


$$\mathbf{f} = \begin{bmatrix} -2m\ddot{x}_L + \frac{3}{2}mL\dot{\theta}_1^2 \cos \theta_1 + \frac{1}{2}mL\dot{\theta}_2^2 \cos \theta_2 + F_{drag,x_L}(\xi) \\ -2m\ddot{y}_L + \frac{3}{2}mL\dot{\theta}_1^2 \sin \theta_1 + \frac{1}{2}mL\dot{\theta}_2^2 \sin \theta_2 + F_{drag,y_L}(\xi) \\ \ddot{x}_L - \ddot{x}_R - L\dot{\theta}_1^2 \cos \theta_1 - L\dot{\theta}_2^2 \cos \theta_2 \\ \ddot{y}_L - \ddot{y}_R - L\dot{\theta}_1^2 \sin \theta_1 - L\dot{\theta}_2^2 \sin \theta_2 \\ -\frac{3}{2}m\ddot{y}_L \cos \theta_1 + \frac{3}{2}m\ddot{x}_L \sin \theta_1 - \frac{1}{2}mL\dot{\theta}_2^2 \sin (\theta_1 - \theta_2) + F_{drag,\theta_1}(\xi) \\ -\frac{1}{2}m\ddot{y}_L \cos \theta_2 + \frac{1}{2}m\ddot{x}_L \sin \theta_2 + \frac{1}{2}mL\dot{\theta}_1^2 \sin (\theta_1 - \theta_2) + F_{drag,\theta_2}(\xi) \end{bmatrix}. \quad (3.27)$$

To check when the matrix is non-singular, and thus can be inverted to solve the system, the determinant is calculated to be

$$\det(\mathbf{M}) = L^4 \sin^2 (\theta_1 - \theta_2), \quad (3.28)$$

which is non-zero whenever $\theta_1 \neq \theta_2$. Hence, the system is well-defined, and a solution can be found, as long as the cable configuration is not equivalent to a straight line. The intuition behind this is trivial, as this case will only occur if the

euclidean distance between the two vessels, where the cable ends are connected, is equal to the total length of the cable. In this case, an infinite force will be required to ensure the cable's continuity as the cable would break if the euclidean distance between the vessels is larger than the total length of the cable. Thus, it can be concluded that the simple system considered in this example is well defined as long the euclidean distance between the two cable ends are strictly less than the total length of the cable.

End Example 3.1 

3.3.1 Practical implementation

Due to the size and complexity of the system when n increases, it is not feasible to calculate the equations of motion for the system by hand. Instead, another approach was taken where the equations were implemented in the symbolic programming language *Wolfram Language*, see Wolfram Research (2020), which performs all the calculations described in Section 3.2 symbolically. The equations are then transformed into the form of (3.18). Finally, the program creates a file of a MATLAB function that takes all the required states ζ as input parameters and returns the matrix \mathbf{M} and the vector \mathbf{f} . The MATLAB function may then be called at each time step in the simulation in MATLAB to calculate \mathbf{M} and \mathbf{f} given the current states, before solving the system with (3.20).

In general, increasing the number of links would yield better resolution and be more accurate as the link length would be smaller. However, with the currently available processing capacity, it was found that $n = 20$ is the upper limit on the number of links to use for the cable mode. This is due to processing and memory limitations, both during the model derivation using *Wolfram Language* and the compile and run-time of the generated model in MATLAB/Simulink.

Remark 3.2. *An attempt deriving the equations of motion using the Matlab Symbolic Toolbox The MathWorks (2020b) was also done. However, while being simpler to use than Wolfram Language, it lacked performance and suffered from a long computational time when performing the symbolic calculations. When the number of links increased ($n = 10$), it had still not managed to calculate the kinetic energy expression when stopped after 24 hours. In comparison, the same calculations take just about 30 min in Wolfram Language for $n = 10$, and about 48 h for $n = 20$.*

Remark 3.3. *The implementation described above is not entirely self-developed but rather heavily influenced by the existing implementation from Bhattacharya (2020a). This code, which already implemented the full model as presented in Bhattacharya et al. (2011), was used as a starting base. It has further been extended to incorporate ocean currents and export the finished model to a MATLAB compatible format by the author of this thesis.*

3.4 Connection with vessel

This section aims to connect the cable model presented in this chapter with the vessel model presented in Chapter 2. Firstly, the necessary theory needed to calculate how the exerted forces by the cable on each of the vessels will affect the vessel dynamics will be provided. Then, the position, velocity, and acceleration (PVA) of the cable endpoints are calculated based on the position of CO for the vessel.

An illustration of how the end point of the cable is connected to the vessel in the point C is illustrated in Figure 3.2.

3.4.1 Cable forces

To calculate the impact on the vessel dynamics from the additional forces on the vessel from the cable, the forces must be transformed to the body-fixed coordinate system of each vessel such that they can be used in (2.1b). First, the reactive force on the vessel from the cable, expressed in $\{c\}$ can be calculated as

$$\tau_{\text{cable}}^c = \mathbf{R}_{z,\psi} \begin{bmatrix} -f_{i,x} \\ -f_{i,y} \\ 0 \end{bmatrix}, \quad (3.29)$$

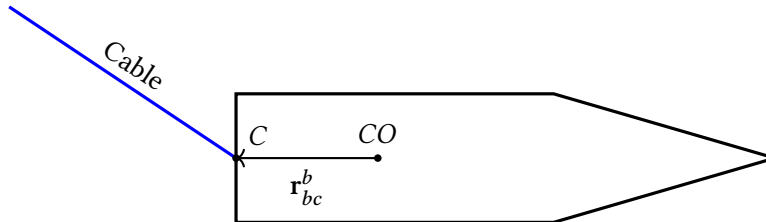


Figure 3.2: Illustration of connection between cable and vessel

where $f_{i,x}$ and $f_{i,y}$, $i \in \{L, R\}$ are the forces, expressed in $\{n\}$, on the left and right cable ends from each vessel respectively. The negative signs arise from Newton's third law of motion as the reactive forces on the vessels from the cable is opposite from the forces on the cable from the vessels. To transform the forces expressed in $\{c\}$ to $\{b\}$, the system transformation matrix from Fossen (2011) is used, which in 3-DOF takes the form of

$$\mathbf{H}(\mathbf{r}_{bc}^b) = \begin{bmatrix} 1 & 0 & -y_{bc}^b \\ 0 & 1 & x_{bc}^b \\ 0 & 0 & 1 \end{bmatrix}, \quad (3.30)$$

where \mathbf{r}_{bc}^b is the vector from CO to C expressed in $\{b\}$, as illustrated in Figure 3.2. The force can then be transformed from $\{c\}$ to $\{b\}$ as

$$\boldsymbol{\tau}_{\text{cable}}^b = \mathbf{H}(\mathbf{r}_{bc}^b)^T \boldsymbol{\tau}_{\text{cable}}^c, \quad (3.31)$$

which is included in (2.1b) to add the forces from the cable in the vessel dynamics.

3.4.2 PVA of cable end points

One of the requirements when simulating the cable model presented in this chapter is that the position, velocity, and acceleration (PVA) of the cable endpoints are known, as these states are used as inputs to the model. However, the PVA of the point C must be calculated from the vessel's PVA in CO as the cable is not attached directly to CO of the vessels.

First, it can be observed that the position of C can be found by the translation

$$\boldsymbol{\eta}_c^n = \boldsymbol{\eta}_b^n + \mathbf{R}_{z,\psi} \mathbf{r}_{bc}^b, \quad (3.32)$$

where $\boldsymbol{\eta}_b^n$ is the position of the vessel, the point CO, expressed in $\{n\}$. Next, the velocity is found by taking the time-derivative

$$\dot{\boldsymbol{\eta}}_c^n = \dot{\boldsymbol{\eta}}_b^n + \dot{\mathbf{R}}_{z,\psi} \mathbf{r}_{bc}^b + \mathbf{R}_{z,\psi} \dot{\mathbf{r}}_{bc}^b \quad (3.33)$$

$$= \mathbf{R}_{z,\psi} \mathbf{v}^b + \mathbf{R}_{z,\psi} \mathbf{S} \begin{pmatrix} 0 \\ 0 \\ r \end{pmatrix} \mathbf{r}_{bc}^b, \quad (3.34)$$

where the last term in (3.33) is zero as the vector from CO to C is constant in $\{b\}$, \mathbf{v}^b the velocity of the vessel in $\{b\}$, r the yaw rate and $\mathbf{S}(\cdot)$ the skew-symmetric matrix. Finally, the acceleration is found by taking the time-derivative of (3.34) to obtain

$$\ddot{\mathbf{q}}_c^n = \dot{\mathbf{R}}_{z,\psi} \mathbf{v}^b + \mathbf{R}_{z,\psi} \dot{\mathbf{v}}^b + \dot{\mathbf{R}}_{z,\psi} \mathbf{S} \begin{pmatrix} 0 \\ 0 \\ r \end{pmatrix} \mathbf{r}_{bc}^b + \mathbf{R}_{z,\psi} \dot{\mathbf{S}} \begin{pmatrix} 0 \\ 0 \\ r \end{pmatrix} \mathbf{r}_{bc}^b + \mathbf{R}_{z,\psi} \mathbf{S} \begin{pmatrix} 0 \\ 0 \\ r \end{pmatrix} \dot{\mathbf{r}}_{bc}^b \quad (3.35)$$

$$= \underbrace{\mathbf{R}_{z,\psi} \mathbf{S} \begin{pmatrix} 0 \\ 0 \\ r \end{pmatrix} \mathbf{v}^b}_{\ddot{\eta}_b^n} + \underbrace{\mathbf{R}_{z,\psi} \dot{\mathbf{v}}^b}_{\text{Centripetal acceleration}} + \underbrace{\mathbf{R}_{z,\psi} \mathbf{S}^2 \begin{pmatrix} 0 \\ 0 \\ r \end{pmatrix} \mathbf{r}_{bc}^b}_{\text{Traversal acceleration}} + \underbrace{\mathbf{R}_{z,\psi} \mathbf{S} \begin{pmatrix} 0 \\ 0 \\ \dot{r} \end{pmatrix} \mathbf{r}_{bc}^b}_{\text{Traversal acceleration}}, \quad (3.36)$$

where \dot{r} is the derivative of the yaw rate, i.e. the yaw acceleration.

When looking at the PVA equations, it is clear how the lever arm from CO to C introduces new terms arising from Traversal and Centripetal acceleration. However, it can be observed that there are no Coriolis terms present in (3.36) as there are no motion of C in $\{b\}$ relative to CO.

3.5 Model verification

In this section, the model will be simulated under different scenarios to verify the model behavior.

3.5.1 Ocean currents

The purpose of this scenario is to verify that the new hydrodynamic drag model presented in Section 3.2.2 exhibits behavior as expected when exposed to an environment where ocean currents are present. In the scenario considered here, the cables' endpoints are attached to two stationary poles located in the middle of an irrotational and constant ocean current. The system is then simulated to analyze how the ocean currents will affect the cable motion.

The simulation results are presented in Fig. 3.3. The figure shows that the cable converges to the form of a catenary when exposed to ocean currents, which minimizes the hydrodynamic impact on the cable. Bhattacharya et al. (2011) showed that the steady-state solution of the cable, when the motion of both ends was equal to constant parallel velocities, would take the shape of a catenary. As the scenario

considered here is equivalent to a cable with constant parallel velocities of the ends with no ocean currents, it is expected that the same steady-state solution would be seen here.

Further, the cable in this scenario displays a clear analogy to a hanging cable influenced by gravity, which is also well known to take the shape of a catenary, minimizing the potential energy of the cable. By observing that the irrotational constant ocean current is analogous to a uniform gravitational field, it is no surprise that the cable takes the shape of a catenary.

Looking at Fig. 3.3, it is safe to conclude that the extended hydrodynamic drag model presented in Section 3.2.2 produces a realistic cable motion similar to what is expected when considering the steady-state solution.

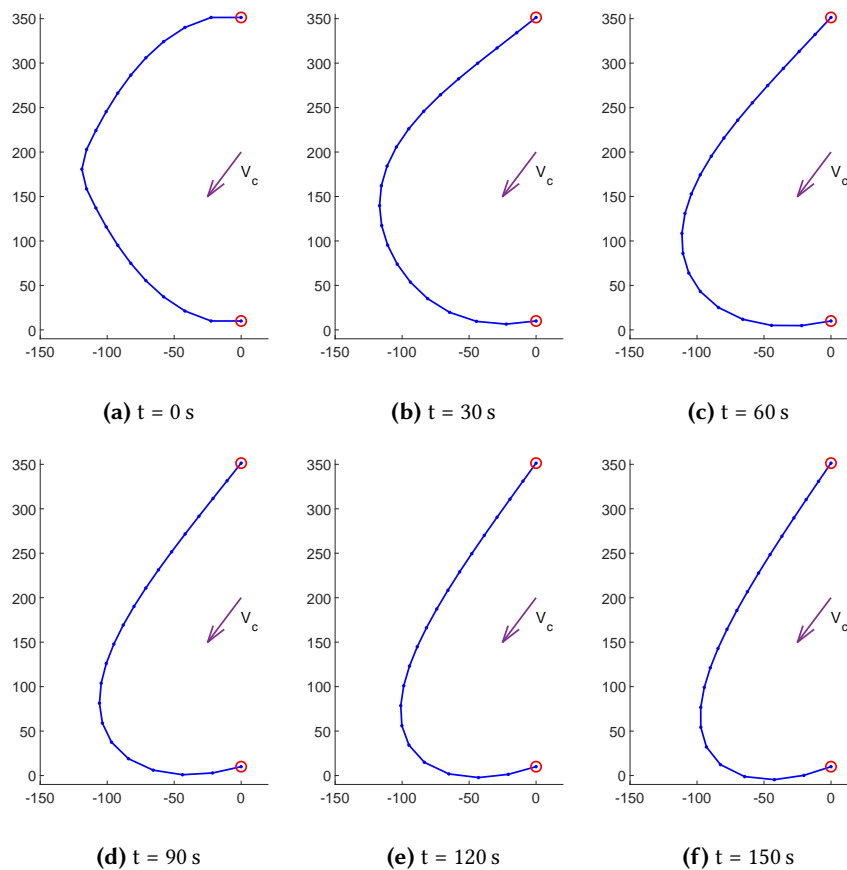


Figure 3.3: Cable affected by constant ocean currents.

3.5.2 Drag coefficients

The purpose of this section is to find reasonable estimates of the parallel and perpendicular drag coefficients in (3.5) to improve the transient phase of the cable concerning the load experienced on each vessel from the cable.

While the steady-state solution of the cable was confirmed to be reasonable in the last section, it is difficult to conclude anything of the transient response of the cable from this simple scenario as the transient phase is heavily determined by choice of drag coefficient values.

The transient response of the cable is investigated by comparing data logged from full-scale experiments performed by FFI with the simulated behavior. In the experiment, the vessels were controlled using a leader-follower method on the straight-line path segments. Due to limitations in the leader-follower method, the vessels were controlled manually throughout the turns to maintain the desired formation.

During the tests, data such as the positions and body-fixed velocities of the vessels were logged. Also, the experienced load on the vessels from the cable was measured using a load cell. The goal is not to find drag coefficients corresponding to a perfect one-to-one matching with experimental data due to the complicated nature of the system dynamics. Instead, the goal is to find drag coefficients such that the experienced load on the vessels from the cable, in simulation, will be within the same order of magnitude to the experimental data.

The logged movement of the vessels was used as the endpoints of the cable, to recreate the experiments. Using the vessels' recorded positions from experiments as direct inputs to the cable model eliminates any impacts caused by the model uncertainties of the vessel model in Chapter 2. This way, it is possible to isolate the cable model's behavior, allowing a more accurate comparison.

To simulate the cable dynamics, the PVA of the cable's endpoints must be known. To recreate the experiments, the PVA of both vessels must, therefore, be calculated. This imposed a challenge as only the positions (latitude and longitude) and body-fixed velocities were logged during the experiments. Hence, an attempt to recalculate the vessels' PVA from these data was done by numerical differentiation of the available data.

For the following simulation, the number of rigid links is chosen as $n = 20$. The numerical values of the total mass, length, and drag coefficients of the cable used in the simulation are not given in this thesis on request from FFI. This is done to avoid the possibility of recreating the exact cable model used, as FFI has requested that the

experienced load from the cable remains confidential.

The cable model was then implemented in MATLAB/Simulink, according to Section 3.3.1. Moreover, the simulation is performed without ocean currents as it is unknown if, and what the ocean current was during the tests. The mismatch in ocean currents could be a potential error source, but simulating with no ocean currents, will introduce less error than simulating with the wrong ocean currents, thus minimizing the impact.

The resulting loads from the simulation with the chosen drag coefficients, along with the experimental data, is plotted in Fig. 3.4a, while the corresponding surge speed of the vessels are found in Fig. 3.4b. It can be seen that the cable model, with the given choice of drag coefficients, gives an experienced load within the same order of magnitude to the experimental data.

The figures show that the simulated load matches well with the experimental data for the first three periods, which are similar when considering the surge speed characteristics under each of these periods. For the fourth period, between $t = 700$ s and 1000 s, the simulated load deviates a bit more from the experimental data, where the vessel had somewhat higher surge speeds. This indicates that the linear drag model (3.5) is less accurate when the speed increases.

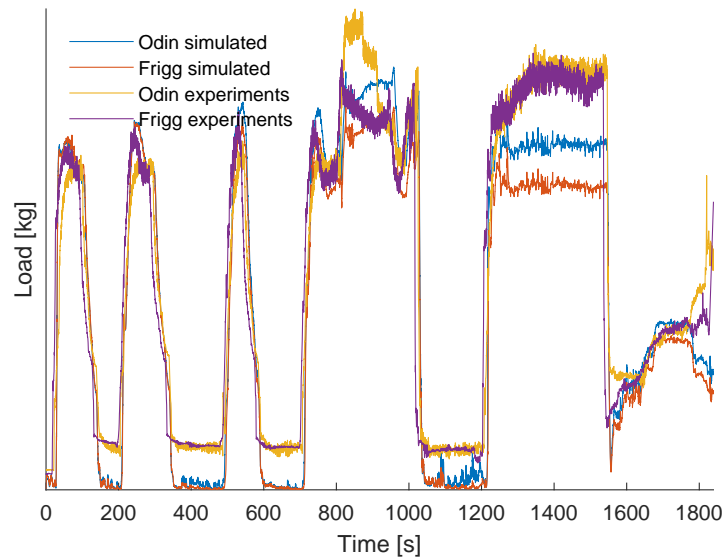
However, it can be noticed that the simulated load does not match the experimental for the last period between $t = 1200$ s and 1500 s. By looking at Fig. 3.4b, the surge speeds during this period are equal, and even a bit smaller, in magnitude compared with the first three periods. However, the recorded loads are much higher than the load for the first three periods, almost at the same level as the fourth period. The simulated loads, on the other hand, are similar in this period as the first three.

It is unknown why the recorded load of the last period differs so much, and it is probably the reason for the mismatch between the simulated cable model and the experimental data as the simulated loads are similar in magnitude to the three first periods.

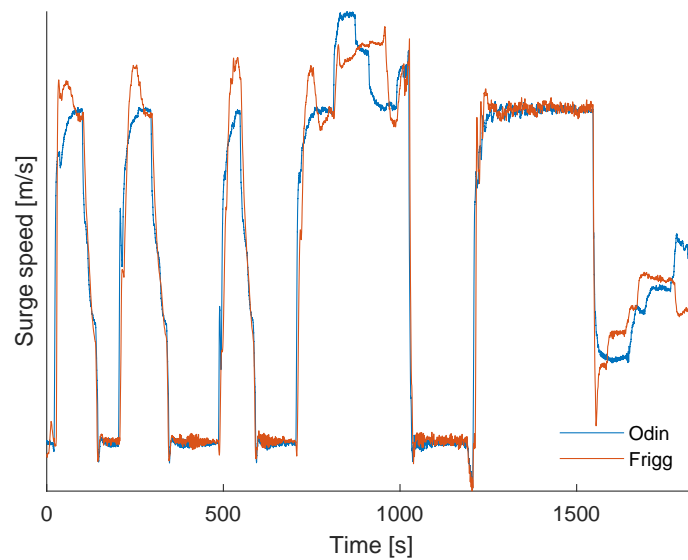
During the last period, different simulated loads for Odin and Frigg can be observed. The mismatch is likely to be caused by how PVA had to be obtained through numerical differentiation. An implication of this is that the cable model's velocity and acceleration constraints are no longer necessarily satisfied at each time step of the simulation. Hence, throughout the simulation, the position of the right endpoint and the vessel's position diverge a bit, causing Odin to be positioned a bit before Frigg towards the end of the simulation. Hence Odin experience a higher load as it must tow a more substantial amount of the cable than Frigg. The diverge

is a direct result of the numerical differentiation required to obtain the vessels PVA and is avoided if the vessels' trajectories are generated such that the velocity and acceleration constraints are satisfied at all times. However, this has no significant effect on the results as the experienced loads for both vessels are still within the same order of magnitude.

Regardless of the mismatch during the last period, it can be concluded that the linear drag model (3.5) is a reasonable approximation for the low-speed applications considered in this thesis and that the experienced load on the vessels from the cable will be within the same order of magnitude as experienced in experiments.



(a) Load from cable on vessels.



(b) Logged surge speed of vessels from experiments.

Figure 3.4: Comparison of simulation vs. experiments. Plotted without numerical data on request by FFI.

4 | Formation Control

In this chapter, a method for formation control of two underactuated USVs using the NSB framework is presented. First, a brief introduction to the field of behavioral-based formation control methods is given. Then, the mathematical foundation of the NSB framework is presented, and the interface between the formation control system and the maneuvering controllers is established. Next, the different tasks for the NSB framework are then presented, including the proposal of a new definition of the barycenter task, inspired by line-of-sight methods. Then, rigorous closed-loop stability analysis for the formation and barycenter tasks are performed in the ideal case with no model uncertainties, using the vessel model and autopilots from Moe et al. (2016). Finally, the robustness properties against nonvanishing perturbations are investigated to see how the cable dynamics affect the tasks' errors.

4.1 Introduction

When designing autonomous systems, they must be designed to have the autonomy to plan and navigate complex environments, with often dynamically changing areas, in real-time. These environments can be intricate to describe mathematically, making it difficult to design a single control law fusing all available information at once. Alternatively, an idea to overcome this issue is to divide the overall objectives into several sub-problems that are simpler to solve individually. The solutions from each sub-problem may then be combined to obtain a solution that will hopefully fulfill the overall objectives. Instead of considering an objective like "*Move from point A to point B without colliding*," it could be split into the two sub-problems (1) "Maintain a minimum distance to all obstacles" and (2) "Move towards the target location."

This concept builds up the foundation of behavioral-based methods. To handle complex missions, behavioral-based methods usually decompose the problem into a set of simple tasks, which are solved independently and then combined to solve the mission. While the introduction of fundamental tasks simplifies the planning,

caution must be taken when combining the individual task solutions. In particular, when different tasks counteract, meaning a single solution cannot satisfy all, a proper policy must be applied to minimize the conflict among the tasks.

In general, behavioral methods may be divided into two classes depending on how the solutions are combined, which are *competitive* and *cooperative*. An example of a competitive scheme is the *layered control system* (LCS) Brooks (1986) where each task, working independently, is assigned a priority level, and higher-priority tasks solve conflicts by subsuming the lower ones. The implications are that only the highest-priority task is correctly achieved, and lower-priority tasks are only allowed to influence the decision once the first task is fulfilled. Instead of all tasks cooperating to solve the overall goal, they are competitive and subsume lower-level tasks until they are fulfilled themselves.

In a cooperative scheme, on the other hand, instead of the individual task competing against each other, the output of each task is combined using a weighted sum according to their priority, meaning no task is fully achieved but rather a compromise of the relative task weightings. An example using this approach is the *motor schema control* (MSC) Arkin (1989); Balch and Arkin (1998).

Another example of a cooperative scheme is the *Null-Space-Based behavioral control* (NSB) presented in Antonelli and Chiaverini (2003, 2006), which uses a different approach to combine the task solutions. Instead of using a weighted sum, causing no task to be fully achieved, the solutions of the different tasks are combined by projecting the solution from one task onto the null-space of the higher-priority task. By the projection, all components from the lower-priority tasks which would conflict with higher-priority tasks are therefore removed, also allowing lower priority tasks to be fulfilled as long they do not counteract the other tasks. In Antonelli et al. (2005) the three methods are compared, and showed that NSB will perform better than MSC and LCS for obstacle avoidance and path following for mobile robots.

The NSB method was first used to coordinate a platoon of marine surface vessels in Arrichiello et al. (2006a,b). In Arrichiello et al. (2006a), the method was applied for vessels that are underactuated at high velocities and fully-actuated at low-velocities, while the vessel is underactuated at all velocities in Arrichiello et al. (2006b). In this case, the NSB system can be seen as a centralized guidance block, which outputs an individual velocity for each vessel to achieve the desired behavior using state measurements from all vessels Fig. 4.1. The task of controlling the dynamics are left up to the maneuvering controller of each vessel. Hence, the NSB system can focus on the kinematics needed to fulfill the tasks, rather than the control.

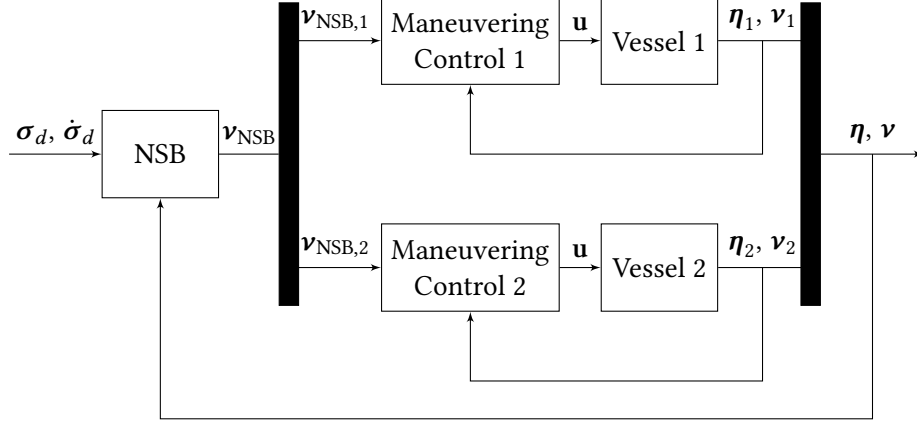


Figure 4.1: Overview of centralized NSB guidance system. Inspired by (Arrichiello et al.; 2006b, Figure 1).

4.2 NSB mathematics

In the NSB framework, for each task, a task variable $\sigma \in \mathbb{R}^m$ to be controlled is defined as

$$\sigma = \mathbf{f}(\mathbf{p}), \quad (4.1)$$

where $\mathbf{p} = [\mathbf{p}_1^T \ \dots \ \mathbf{p}_n^T]^T \in \mathbb{R}^{pn}$ is the concatenated vector of system configurations, where $\mathbf{p}_i \in \mathbb{R}^p$ is the configuration for system i , and $\mathbf{f}: \mathbb{R}^{pn} \rightarrow \mathbb{R}^m$ is the task function which maps the system configuration to the task variable. In this thesis, the vessel positions are used as the system configuration, i.e. $\mathbf{p} \in \mathbb{R}^{2n}$ contains the position of all vessels.

With the expression of the task variable, the goal is to find trajectories of $\mathbf{p}(t)$ such that

$$\lim_{t \rightarrow \infty} \sigma_d(t) - \sigma(t) = 0, \quad (4.2)$$

where $\sigma_d(t) \in \mathbb{R}^m$ is the desired task value. The differential relationship between the task variable derivative and the system velocities, is found by taking the derivative of (4.1)

$$\dot{\sigma} = \sum_{i=1}^n \frac{\partial \mathbf{f}(\mathbf{p})}{\partial \mathbf{f}(\mathbf{p}_i)} \mathbf{v}_i = \mathbf{J}(\mathbf{p}) \mathbf{v}, \quad (4.3)$$

where $\mathbf{J} \in \mathbb{R}^{m \times pn}$ is the configuration-dependent task Jacobian matrix, and $\mathbf{v} = [\mathbf{v}_1^T \ \dots \ \mathbf{v}_n^T]^T \in \mathbb{R}^{2n}$ the vessel velocities. To generate desired motion references $\mathbf{p}_d(t)$ for the vessels from the desired task function $\sigma_d(t)$ an effective way is to act at the differential level by inverting the locally linear mapping (4.3) Arrichiello

(2006). Thus, to generate reference velocities for the vessels, (4.3) is inverted using the Moore-Penrose pseudoinverse

$$\mathbf{v}_d = \mathbf{J}^\dagger \dot{\boldsymbol{\sigma}}_d. \quad (4.4)$$

However, to reduce numerical drift during discrete-time integration of (4.4), feedback is added to obtain a Closed Loop Inverse Kinematics (CLIK) form, see for instance Arrichiello et al. (2006b)

$$\mathbf{v}_d = \mathbf{J}^\dagger (\dot{\boldsymbol{\sigma}}_d + \Lambda \tilde{\boldsymbol{\sigma}}), \quad (4.5)$$

where $\Lambda \in \mathbb{R}^{m \times m} > 0$ is a matrix of proportional gains and $\tilde{\boldsymbol{\sigma}} = \boldsymbol{\sigma}_d - \boldsymbol{\sigma}$ the task error. It can be observed how this closed-loop form is equivalent to a P-controller of the task error tracking the possibly time-varying $\boldsymbol{\sigma}_d$, which is transformed from task-space to Cartesian coordinates through the Jacobian.

Lemma 4.1. *Consider the task function (4.1) with the CLIK control law (4.5). Furthermore, assume that the system velocities perfectly follows the reference \mathbf{v}_d from (4.5), i.e. $\mathbf{v} = \mathbf{v}_d$. Then, the closed-loop system is UGES if the configuration-dependent task Jacobian has full row rank, that is $\mathbf{J}\mathbf{J}^T$ invertible.*

Proof. By inserting (4.5) into (4.3), under the assumption $\mathbf{v} = \mathbf{v}_d$, the following closed-loop task function dynamics is obtained

$$\dot{\boldsymbol{\sigma}} = \mathbf{J}\mathbf{v}_d \quad (4.6)$$

$$= \mathbf{J}\mathbf{J}^\dagger (\dot{\boldsymbol{\sigma}}_d + \Lambda \tilde{\boldsymbol{\sigma}}). \quad (4.7)$$

In the case where the configuration-dependent task Jacobian has full rank, $\mathbf{J}\mathbf{J}^\dagger = \mathbf{I}$ as

$$\mathbf{J}\mathbf{J}^\dagger = \mathbf{J}\mathbf{J}^T (\mathbf{J}\mathbf{J}^T)^{-1} = \mathbf{I}. \quad (4.8)$$

This gives the task function error dynamics

$$\dot{\tilde{\boldsymbol{\sigma}}} = -\Lambda \tilde{\boldsymbol{\sigma}}. \quad (4.9)$$

Using the C^1 Lyapunov Function Candidate (LFC) $V(\tilde{\boldsymbol{\sigma}}) = \frac{1}{2} \tilde{\boldsymbol{\sigma}}^T \tilde{\boldsymbol{\sigma}}$ for which

$$\dot{V} = -\tilde{\boldsymbol{\sigma}}^T \Lambda \tilde{\boldsymbol{\sigma}} \quad (4.10)$$

clearly satisfies the conditions of (Khalil; 2002, Theorem 4.10). Thus, the system is UGES and UGAS under the conditions given in Lemma 4.1, a result also shown in

Arrichiello (2006). □

4.2.1 Merging multiple tasks

While (4.5) will make the task variable converge to its desired value for a single task case, fulfilling (4.2), a method for merging different task output velocities is needed in the case of multiple tasks. As previously discussed, the NSB framework solves this by projecting the solution from one task onto the null-space of the higher-priority task. First, consider the i^{th} task velocity chosen in analogy of (4.5)

$$\mathbf{v}_i = \mathbf{J}_i^\dagger (\dot{\boldsymbol{\sigma}}_{i,d} + \Lambda_i \tilde{\boldsymbol{\sigma}}_i). \quad (4.11)$$

Now, let the subscript i also denote the priority of the task, i.e. task 1 has the highest priority followed by task 2 the second highest etc. The velocities of each task can then be combined by

$$\mathbf{v}_d = \mathbf{v}_1 + \left(\mathbf{I} - \mathbf{J}_1^\dagger \mathbf{J}_1\right) \left[\mathbf{v}_2 + \left(\mathbf{I} - \mathbf{J}_2^\dagger \mathbf{J}_2\right) \mathbf{v}_3 \right], \quad (4.12)$$

where \mathbf{I} is the identity matrices of appropriate dimensions. It is clear how components from lower-priority tasks that would conflict higher-priority tasks are removed through the projection onto the null-space of the task above. The implication is that the highest-priority task always will be fulfilled, while the lower-priority tasks are fulfilled as long they are compatible with the higher-priority task goals.

For illustrative purposes, this can clearly be seen when considering a geometrical interpretation of (4.12) in an example with two tasks. By defining the null-space $\mathcal{N}_i \in \mathbb{R}^{pn \times pn}$ of task i as

$$\mathcal{N}_i = \mathbf{I} - \mathbf{J}_i^\dagger \mathbf{J}_i, \quad (4.13)$$

a geometrical interpretation of (4.12) is illustrated in Fig. 4.2. Here, the task output \mathbf{v}_2 is projected onto the null-space of \mathbf{v}_1 , removing the components of \mathbf{v}_2 conflicting with \mathbf{v}_1 , to create the final output (blue vector).

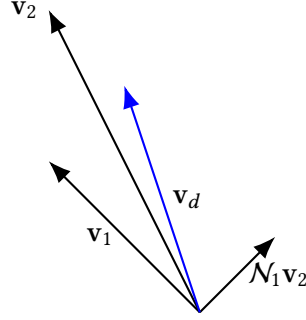


Figure 4.2: Geometric interpretation of combining velocities through null-space projections

4.3 Maneuvering Controller interface

In order to use the NSB guidance system with the low-level maneuvering controllers of Odin and Frigg, the NSB output will need to be converted. As shown in Fig. 4.1 and (4.12), the output from the guidance system is a vector with the desired velocities for the vessel given in the inertial frame. However, the maneuvering controllers in Section 2.4 require references for surge and heading. Hence, the velocity vector must first be decomposed into surge and course references

$$U_{\text{NSB}} = \|\mathbf{v}_{\text{NSB}}^n\|_2 \quad (4.14a)$$

$$\chi_{\text{NSB}} = \text{atan2}(v_{\text{NSB}}^n, u_{\text{NSB}}^n), \quad (4.14b)$$

where $\mathbf{v}_{\text{NSB}}^n = [v_{\text{NSB}}^n \ u_{\text{NSB}}^n]^T$ is the NSB output velocity vector for each vessel, where the subscript i denoting each vessel is omitted for simplicity. Further, this is converted to the surge and heading references for the maneuvering controllers by

$$u_d = U_{\text{NSB}} \frac{1 + \cos(\chi_{\text{NSB}} - \chi)}{2} \quad (4.15a)$$

$$\psi_d = \underbrace{\chi_{\text{NSB}} - \arctan\left(\frac{v^b}{u_d}\right)}_{\beta_d}, \quad (4.15b)$$

where the last term of (4.15b) is the desired crab angle of the vessel, i.e. the angle between the surge and total speed when $u = u_d$, and (4.15a) was first used in Arrichiello et al. (2006b).

4.4 Tasks

When using a behavioral-based approach, the overall mission must be decomposed into several fundamental tasks. For the overall objectives considered in this thesis Section 1.3, the three following fundamental tasks are chosen:

1. Obstacle Avoidance - Maintain a safe distance between themselves.
2. Formation - Both vessels should align themselves such that the vector between them is perpendicular to the path.
3. Barycenter - The barycenter of the vessels should follow a defined trajectory.

4.4.1 Obstacle Avoidance

When operating several vessels close to each other, maintaining the integrity of the vessel by avoiding other vessels and obstacles is of crucial importance. Thus, this task is run with the highest priority to maintain a minimum safe distance from each vessel to any other objects, including the other vessel.

Using the definition from Arrichiello et al. (2006b), the obstacle avoidance task variable is defined as the Euclidean distance between the vessel i and any obstacle or objects o , located at the position $\mathbf{p}_o \in \mathbb{R}^2$, which should be kept above a minimum distance $d_o \in \mathbb{R}_{>0}$ at all times. As an obstacle may be close to one vessel, but far from the other, the obstacle avoidance task function is defined individually for each vessel.

$$\sigma_o = \|\mathbf{p}_i - \mathbf{p}_o\| \in \mathbb{R} \quad (4.16a)$$

$$\sigma_{o,d} = d_o. \quad (4.16b)$$

The Jacobian may then be calculated as

$$\mathbf{J}_o = \frac{\partial}{\partial p_i} \|\mathbf{p}_i - \mathbf{p}_o\| = \frac{(\mathbf{p}_i - \mathbf{p}_o)^T}{\|\mathbf{p}_i - \mathbf{p}_o\|} = \hat{\mathbf{r}}^T. \quad (4.17)$$

Thus, the Jacobian is equal to the unit vector between the vessel and obstacle position. By calculating the null-space matrix

$$\mathcal{N}_i = \mathbf{I} - \hat{\mathbf{r}}\hat{\mathbf{r}}^T \quad (4.18)$$

it can be seen that when projecting lower-priority tasks into the null-space of this task, all components not parallel to the tangent of the circle of radius d_o around \mathbf{p}_o will be removed.

For the application considered in this thesis, it is assumed that no external obstacles will be present in the area of operation. Thus, the only obstacle will be the other vessel, implying that the only time the task will be activated is when the vessels are too close to each other to avoid a collision. Thus, when the inter-vessel distance is above the threshold d_o , this task is deactivated, meaning it will not conflict the mission during regular operation.

4.4.2 Formation

The second task aims to keep the vessels in the desired formation relative to the barycenter. As the vessels will be physically connected for the application considered, the vessels must keep their formation with the desired inter-vessel distance at all times. Thus, this task is run with the second-highest priority, meaning it will have the highest priority during regular operation when the obstacle avoidance task is deactivated.

For the application considered, where the vessels are towing a cable, it is desirable that the vessels should maintain a desired cross-track distance $d_f \in \mathbb{R}_{>0}$ from the barycenter $\mathbf{p}_b \in \mathbb{R}^2$ perpendicular to the path, while maintaining a zero along-track offset. The formation task function is chosen as

$$\boldsymbol{\sigma}_f = \|\mathbf{p}_1 - \mathbf{p}_b\| \in \mathbb{R}^2, \quad (4.19)$$

where \mathbf{p}_1 is the position of vessel 1, and \mathbf{p}_b is given by (4.26). As the vessels are required to maintain a desired cross-track distance perpendicular to the path, the desired task function value is expressed in the *path tangential frame*

$$\boldsymbol{\sigma}_{f,d}^p = \begin{bmatrix} 0 & \pm d_f \end{bmatrix}^T \quad (4.20)$$

$$\boldsymbol{\sigma}_{f,d} = R(\gamma_p(\theta))^T \boldsymbol{\sigma}_{f,d}^p \quad (4.21)$$

where choosing a positive sign for d_f corresponds to that vessel 1 should be positioned on the starboard side of the formation, while a negative sign corresponds to the port side. It should be noted how the desired position of vessel 2 is implicitly defined through (4.19) even as only the desired position of vessel 1 is explicitly defined. As the barycenter is defined as the midpoint between the vessels, specifying a desired

position of vessel 1 relative to the barycenter implies that the other vessel must be positioned at an equally mirrored position through the barycenter.

Similarly, the matrix of proportional gains, Λ_f^p are specified in terms of the *path tangential frame* to be able to specify the gains for along- and cross-track errors independently. Specifying the matrix in the *path tangential frame* allows independent tuning of the along- and cross-track errors, which would otherwise not be possible if the matrix was specified in the inertial frame directly. Hence, the matrix of proportional gains, expressed in the inertial frame, is equal to

$$\Lambda_f = \mathbf{R}(\gamma_p(\theta))^T \Lambda_f^p. \quad (4.22)$$

Calculating the Jacobian of (4.19) it can easily be verified to be equal to

$$\mathbf{J}_f = \begin{bmatrix} 1 - \frac{1}{2} & 0 & -\frac{1}{2} & 0 \\ 0 & 1 - \frac{1}{2} & 0 & -\frac{1}{2} \end{bmatrix}. \quad (4.23)$$

Proposition 4.1. *Consider the formation task function (4.19) with the configuration-dependent task Jacobian (4.23). Further, assume that the system velocities perfectly follow the reference $\mathbf{v}_{d,f}$. Then, the Jacobian fulfills the conditions of Lemma 4.1 and the formation task error dynamics is UGES.*

Proof. Given the Jacobian Eq. (4.23), and the fact that it has full row rank it is straight forward to verify that

$$\mathbf{J}\mathbf{J}^T = \begin{bmatrix} \frac{1}{2} & 0 & -\frac{1}{2} & 0 \\ 0 & \frac{1}{2} & 0 & -\frac{1}{2} \end{bmatrix} \begin{bmatrix} \frac{1}{2} & 0 \\ 0 & \frac{1}{2} \\ -\frac{1}{2} & 0 \\ 0 & -\frac{1}{2} \end{bmatrix} = \frac{1}{2} \begin{bmatrix} 1 & 0 \\ 0 & 1 \end{bmatrix} \quad (4.24)$$

which clearly is invertible. Thus, the conditions of Lemma 4.1 is fulfilled and the formation task dynamics is UGES under the assumptions that $\mathbf{v} = \mathbf{v}_{d,f}$, concluding the proof of Proposition 4.1. \square

It should be observed how the task function definition (4.19) differs from the definitions used in other literature using a rigid formation task definition such as Arrichiello et al. (2006b); Pereda et al. (2011); Eek (2019), where the desired position of all vessels relative to the barycenter is specified.

While the definitions used in these works are easy to understand, they are not

well-posed as the rows are linearly dependent. Thus, the Jacobian has not full row rank, an observation first made in Antonelli et al. (2008), with the implications that the conditions for Proposition 4.1 is no longer fulfilled, and neither UGES or UGAS may be proven for the task error dynamics. Additionally, it would affect the stability analysis in Section 4.4.4 as the conditions of Proposition 4.3 would no longer be fulfilled since the barycenter and formation tasks are no longer orthogonal.

By using the reduced task function (4.19), as proposed in Antonelli et al. (2008), the nice interpretation of Arrichiello et al. (2006b); Pereda et al. (2011); Eek (2019) is lost, but it is possible to prove UGES for the task individually according to Proposition 4.1, and UGAS for the formation and barycenter tasks combined according to Proposition 4.3.

4.4.3 Barycenter

The last task, running at the lowest priority, is the barycenter task, which aims to move the barycenter of the vessels along the desired path. Consequently, this task will only take effect when the desired velocities for path following do not conflict with the velocities needed to maintain the desired formation. This way, it is ensured that the vessels will prioritize keeping the formation over following the path, which is essential when the vessels are physically connected.

Traditionally when this task is incorporated into the NSB framework, it is defined using a task function which is then solved using the CLIK control law (4.5) similarly to the two previous task definitions. However, as covered in Eek (2019), this approach gave a rather slow convergence towards the desired path compared to other approaches such as the integral Line-of-Sight (ILOS) method proposed in Belleter and Pettersen (2014). Furthermore, attempts to decrease the convergence time by increasing the proportional gain matrix Λ , see (4.5), introduced unwanted oscillations to the system (Eek; 2019, Section 5.5.6).

To overcome this issue, and to obtain faster convergence towards the desired path, a novel approach for path following of the barycenter within the NSB framework utilizing ideas inspired from traditional LOS methods is presented in this section. To the author's knowledge, such an attempt to combine the field of LOS and NSB is unique in the literature of formation control for marine surface vessels.

The LOS method presented here is inspired by the recent results on the curved path following in the presence of unknown ocean currents by Belleter et al. (2019). The same underlying ideas of Belleter et al. (2019) has been used in designing a LOS method for the barycenter.

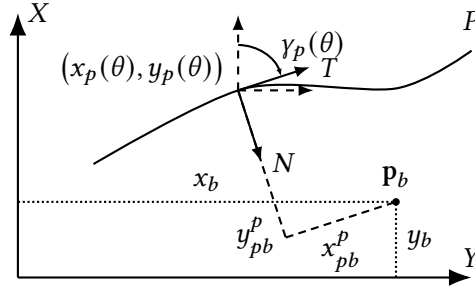


Figure 4.3: Definition of the path and path following errors.

However, as the relative velocities of the vessels are not available for feedback in the application considered here in this thesis, the following method is expressed in terms of the absolute velocities instead of relative velocities, which are commonly used when expressing LOS methods with unknown ocean currents Caharija et al. (2012); Wiig et al. (2018); Belleter et al. (2019). One direct implication of this is that the ocean current observed used to estimate the inertia frame ocean current components in Belleter et al. (2019) is superfluous, and it is not present in the following model.

4.4.3.1 Problem definition

The objective of the LOS guidance law presented in this section is to make the barycenter of the two vessels converge and follow a given smooth path P and maintain a desired total speed $U = \sqrt{u^2 + v^2}$ tangential to the path in the presence of unknown constant irrotational ocean currents. The path P is parametrized using a path variable $\theta \in \mathbb{R}$ with respect to the inertia frame. Moreover, for each point on the path $(x_p(\theta), y_p(\theta)) \in P$ a path tangential frame is introduced, see Fig. 4.3. Using these definitions, the path following errors $\mathbf{p}_{pb}^p \triangleq \begin{bmatrix} x_{pb}^p & y_{pb}^p \end{bmatrix}^T$ expressed in the path-tangential frame is found to be

$$\begin{bmatrix} x_{pb}^p \\ y_{pb}^p \end{bmatrix} = \begin{bmatrix} \cos(\gamma_p(\theta)) & -\sin(\gamma_p(\theta)) \\ \sin(\gamma_p(\theta)) & \cos(\gamma_p(\theta)) \end{bmatrix}^T \begin{bmatrix} x_b - x_p(\theta) \\ y_b - y_p(\theta) \end{bmatrix}, \quad (4.25)$$

where $\gamma_p(\theta)$ is the path-tangential angle. Hence, the task errors x_{pb}^p and y_{pb}^p expresses the position of the barycenter along the path frame tangential and orthogonal axis respectively. The path following objective for the barycenter is thus fulfilled if the trajectory of both vessels makes x_{pb}^p and y_{pb}^p converge to zero.

4.4.3.2 Barycenter kinematics

The barycenter given the two vessel positions can be expressed as

$$\mathbf{p}_b = \frac{1}{2} (\mathbf{p}_1 + \mathbf{p}_2) \in \mathbb{R}^2, \quad (4.26)$$

where \mathbf{p}_i is the position of the i^{th} vessel. Next, as the position of the barycenter cannot be controlled directly, only through each of the vessels, it is desirable to express the barycenter kinematics in terms of the kinematics of each vessel (2.1a). Taking the time derivative of (4.26) yields

$$\dot{\mathbf{p}}_b = \frac{1}{2} (\dot{\mathbf{p}}_1 + \dot{\mathbf{p}}_2), \quad (4.27)$$

or in component form

$$\dot{x}_b = \frac{1}{2} \left[u_1 \cos \psi_1 - v_1 \sin \psi_1 + u_2 \cos \psi_2 - v_2 \sin \psi_2 \right] \quad (4.28a)$$

$$\dot{y}_b = \frac{1}{2} \left[u_1 \sin \psi_1 + v_1 \cos \psi_1 + u_2 \sin \psi_2 + v_2 \cos \psi_2 \right]. \quad (4.28b)$$

To see how the kinematics of the barycenter affects the path following error dynamics, (4.25) is first written in component form

$$x_{pb}^p = (x_b - x_p) \cos(\gamma_p) + (y_b - y_p) \sin(\gamma_p) \quad (4.29a)$$

$$y_{pb}^p = -(x_b - x_p) \sin(\gamma_p) + (y_b - y_p) \cos(\gamma_p). \quad (4.29b)$$

The path following error dynamics of (4.29) is computed by inserting (4.28) into the derivative of (4.29), which after some rearrangements and trigonometric identities, see Section B.1 for details, are found to be

$$\dot{x}_{pb}^p = \frac{1}{2} U_1 \cos(\chi_1 - \gamma_p) + \frac{1}{2} U_2 \cos(\chi_2 - \gamma_p) - \dot{\theta} (1 - \kappa(\theta)) y_{pb}^p \quad (4.30a)$$

$$\dot{y}_{pb}^p = \frac{1}{2} U_1 \sin(\chi_1 - \gamma_p) + \frac{1}{2} U_2 \sin(\chi_2 - \gamma_p) - \kappa(\theta) \dot{\theta} x_{pb}^p, \quad (4.30b)$$

where $\kappa(\theta)$ is the curvature of P at θ and χ_i the course of vessel i .

4.4.3.3 Path parametrization

As the path is parametrized with the path variable θ , it is possible to use the update law of the path variable as an extra degree of freedom when designing the controller

Lapierre and Soetanto (2007). In Belleter et al. (2019) the update law is chosen to obtain a desirable behavior of the x_{pb}^p dynamics. Inspired by Belleter et al. (2019), a similar approach will be used here where the update law is chosen such that the propagation speed of the path tangential frame cancel the undesirable terms of (4.30a). To obtain the desired x_{pb}^p dynamics, the update law is chosen as

$$\dot{\theta} = \frac{1}{2}U_1 \cos(\chi_1 - \gamma_p) + \frac{1}{2}U_2 \cos(\chi_2 - \gamma_p) + k_\theta f_\theta(x_{pb}^p, y_{pb}^p), \quad (4.31)$$

where $k_\theta \in \mathbb{R}_{>0}$ and $f_\theta: \mathbb{R}^2 \rightarrow \mathbb{R}_{>0}$ is a control gain and function for convergence of x_{pb}^p . Similarly to Belleter et al. (2019) it will be used to ensure a desirable along-track error dynamics, and is chosen as

$$f_\theta(x_{pb}^p, y_{pb}^p) = \frac{x_{pb}^p}{\sqrt{1 + (x_{pb}^p)^2}}. \quad (4.32)$$

Inserting (4.31) into (4.30a) the following error dynamics is obtained

$$\dot{x}_{pb}^p = -k_\theta \frac{x_{pb}^p}{\sqrt{1 + (x_{pb}^p)^2}} + \dot{\theta} \kappa(\theta) y_{pb}^p. \quad (4.33)$$

4.4.3.4 Guidance law

As mentioned earlier, the position of the barycenter can only be controller through each of the vessels. Thus, the chosen guidance law for path following of the barycenter must be specified in terms of desired heading and surge references, which are the available control inputs, for each vessel. By calculating the Jacobian of (4.26), (4.27) can be inverted to find the mapping from the velocity of the barycenter to each of the vessels

$$\mathbf{J}_b = \frac{1}{2} \begin{bmatrix} 1 & 0 & 1 & 0 \\ 0 & 1 & 0 & 1 \end{bmatrix}. \quad (4.34)$$

Consequently, by taking the inverse mapping of $\mathbf{v}_b = \mathbf{J}_b [\mathbf{v}_1 \ \mathbf{v}_2]^T$, it is easily verified that the following relationship holds

$$\mathbf{v}_1 = \mathbf{v}_2 = \mathbf{v}_b. \quad (4.35)$$

Furthermore, given a desired along-path speed U_d and a desired course of the barycenter from the guidance law, the corresponding desired barycenter velocity is given by

$$\mathbf{v}_{b,d} = \begin{bmatrix} U_d \cos \chi_{b,d} \\ U_d \sin \chi_{b,d} \end{bmatrix}. \quad (4.36)$$

To make the barycenter converge to the desired path, a LOS guidance law on the form

$$\chi_{b,d} = \gamma_p(\theta) - \arctan\left(\frac{y_{pb}^p}{\Delta(\mathbf{p}_{pb}^p)}\right) \quad (4.37)$$

is chosen. The guidance law consists of two terms. The first term is the path tangential angle, while the second term is the velocity-path relative angle which is used to steer the barycenter such that its velocity is directed towards a point that is located a lookahead distance $\Delta(\mathbf{p}_{pb}^p)$ ahead of the path tangential frame \mathbf{p}_p . Inspired by Belleter et al. (2019), the lookahead distance has one constant part, and one part which depends on the path following errors given by

$$\Delta(\mathbf{p}_{pb}^p) = \sqrt{\mu + (x_{pb}^p)^2 + (y_{pb}^p)^2}, \quad (4.38)$$

where $\mu \in \mathbb{R}_{>0}$ is a constant. Choosing Δ to depend on x_{pb}^p is necessary to be able to find a bounded value of μ to prove boundedness of the sway dynamics v in Section A.2. Interestingly, due to the fact that absolute velocities are used, instead of relative, Δ could be chosen independent of y_{pb}^p as shown in Section A.2.1. However, it is still chosen to let Δ depend on y_{pb}^p to ensure a smoother convergence.

The implications of this time-varying lookahead distance are that when the barycenter is far away from the path, the lookahead distance will be large, ensuring a smooth convergence. When the barycenter is closer to the path, the lookahead distance decreases, allowing more rapid convergence. Overall, this leads to a smoother transient phase of the barycenter task dynamics. An illustration of the proposed guidance law can be seen in Fig. 4.4.

To generate the desired heading reference for each vessel, crab angle compensation according to (4.15b) is performed to obtain the following heading guidance law

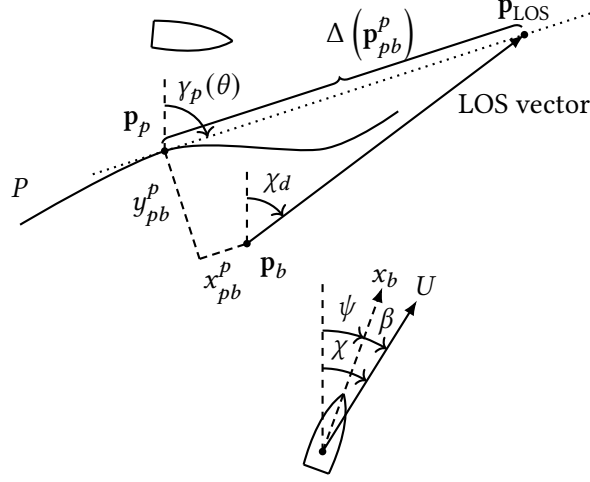


Figure 4.4: Illustration of the LOS guidance law for path following for the barycenter. The subscripts for the lower vessel's states are omitted for simplicity.

for each vessel, omitting the subscript indexes for simplicity

$$\psi_d = \underbrace{\gamma_p(\theta) - \arctan\left(\frac{v^b}{u_d}\right)}_{\beta_d} - \arctan\left(\frac{y_{pb}^p}{\Delta(\mathbf{p}_{pb}^p)}\right). \quad (4.39)$$

Substituting (4.39) in (4.30b) the following cross-track error dynamics are obtained, see Section B.2 for details

$$\begin{aligned} \dot{y}_{pb}^p &= \frac{1}{2}U_{d,1} \sin(\psi_{d,1} + \tilde{\psi}_1 + \beta_{d,1} - \gamma_p) \\ &\quad + \frac{1}{2}U_{d,2} \sin(\psi_{d,2} + \tilde{\psi}_2 + \beta_{d,2} - \gamma_p) \\ &\quad - \kappa(\theta)\dot{\theta}x_{pb}^p \\ &\quad + \frac{1}{2}\tilde{u}_1 \sin(\psi_1 - \gamma_p) + \frac{1}{2}\tilde{u}_2 \sin(\psi_2 - \gamma_p) \\ &= -\frac{1}{2}(U_{d,1} + U_{d,2}) \frac{y_{pb}^p}{\sqrt{\Delta^2 + (y_{pb}^p)^2}} \\ &\quad - \kappa(\theta)\dot{\theta}x_{pb}^p + G_1(\tilde{\psi}_1, \tilde{u}_1, \psi_{d,1}, U_{d,1}, \tilde{\psi}_2, \tilde{u}_2, \psi_{d,2}, U_{d,2}, y_{pb}^p), \end{aligned} \quad (4.40)$$

$$(4.41)$$

where $U_{d,i} = \sqrt{u_{d,i}^2 + v_i^2}$ being the total desired speed of vessel i and $G_1(\cdot)$ a perturbing

term of the error states of the vessels' autopilots, given by

$$G_1(\cdot) = \frac{1}{2}G_2\left(\tilde{\psi}_1, \tilde{u}_1, \psi_{d,1}, U_{d,1}, y_{pb}^p\right) + \frac{1}{2}G_2\left(\tilde{\psi}_2, \tilde{u}_2, \psi_{d,2}, U_{d,2}, y_{pb}^p\right) \quad (4.42)$$

with

$$\begin{aligned} G_2(\tilde{\psi}, \tilde{u}, \psi_d, U_d, y_{pb}^p) &= U_d \left(1 - \cos \tilde{\psi}\right) \sin\left(\arctan\left(\frac{y_{pb}^p}{\Delta}\right)\right) + \tilde{u} \sin(\psi - \gamma_p) \\ &+ U_d \cos\left(\arctan\left(\frac{y_{pb}^p}{\Delta}\right)\right) \sin \tilde{\psi}. \end{aligned} \quad (4.43)$$

Note that $G_1(\cdot)$ satisfy

$$G_1\left(0, 0, \psi_{d,1}, U_{d,1}, 0, 0, \psi_{d,2}, U_{d,2}, y_{pb}^p\right) = 0 \quad (4.44a)$$

$$\|G_1\left(\tilde{\psi}_1, \tilde{u}_1, \psi_{d,1}, U_{d,1}, \tilde{\psi}_2, \tilde{u}_2, \psi_{d,2}, U_{d,2}, y_{pb}^p\right)\| \leq \zeta_1(U_{d,1}, U_{d,2}) \|\tilde{\psi}_1 \ \tilde{u}_1 \ \tilde{\psi}_2 \ \tilde{u}_2\|^T \quad (4.44b)$$

where $\zeta_1(U_{d,1}, U_{d,2}) > 0$. This shows that the perturbing term $G_1(\cdot)$ is zero when the perturbing states are zero, and has at most linear growth in the perturbing states.

Proposition 4.2. *Consider a θ -parametrized path denoted by $P(\theta) = (x_p(\theta), y_p(\theta))$, with the update law (4.31) and a system given by two vessels with the barycenter kinematics (4.28). Furthermore, assume that each vessel follows the references of the guidance law (4.39) perfectly, i.e. $\tilde{\psi} = \tilde{u} = 0$. Then, the origin of (4.33), (4.41) is a uniformly semi-global exponential stable (USGES) equilibrium point.*

Proof. This proof makes use of recent results for Lyapunov sufficient conditions for USGES systems in Pettersen (2017) to prove USGES for Proposition 4.2.

Using the fact that $\tilde{\psi} = \tilde{u} = 0$ and (4.44a), the cross-track error dynamics (4.41) simplifies to

$$\dot{y}_{pb}^p = -\frac{1}{2}(U_{d,1} + U_{d,2}) \frac{y_{pb}^p}{\sqrt{\Delta^2 + (y_{pb}^p)^2}} - \kappa(\theta)\dot{\theta}x_{pb}^p. \quad (4.45)$$

Next, consider the C^1 Lyapunov Function Candidate $V_{pb}^p = \frac{1}{2}(x_{pb}^p)^2 + \frac{1}{2}(y_{pb}^p)^2$. Taking the derivatives along the trajectories of (4.33) and (4.45)

$$\dot{V}_{pb}^p = x_{pb}^p \dot{x}_{pb}^p + y_{pb}^p \dot{y}_{pb}^p \quad (4.46)$$

$$\begin{aligned}
&= x_{pb}^p \left(-k_\theta \frac{x_{pb}^p}{\sqrt{1 + (x_{pb}^p)^2}} + \dot{\theta} \kappa(\theta) y_{pb}^p \right) \\
&\quad + y_{pb}^p \left(-\frac{1}{2} (U_{d,1} + U_{d,2}) \frac{y_{pb}^p}{\sqrt{\Delta^2 + (y_{pb}^p)^2}} - \kappa(\theta) \dot{\theta} x_{pb}^p \right) \quad (4.47)
\end{aligned}$$

$$= -k_\theta \frac{(x_{pb}^p)^2}{\sqrt{1 + (x_{pb}^p)^2}} - \frac{1}{2} (U_{d,1} + U_{d,2}) \frac{(y_{pb}^p)^2}{\sqrt{\Delta^2 + (y_{pb}^p)^2}} \quad (4.48)$$

which is negative definite, meaning UGAS can be concluded. Furthermore, to investigate USGES, define the error variables

$$\mathbf{e} = \begin{bmatrix} e_1 \\ e_2 \end{bmatrix} = \begin{bmatrix} x_{pb}^p \\ y_{pb}^p \end{bmatrix}. \quad (4.49)$$

By substituting the lookahead distance (4.38) and the error variables (4.49), the LFC derivative (4.48) can be written as

$$\dot{V} = -k_\theta \frac{e_1^2}{\sqrt{1 + e_1^2}} - \frac{1}{2} (U_{d,1} + U_{d,2}) \frac{e_2^2}{\sqrt{\mu + e_1^2 + 2e_2^2}} \quad (4.50)$$

$$= -\mathbf{e}^T \mathbf{Q} \mathbf{e} \quad (4.51)$$

for which

$$\mathbf{Q} = \begin{bmatrix} \frac{k_\theta}{\sqrt{1+e_1^2}} & 0 \\ 0 & \frac{1}{2} \frac{U_{d,1}+U_{d,2}}{\sqrt{\mu+e_1^2+2e_2^2}} \end{bmatrix} > 0 \quad (4.52)$$

is a positive definite matrix as $k_\theta, U_{d,1}, U_{d,2} > 0$. Hence, the following bound holds $\forall \mathbf{e} \in \mathcal{B}_r$,

$$\dot{V} \leq -q_{\min} \|\mathbf{e}\|^2, \quad (4.53)$$

with

$$q_{\min} \triangleq \lambda_{\min} \left(\begin{bmatrix} \frac{k_\theta}{\sqrt{1+r^2}} & 0 \\ 0 & \frac{1}{2} \frac{U_{d,1}+U_{d,2}}{\sqrt{\mu+3r^2}} \end{bmatrix} \right) \quad (4.54)$$

for any ball $\mathcal{B}_r \triangleq \{\max\{|e_1|, |e_2|\} < r\}$, $r > 0$, where $\lambda_{\min}(\mathbf{A})$, is defined as the

minimum eigenvalue of A . Thus, the conditions for (Pettersen; 2017, Theorem 5) is fulfilled with $k_1 = k_2 = \frac{1}{2}$, $a = 2$ and $k_3 = q_{\min}$, and USGES can be concluded for the origin (4.33), (4.41) under the conditions given in Proposition 4.2. \square

It can be observed that it is not possible to conclude GES for the origin (4.33), (4.41) using (Khalil; 2002, Theorem 4.10) as it is not possible to find a positive constant k_3 that is independent of the size of the estimated region of attraction as k_3 converges to zero when the distance to the path increases Pettersen (2017).

In fact, USGES is the best possible stability guaranties possible for LOS methods due to the saturation in (4.39), see Fossen and Pettersen (2014).

4.4.4 Stability of merged formation and barycenter tasks

While the previous sections have focused on the stability properties of each task individually, it is of interest to investigate what stability guarantees may be concluded when the solutions for the formation and barycenter tasks are combined in the NSB framework. As discussed in Section 4.2.1, components from lower-priority tasks that would conflict higher-priority tasks are removed through the null-space projection (4.12). Thus, it cannot be guaranteed that the lower-priority task errors will converge to zero from the stability analysis of each task separately. For the tasks previously defined, only the formation and barycenter tasks will be active during normal operation. Thus, the following analysis will focus on the stability properties when these two tasks are active.

A rigorously analysis of the stability properties when combining task solutions using the projection method (4.12) is performed in Arrichiello (2006); Antonelli et al. (2008) where it was proven that the resulting system of three tasks would be UGAS if an orthogonality condition existed between two successive tasks while an independency condition existed between the remaining tasks. In Antonelli et al. (2008), two tasks are defined as orthogonal if

$$\mathbf{J}_x \mathbf{J}_y^\dagger = \mathbf{O}_{m_x \times m_y}, \quad (4.55)$$

where $\mathbf{O}_{m_x \times m_y}$ is the $(m_x \times m_y)$ null matrix, and two tasks are defined as independent if

$$\rho(\mathbf{J}_x^T) + \rho(\mathbf{J}_y^T) = \rho([\mathbf{J}_x^T \ \mathbf{J}_y^T]), \quad (4.56)$$

where $\rho(\cdot)$ denotes the rank of the matrix.

Proposition 4.3. *Consider the formation and barycenter tasks defined according to Section 4.4.2 and Section 4.4.3 respectively, combined with the null-space-projection (4.12). Furthermore, assume that the system velocities perfectly follow the reference \mathbf{v}_a . Then, this two-task system is UGAS, and both tasks' errors converge to zero asymptotically.*

Proof. For a two-task system to be asymptotically stable, the two tasks must be orthogonal according to Antonelli et al. (2008). Using the two task Jacobians (4.23) and (4.34), it is straight forward to verify that they satisfy the orthonogality condition as

$$\mathbf{J}_f \mathbf{J}_b^\dagger = \mathbf{O}_{2 \times 2}. \quad (4.57)$$

Consequently, both the task's errors are asymptotically stable, and the system is UGAS, a result also shown in Antonelli et al. (2008). \square

4.5 Closed-loop analysis

In this section, the closed-loop stability of the guidance laws presented in the last section is analyzed. While Proposition 4.1 and Proposition 4.2 proved stability for both the formation and barycenter tasks respectively, assuming perfect tracking of the desired surge and heading references, they did not account for the dynamics of each vessel. It is well known that inadequate tracking by the inner-loop controllers may destabilize the overall system. Consequently, further analysis is required to prove overall closed-loop stability when also incorporating the vessel dynamics, meaning the desired references are not necessarily tracked perfectly at all times. Due to the vessel model's parameter uncertainties and the complexity of the waterjet model in Chapter 2, the selected autopilots in Section 2.4 operate directly on the desired throttle and steering demands respectively. An implication of this is that more advanced techniques such as feedback-linearization are not possible, making it challenging to prove stability with these maneuvering controllers.

Instead, the following stability analysis will be performed under the ideal case where all model parameters are assumed to be perfectly known. Hence, techniques such as feedback-linearization may be used in the surge and heading autopilots to cancel out undesirable nonlinear model dynamics, which are crucial for proving stability. More specifically, in the following analysis, it will be assumed that the vessel dynamics, and autopilots, may be described by the vessel model and autopilots in Moe et al. (2016). The assumptions for when this holds are given in Moe et al. (2016); Børhaug et al. (2008), and repeated here: Assumption 2.1 and Assumptions 4.1–4.4 for convenience.

Assumption 4.1 ((Moe et al.; 2016, Assumption 1)). *The motion of the USV is described in 3-DOF, that is surge, sway, and yaw.*

Assumption 4.2 ((Moe et al.; 2016, Assumption 2)). *The USV is port-starboard symmetric.*

Assumption 4.3 ((Moe et al.; 2016, Assumption 3)). *The body-fixed coordinate system is located at a distance $(x_g^*, 0)$ from the USV's CG along the center-line of the vessel such that the yaw control does not affect the sway motion. Such a transformation does always exist for port-starboard symmetric vessels Fredriksen and Pettersen (2006).*

Assumption 4.4 ((Børhaug et al.; 2008, Assumption A.4)). *The function $Y(u, u_c)$ satisfies*

$$Y(u, u_c) \leq -Y_{min} < 0, \quad \forall u \in [0, U_d]. \quad (4.58)$$

Given these assumptions, the full model of each vessel, in component form, from Moe et al. (2016) may be written as

$$\dot{x} = \cos(\psi)u - \sin(\psi)v \quad (4.59a)$$

$$\dot{y} = \sin(\psi)u + \cos(\psi)v \quad (4.59b)$$

$$\dot{\psi} = r \quad (4.59c)$$

$$\dot{u} = -\frac{d_{11} + d_{11}^q}{m_{11}}u + \frac{(m_{22}v + m_{23}r)}{m_{11}}r + \phi_u^T(\psi, r)\theta_u + \tau_u \quad (4.59d)$$

$$\dot{v} = X(u, u_c)r + Y(u, u_c)v_r \quad (4.59e)$$

$$\dot{r} = F_r(u, v, r) + \phi_r^T(u, v, r, \psi)\theta_r + \tau_r \quad (4.59f)$$

where $\theta_u = \theta_r = [V_x \ V_y \ V_x^2 \ V_y^2 \ V_x V_y]^T$ and the expressions for $\phi_u^T(\psi, r)$, $X(u, u_c)$, $Y(u, u_c)$, $F_r(u, v, r)$ and $\phi_r^T(u, v, r, \psi)$ are given in Appendix C. It should be noted that in Moe et al. (2016), the expressions for the sway dynamics are expressed as $X(u_r, u_c)$ and $Y(u_r)$, i.e. with relative velocities. However, to simplify the stability analyses later, the expressions have been reformulated in terms of absolute velocities here.

Next, the autopilots for heading and surge from Moe et al. (2016) are presented. Defining the error states

$$\tilde{u} = u - u_d \quad (4.60a)$$

$$\tilde{\psi} = \psi - \psi_d \quad (4.60b)$$

$$\dot{\tilde{\psi}} = \dot{\psi} - \dot{\psi}_d \quad (4.60c)$$

$$\xi = [\tilde{u} \ \tilde{\psi} \ \dot{\tilde{\psi}}]^T \quad (4.60d)$$

the following adaptive feedback linearizing PD-controller with sliding-mode is used to ensure tracking of the desired heading

$$\begin{aligned} \tau_r = & -F_r(u, v, r) - \phi_r^T(u, v, r, \psi) \hat{\theta}_r + \ddot{\psi}_d \\ & - (k_\psi + \lambda k_r) \tilde{\psi} - (k_r + \lambda) \dot{\tilde{\psi}} - k_d \text{sign}(\dot{\tilde{\psi}} + \lambda \tilde{\psi}) \end{aligned} \quad (4.61a)$$

$$\dot{\hat{\theta}}_r = \gamma_r \phi_r^T(u, v, r, \psi) (\dot{\tilde{\psi}} + \lambda \tilde{\psi}), \quad (4.61b)$$

where the gains $k_\psi, k_r, \lambda, \gamma_r$ are constant and positive and the function $\text{sign}(x)$ returns 1, 0 and -1 when x is positive, zero and negative respectively. Further, a combined feedback linearizing and sliding-mode P-controller is used to track the desired surge speed

$$\begin{aligned} \tau_u = & -\frac{1}{m_{11}} (m_{22}v + m_{23}r) r + \frac{d_{11}}{m_{11}} u_d - \phi_u^T(\psi, r) \hat{\theta}_u \\ & + \frac{d_{11}^q}{m_{11}} u^2 + \dot{u}_d - k_u \tilde{u} - k_e \text{sign}(\tilde{u}) \end{aligned} \quad (4.62a)$$

$$\dot{\hat{\theta}}_u = \gamma_u \phi_u^T(\psi, r) \tilde{u}. \quad (4.62b)$$

Proposition 4.4 ((Moe et al.; 2016, Proposition 1)). *Given an underactuated surface vessel described by the vessel model (4.59). Under Assumption 2.1 and Assumptions 4.1–4.4, the adaptive controllers (4.61) and (4.62) ensures that $\xi = 0$ is an UGES equilibrium point and that the references provided by the guidance system is exponentially tracked.*

Proof. The proof can be found in Moe et al. (2016). \square

During the following stability analyses, the closed-loop system will be seen as a cascade, where the marine vessel and the autopilots, tracking the guidance references, are the inner-loop, while the guidance system, each of the NSB tasks, constitute the outer-loop, according to Fig. 4.1. Consequently, the error states (4.60) may be seen as perturbations to the nominal dynamics of the guidance method, i.e. the error dynamics considered in Proposition 4.1 and Proposition 4.2, where the autopilots perfectly follow the guidance references. Cascaded theory may therefore be used to prove the overall stability of the cascaded system.

4.5.1 Formation task

When considering stability analysis of the CLIK control law within the NSB framework, a common strategy is to ignore the system dynamics of each vehicle, and

assume that the vehicles follow the NSB references perfectly, see e.g., Antonelli et al. (2008); Arrichiello (2006). In this section, the stability analysis will be extended by investigating the stability of the overall closed-loop system by incorporating the vessel dynamics (4.59) and adaptive controllers (4.61) and (4.62) into the analysis.

The expression for the closed-loop system is obtained by inserting the CLIK control law (4.5) into the differential relationship (4.3)

$$\dot{\tilde{\sigma}}_f = -\Lambda \tilde{\sigma}_f - \mathbf{J}_f \tilde{\mathbf{v}}. \quad (4.63)$$

Here, the first term denotes the nominal dynamics of the task error, while the last term is an perturbing term caused from imperfect tracking of the NSB references due to system dynamics. To express the perturbing term as a function of the error states of the autopilots (4.60), the velocity vector is decomposed into surge, sway and heading components. After some rearrangements and trigonometric relations, the following closed-loop system is obtained, see Section B.3 for details

$$\dot{\tilde{\sigma}}_f = -\Lambda \tilde{\sigma}_f - \mathbf{J}_f \begin{bmatrix} G_3 \left(\tilde{\psi}_1, \tilde{u}_1, \psi_{d,1}, U_{d,1}, \beta_{d,1} \right) \\ G_4 \left(\tilde{\psi}_1, \tilde{u}_1, \psi_{d,1}, U_{d,1}, \beta_{d,1} \right) \\ G_3 \left(\tilde{\psi}_2, \tilde{u}_2, \psi_{d,2}, U_{d,2}, \beta_{d,2} \right) \\ G_4 \left(\tilde{\psi}_2, \tilde{u}_2, \psi_{d,2}, U_{d,2}, \beta_{d,2} \right) \end{bmatrix} \quad (4.64)$$

with $G_{3,4}(\cdot)$ a perturbing term of the error states of the vessel's autopilots, given by

$$\begin{aligned} G_3 \left(\tilde{\psi}, \tilde{u}, \psi_d, U_d, \beta_d \right) &= \tilde{u} \cos \psi_d \cos \tilde{\psi} - \tilde{u} \sin \psi_d \sin \tilde{\psi} \\ &\quad + U_d \cos (\psi_d + \beta_d) \left(1 - \cos \tilde{\psi} \right) \\ &\quad - U_d \sin (\psi_d + \beta_d) \sin \tilde{\psi} \end{aligned} \quad (4.65)$$

$$\begin{aligned} G_4 \left(\tilde{\psi}, \tilde{u}, \psi_d, U_d, \beta_d \right) &= \tilde{u} \sin \psi_d \cos \tilde{\psi} + \tilde{u} \cos \psi_d \sin \tilde{\psi} \\ &\quad - U_d \sin (\psi_d + \beta_d) \left(1 - \cos \tilde{\psi} \right) \\ &\quad - U_d \cos (\psi_d + \beta_d) \sin \tilde{\psi}. \end{aligned} \quad (4.66)$$

Note that both $G_{3,4}(\cdot)$ satisfy

$$G_{3,4} (0, 0, \psi_d, U_d, \beta_d) = 0 \quad (4.67a)$$

$$\|G_{3,4} \left(\tilde{\psi}, \tilde{u}, \psi_d, U_d, \beta_d \right)\| \leq \zeta_{3,4} (U_d) \|[\tilde{\psi} \ \tilde{u}]^T\| \quad (4.67b)$$

where $\zeta_{3,4}(U_d) > 0$. This shows that the perturbing term $G_{3,4}(\cdot)$ is zero when the perturbing states are zero, and has at most linear growth in the perturbing states.

Next, define the following sets of variables

$$\tilde{\mathbf{X}}_1 \triangleq [\tilde{\sigma}_{f,x} \ \tilde{\sigma}_{f,y}]^T \quad (4.68a)$$

$$\tilde{\mathbf{X}}_{2,i} \triangleq [\tilde{u}_i \ \dot{\tilde{\psi}}_i \ s_i]^T \quad (4.68b)$$

$$\tilde{\mathbf{X}}_2 \triangleq [\tilde{\mathbf{X}}_{2,1}^T \ \tilde{\mathbf{X}}_{2,2}^T]^T, \quad (4.68c)$$

where $\tilde{\mathbf{X}}_{2,i}$, contains the autopilot error states of each vessel, that converge independent of $\tilde{\mathbf{X}}_1$, and s_i is defined in Moe et al. (2016) as $s_i = \dot{\tilde{\psi}}_i + \lambda_i \tilde{\psi}_i$. The closed-loop error dynamics of the total system may then be written as

$$\dot{\tilde{\mathbf{X}}}_1 = -\Lambda \tilde{\sigma}_f - \mathbf{J}_f \begin{bmatrix} G_3(\tilde{\psi}_1, \tilde{u}_1, \psi_{d,1}, U_{d,1}, \beta_{d,1}) \\ G_4(\tilde{\psi}_1, \tilde{u}_1, \psi_{d,1}, U_{d,1}, \beta_{d,1}) \\ G_3(\tilde{\psi}_2, \tilde{u}_2, \psi_{d,2}, U_{d,2}, \beta_{d,2}) \\ G_4(\tilde{\psi}_2, \tilde{u}_2, \psi_{d,2}, U_{d,2}, \beta_{d,2}) \end{bmatrix} \quad (4.69a)$$

$$\dot{\tilde{\mathbf{X}}}_{2,i} = \begin{bmatrix} -\left(\frac{d_{11}}{m_{11}} + k_{u,i}\right) \tilde{u}_i - \boldsymbol{\phi}_u^T(\cdot) \tilde{\boldsymbol{\theta}}_{u,i} - k_{e,i} \text{sign}(\tilde{u}_i) \\ -\lambda_i \tilde{\psi}_i + s \\ -k_{\psi,i} \tilde{\psi}_i - k_{r,i} s_i - \boldsymbol{\phi}_r^T(\cdot) \tilde{\boldsymbol{\theta}}_{r,i} - k_{d,i} \text{sign}(s_i) \end{bmatrix} \quad (4.69b)$$

$$\dot{\tilde{\boldsymbol{\theta}}}_{r,i} = \gamma_r \boldsymbol{\phi}_r^T(u, v, r, \psi) s_i \quad (4.69c)$$

$$\dot{\tilde{\boldsymbol{\theta}}}_{u,i} = \gamma_u \boldsymbol{\phi}_u^T(\psi, r) \tilde{u}_i \quad (4.69d)$$

$$\begin{aligned} \dot{v}_i &= X(u_{d,i} + \tilde{u}_i, u_c) r_{d,i} + X(u_{d,i} + \tilde{u}_i, u_c) \tilde{r}_i \\ &\quad + Y(u_{d,i} + \tilde{u}_i, u_c) v - Y(u_{d,i} + \tilde{u}_i, u_c) v_c, \end{aligned} \quad (4.69e)$$

where Eqs. (4.69a)–(4.69b) should converge to zero, while Eqs. (4.69c)–(4.69e) should remain bounded.

Theorem 4.1. *Consider the formation task function (4.19) with the configuration-dependent task Jacobian (4.23) and a system given by two vessels, each described by (4.59). Furthermore, the adaptive controllers (4.61) and (4.62) are used as autopilots for each of the vessels, with the CLIK control law (4.5). Then, under the assumption that the sway-dynamics are bounded, the origin of the closed-loop system Eqs. (4.69a)–(4.69b) is an UGES equilibrium point while Eqs. (4.69c)–(4.69e) remains bounded.*

Proof. To prove UGES of the equilibrium point of the task function error dynamics,

results within cascaded systems from (Loría and Panteley; 2005, Theorem 2.1 and Proposition 2.3) will be used.

First, consider the nominal dynamics given by the first matrix of (4.69a). Selecting the C^1 Lyapunov function candidate

$$V(\tilde{\mathbf{X}}_1) = \frac{1}{2} \tilde{\boldsymbol{\sigma}}_f^T \tilde{\boldsymbol{\sigma}}_f = \frac{1}{2} \tilde{\sigma}_{f,x}^2 + \frac{1}{2} \tilde{\sigma}_{f,y}^2, \quad (4.70)$$

it is positive definite on \mathbb{R} and the nominal dynamics is proved UGES in Proposition 4.1, implying both UGAS and ULES. Hence, (Loría and Panteley; 2005, Assumption 1a) is trivially satisfied for the nominal system. The existence of positive constants $c_1, c_2, \eta > 0$ satisfying (Loría and Panteley; 2005, Assumption 3) is clearly satisfied with (4.70)

$$\begin{aligned} \left\| \frac{\partial V}{\partial \tilde{\mathbf{X}}_1} \right\| \|\tilde{\mathbf{X}}_1\| &= \left\| [\tilde{\sigma}_{f,x} \quad \tilde{\sigma}_{f,y}]^T \right\|^2 \\ &= \tilde{\sigma}_{f,x}^2 + \tilde{\sigma}_{f,y}^2 \\ &= 2V(\tilde{\mathbf{X}}_1) \quad \forall \|\tilde{\mathbf{X}}_1\| \end{aligned} \quad (4.71)$$

$$\left\| \frac{\partial V}{\partial \tilde{\mathbf{X}}_1} \right\| = \|\tilde{\mathbf{X}}_1\| \leq \eta \quad \forall \|\tilde{\mathbf{X}}_1\| \leq \eta, \quad (4.72)$$

i.e. with $c_1 = 2$ and $c_2 = \eta$ for any choice $\eta > 0$. As the perturbing system (4.69b) is UGES by Proposition 4.4 it is also UGAS.

Furthermore, the interconnection term, the second vector of (4.69a), satisfies the linear growth criteria from (Loría and Panteley; 2005, Assumption 4). More specifically, it does not grow with $\tilde{\mathbf{X}}_1$ as it can be bounded by linear functions of $\tilde{\mathbf{X}}_2$ from (4.67b).

Finally, the conditions of (Loría and Panteley; 2005, Assumption 5) must be investigated. Following the arguments from (Pettersen; 2017, Remark 11), the assumption is satisfied by the fact that (4.69b) is UGES, which implies both UGAS and ULES. In (Pettersen; 2017, Remark 11) it is shown that the properties UGAS + ULES fulfills (Loría and Panteley; 2005, Assumption 5). All conditions of (Loría and Panteley; 2005, Theorem 2.1) are therefore satisfied, and the origin of the closed-loop system $(\tilde{\mathbf{X}}_1, \tilde{\mathbf{X}}_2) = (\mathbf{0}, \mathbf{0})$ can be concluded UGAS. Additionally, since both subsystems; the perturbing system (4.69b) and the nominal system (4.69a), are UGES, the cascade Eqs. (4.69a)–(4.69b) is UGES by (Loría and Panteley; 2005, Proposition 2.3).

Thus, all that remains is to prove boundedness of Eqs. (4.69c)–(4.69d). Boundedness of Eqs. (4.69c)–(4.69d) is proven in the proof of Proposition 4.4 in Moe et al. (2016)

where it is established that the equilibrium points $(\tilde{\psi}, s, \dot{\tilde{\theta}}_r) = \mathbf{0}$ and $(\tilde{u}, \dot{\tilde{\theta}}_u) = \mathbf{0}$ are UGS, which implies that both $\tilde{\theta}_r$ and $\tilde{\theta}_u$ are bounded, which concludes the proof of Theorem 4.2. \square

4.5.2 Barycenter task

Proving the closed-loop stability for the barycenter task will be done by following in the lines of Belleter et al. (2019). First, forward completeness of the system states is established. Then, the boundedness of the sway dynamics is proven. Finally, the cascaded system's stability is established to be USGES, making use of the recent results for Lyapunov sufficient conditions in Pettersen (2017).

In order to prove the closed-loop system's stability and that the path following objective is achieved, it must be shown that the along-track and cross-track error dynamics converge to zero. Furthermore, the error states of the autopilot of each vessel respectively must also converge to zero simultaneously. Since the vessels are underactuated in the sway dynamics, convergence to zero of the sway dynamics can not be proven in the general case with curved paths. Instead, it must be shown that the sway dynamics are globally bounded to guarantee that the zero dynamics are well behaved and do not diverge.

First, the expression for the desired yaw rate dynamics is obtained by taking the derivative of (4.39)

$$r_d = \dot{\psi}_d = \kappa(\theta)\dot{\theta} - \frac{\dot{v}u_d - \dot{u}_dv}{u_d^2 + v^2} - \frac{1}{\Delta^2 + (y_{pb}^p)^2} \left[\Delta \dot{y}_{pb}^p - y_{pb}^p \left(\frac{\partial \Delta}{\partial x_{pb}^p} \dot{x}_{pb}^p + \frac{\partial \Delta}{\partial y_{pb}^p} \dot{y}_{pb}^p \right) \right] \quad (4.73)$$

$$= \kappa(\theta)\dot{\theta} - \frac{u_d}{u_d^2 + v^2} (X(u, u_c)r + Y(u, u_c)v - Y(u, u_c)v_c) + \frac{\dot{u}_dv}{u_d^2 + v^2} - \frac{1}{\Delta^2 + (y_{pb}^p)^2} \left[\left(\Delta - y_{pb}^p \frac{\partial \Delta}{\partial y_{pb}^p} \right) \left[-\frac{1}{2} (U_{d,1} + U_{d,2}) \frac{y_{pb}^p}{\sqrt{\Delta^2 + (y_{pb}^p)^2}} - \kappa(\theta)\dot{\theta} x_{pb}^p + G_1(\cdot) \right] - y_{pb}^p \frac{\partial \Delta}{\partial x_{pb}^p} \left[-k_\theta \frac{x_{pb}^p}{\sqrt{1 + (x_{pb}^p)^2}} + \dot{\theta} \kappa(\theta) y_{pb}^p \right] \right]. \quad (4.74)$$

Looking at (4.74) it is clear how the expression of $\dot{\psi}_d$ contains terms depending on \dot{v} which depends on the unknown ocean current u_c and the relative surge and sway speeds u_r and v_r respectively. Interestingly, contrary to Belleter et al. (2019) where $\dot{\psi}_d$ were also dependent on unknown variables and could not be realised, it is not an issue in (4.74). In Belleter et al. (2019), the terms depending on the unknown ocean currents appeared through the along- and cross-track error dynamics. As these states could not be measured directly, they had to be calculated, requiring knowledge about the unknown ocean current. However, in (4.74), the terms depending on the unknown variables appear through the sway dynamic \dot{v} of the vessel, which can be measured using e.g. an Inertial Measurement Unit (IMU), and is therefore available for feedback. This, apparently small difference, allows (4.74) to be realised by obtaining \dot{v} through sensor measurement instead of calculated using (4.59e), while $\dot{\psi}_d$ in (Belleter et al.; 2019, Eq. (35)) could not.

Next, the following sets of variables are defined

$$\tilde{\mathbf{X}}_1 \triangleq [y_{pb}^p \ x_{pb}^p]^T \quad (4.75a)$$

$$\tilde{\mathbf{X}}_{2,i} \triangleq [\tilde{u}_i \ \tilde{\psi}_i \ s_i]^T \quad (4.75b)$$

$$\tilde{\mathbf{X}}_2 \triangleq [\tilde{\mathbf{X}}_{2,1}^T \ \tilde{\mathbf{X}}_{2,2}^T]^T, \quad (4.75c)$$

where $\tilde{\mathbf{X}}_{2,i}$, containing the autopilot error states of each vessel, that converge independent of $\tilde{\mathbf{X}}_1$. Thus, the closed-loop error dynamics of the total system may be written as

$$\dot{\tilde{\mathbf{X}}}_1 = \begin{bmatrix} -\frac{1}{2} (U_{d,1} + U_{d,2}) \frac{y_{pb}^p}{\sqrt{\Delta^2 + (y_{pb}^p)^2}} - \kappa(\theta) \dot{\theta} x_{pb}^p \\ -k_\theta \frac{x_{pb}^p}{\sqrt{1 + (x_{pb}^p)^2}} + \dot{\theta} \kappa(\theta) y_{pb}^p \end{bmatrix} + \begin{bmatrix} G_1(\cdot) \\ 0 \end{bmatrix} \quad (4.76a)$$

$$\dot{\tilde{\mathbf{X}}}_{2,i} = \begin{bmatrix} -\left(\frac{d_{11}}{m_{11}} + k_{u,i}\right) \tilde{u}_i - \boldsymbol{\phi}_u^T(\cdot) \tilde{\boldsymbol{\theta}}_{u,i} - k_{e,i} \text{sign}(\tilde{u}_i) \\ -\lambda_i \tilde{\psi}_i + s \\ -k_{\psi,i} \tilde{\psi}_i - k_{r,i} s_i - \boldsymbol{\phi}_r^T(\cdot) \tilde{\boldsymbol{\theta}}_{r,i} - k_{d,i} \text{sign}(s_i) \end{bmatrix} \quad (4.76b)$$

$$\dot{\tilde{\boldsymbol{\theta}}}_{r,i} = \gamma_r \boldsymbol{\phi}_r^T(u, v, r, \psi) s_i \quad (4.76c)$$

$$\dot{\tilde{\boldsymbol{\theta}}}_{u,i} = \gamma_u \boldsymbol{\phi}_u^T(\psi, r) \tilde{u}_i \quad (4.76d)$$

$$\begin{aligned} \dot{v}_i &= X(u_{d,i} + \tilde{u}_i, u_c) r_{d,i} + X(u_{d,i} + \tilde{u}_i, u_c) \tilde{r}_i \\ &\quad + Y(u_{d,i} + \tilde{u}_i, u_c) v_i - Y(u_{d,i} + \tilde{u}_i, u_c) v_c, \end{aligned} \quad (4.76e)$$

where Eqs. (4.76a)–(4.76b) should converge to zero, while Eqs. (4.76c)–(4.76e) should remain bounded.

Lemma 4.2 (Forward Completeness). *The trajectories of the closed-loop system (4.76) are forward complete*

Proof. The proof of this lemma is given in Section A.1. □

Lemma 4.3 (Boundedness near $(\tilde{X}_1, \tilde{X}_2) = \mathbf{0}$). *The system (4.76e) is bounded near the manifold $(\tilde{X}_1, \tilde{X}_2) = \mathbf{0}$ if and only if the curvature of P satisfies the following condition:*

$$\kappa_{max} \triangleq \max_{\theta \in P} |\kappa(\theta)| < \frac{Y_{min}}{X_{max}}, \quad X_{max} \triangleq |X(u, u_c)|_{\infty}. \quad (4.77)$$

Proof. The proof of this lemma is given in Section A.2. □

Lemma 4.4 (Boundedness near $\tilde{X}_2 = \mathbf{0}$). *The system (4.76e) is bounded near the manifold $\tilde{X}_2 = \mathbf{0}$, independently of \tilde{X}_1 , if the conditions of Lemma 4.3 is satisfied, and the constant term of the lookahead distance is chosen accordingly to*

$$\mu > \frac{4X_{max}}{Y_{min} - X_{max}\kappa_{max}}, \quad (4.78)$$

where $X_{max} \triangleq |X(u, u_c)|_{\infty}$ and $\kappa_{max} \triangleq \max_{\theta \in P} |\kappa(\theta)|$.

Proof. The proof of this lemma is given in Section A.3. □

Theorem 4.2. *Consider a θ -parametrized path denoted by $P(\theta) = (x_p(\theta), y_p(\theta))$, with the update law (4.31) and a system given by two vessels, each described by (4.59), giving the barycenter kinematics (4.28). Furthermore, the adaptive controllers (4.61) and (4.62) are used as autopilots for each of the vessels, with the guidance law (4.39). Then, under the conditions of Lemmas 4.2–4.4, the barycenter follows the path P with Eqs. (4.76c)–(4.76e) bounded, and the origin of the closed-loop system Eqs. (4.76a)–(4.76b) is an USGES equilibrium point.*

Proof. First, consider the unactuated sway-dynamics by following the argument from (Belleter et al.; 2019, Proof of Theorem 1). From the fact that the origin of (4.76b) is USGES, that the closed-loop system (4.76) is forward complete, and that the sway-dynamics (4.76e) is bounded near the manifold $\tilde{X}_2 = \mathbf{0}$, the existence of a finite time $T > t_0$ such that the solutions of (4.76b) will be sufficiently close to $\tilde{X}_2 = \mathbf{0}$ to guarantee boundedness of v_i can be concluded.

Next, consider the nominal dynamics given by the first matrix of (4.76a). Selecting the C^1 Lyapunov function candidate

$$V(\tilde{\mathbf{X}}_1) = \frac{1}{2} (x_{pb}^p)^2 + \frac{1}{2} (y_{pb}^p)^2, \quad (4.79)$$

it is positive definite on \mathbb{R} , and the nominal dynamics is proven UGAS and to satisfy the conditions of (Pettersen; 2017, Theorem 5) in Proposition 4.2. The existence of positive constants $c_1, c_2, \eta > 0$ satisfying (Pettersen; 2017, Assumption 1) is clearly satisfied with (4.79)

$$\begin{aligned} \left\| \frac{\partial V}{\partial \tilde{\mathbf{X}}_1} \right\| \|\tilde{\mathbf{X}}_1\| &= \left\| [y_{pb}^p \ x_{pb}^p]^T \right\|^2 \\ &= (x_{pb}^p)^2 + (y_{pb}^p)^2 \\ &= 2V(\tilde{\mathbf{X}}_1) \quad \forall \|\tilde{\mathbf{X}}_1\| \end{aligned} \quad (4.80)$$

$$\left\| \frac{\partial V}{\partial \tilde{\mathbf{X}}_1} \right\| = \|\tilde{\mathbf{X}}_1\| \leq \eta \quad \forall \|\tilde{\mathbf{X}}_1\| \leq \eta, \quad (4.81)$$

i.e. with $c_1 = 2$ and $c_2 = \eta$ for any choice $\eta > 0$. Next, the perturbing system (4.76b) is UGES by Proposition 4.4 which implies both UGAS and USGES. Hence, the perturbing system also satisfies the conditions of (Pettersen; 2017, Theorem 5). Finally, the conditions of (Pettersen; 2017, Assumption 2) must be investigated, i.e. the assumption that the interconnection terms, the second vector of (4.76a), has at most linear growth in $\tilde{\mathbf{X}}_1$. From (4.44b) it can be seen that the interconnection term does not grow with the states $\tilde{\mathbf{X}}_1$ as it can be bounded by linear functions of $\tilde{\mathbf{X}}_2$. All conditions of (Pettersen; 2017, Proposition 9) are therefore satisfied, and the origin of the closed-loop system $(\tilde{\mathbf{X}}_1, \tilde{\mathbf{X}}_2) = (\mathbf{0}, \mathbf{0})$ is USGES and UGAS.

Thus, all that remains is to prove boundedness of Eqs. (4.76c)–(4.76d). Boundedness of Eqs. (4.76c)–(4.76d) is established in the proof of Proposition 4.4 in Moe et al. (2016) where it is shown that the equilibrium points $(\tilde{\psi}, s, \dot{\tilde{\theta}}_r) = \mathbf{0}$ and $(\tilde{u}, \dot{\tilde{\theta}}_u) = \mathbf{0}$ are UGS, which implies that both $\tilde{\theta}_r$ and $\tilde{\theta}_u$ are bounded. Hence the proof of Theorem 4.2 is concluded. \square

4.6 Robustness against non-vanishing perturbations

In this section, robustness properties against non-vanishing perturbations of the formation and barycenter task definitions presented in Section 4.4 are investigated. Every realistic system will be perturbed by unknown disturbances caused by e.g., modeling uncertainties and errors, and other disturbances such as environmental disturbances.

A system that works as intended in simulations may not work as intended when tested in a real-world scenario as the simulation model has failed to capture the whole, real, dynamics of the system. Therefore, investigating the robustness guarantees of a system could be crucial to ensure that it will still be stable and behave as intended when operating under non-ideal conditions in the real world.

The importance of investigating the robustness properties of the NSB task definitions in Section 4.4 should be obvious as the term containing the reaction forces in (2.1b) are left out of the vessel model (4.59) used in the stability analyses in Section 4.5. Consequently, the stability analysis was performed without considering how the physical inter-vessel connection will affect the system error dynamics. Additional analysis is therefore required to investigate how the addition of the cable will affect the results in Section 4.5.

In the following analysis, the cable will be treated as an unknown bounded state-dependent perturbation due to the complexity of the cable model from Chapter 3. The design objective of the cable model presented in Chapter 3 was to obtain a model that performed sufficiently compared to logged data from real-world experiments to be used in simulations. The implications are that the complexity renders the model impractical for use in control design and analysis, which is evident by looking at the model complexity and size already in Example 1 with $n = 2$. For larger values of n , the model complexity increases such that any attempts using the resulting model in control design and analysis becomes infeasible.

In particular, the effect from the cable is modeled as a perturbing term $\mathbf{g}(t, \mathbf{x})$ of the form

$$\dot{\mathbf{x}} = \mathbf{f}(t, \mathbf{x}) + \mathbf{g}(t, \mathbf{x}) \quad (4.82)$$

where $\mathbf{x} \triangleq [\tilde{\mathbf{X}}_1^T \tilde{\mathbf{X}}_2^T]^T$ and $\mathbf{f}(t, \mathbf{x})$ is given by the closed-loop systems Eqs. (4.69a)–(4.69b) and Eqs. (4.76a)–(4.76b) for the formation and barycenter tasks respectively.

Lemma 4.5 (Boundedness of the closed-loop formation task). *Assume that the condi-*

tions of Theorem 4.1 are satisfied. Then, for all uniformly bounded disturbances $\mathbf{g}(t, \mathbf{x})$, irrespective of their magnitude, the solution of the perturbed system (4.82), with \mathbf{f} given by Eqs. (4.69a)–(4.69b), is uniformly bounded.

Proof. From the fact that the closed-loop system of the formation task Eqs. (4.69a)–(4.69b) is UGES, (Khalil; 2002, Lemma 9.2) gives that the perturbed system (4.82) are uniformly bounded for all bounded disturbances, irrespective of their magnitude. \square

Lemma 4.6 (Boundedness of the nominal barycenter task). *Assume that the conditions of Proposition 4.2 are satisfied. Then, there exists a positive constant δ , a constant $c \in (0, 1)$ and a time $T \geq 0$, such that if the disturbances are bounded by*

$$\|\mathbf{g}(t, \mathbf{x})\| \leq \delta, \quad (4.83)$$

then the solutions of the nominal system

$$\dot{\tilde{\mathbf{X}}}_1 = \begin{bmatrix} -\frac{1}{2} (U_{d,1} + U_{d,2}) \frac{y_{pb}^p}{\sqrt{\Delta^2 + (y_{pb}^p)^2}} - \kappa(\theta) \dot{\theta} x_{pb}^p \\ -k_\theta \frac{x_{pb}^p}{\sqrt{1 + (x_{pb}^p)^2}} + \dot{\theta} \kappa(\theta) y_{pb}^p \end{bmatrix}, \quad (4.84)$$

perturbed by the disturbances $\mathbf{g}(t, \mathbf{x})$, satisfy

$$\|\tilde{\mathbf{X}}_1(t)\| \leq \sqrt{\frac{k_2}{k_1}} \|\tilde{\mathbf{X}}_1(t_0)\| e^{-\frac{(1-c)k_3}{2k_2}(t-t_0)} \quad (4.85)$$

$\forall t_0 \leq t \leq t_0 + T$, and

$$\|\tilde{\mathbf{X}}_1(t)\| \leq \frac{k_4}{k_3} \sqrt{\frac{k_2}{k_1}} \frac{\delta}{c} \quad \forall t \geq t_0 + T. \quad (4.86)$$

Proof. Using the same Lyapunov function candidate as in the proof of Proposition 4.2: $V_{p_{pb}}(\tilde{\mathbf{X}}_1) = \frac{1}{2} (x_{pb}^p)^2 + \frac{1}{2} (y_{pb}^p)^2$, the partial derivative is bounded by

$$\left\| \frac{\partial V}{\partial \tilde{\mathbf{X}}_1} \right\| = \left\| [x_{pb}^p \ y_{pb}^p]^T \right\| \leq \|\tilde{\mathbf{X}}_1(t)\|. \quad (4.87)$$

Hence, the conditions of (Pettersen; 2017, Lemma 12) is satisfied with $k_{1,2,3}$ and a from Proposition 4.2 and $k_4 = 1 = 2k_2$. Consequently, the upper bound on the

disturbance may be expressed as

$$\|\mathbf{g}(t, \mathbf{x})\| \leq \delta < \frac{k_3}{k_4} \left(\frac{k_1}{k_2} \right)^{\frac{1}{a}} r c, \quad (4.88)$$

with r given by Proposition 4.2. Hence, the conditions of (Pettersen; 2017, Lemma 12) is satisfied, and the solutions of the nominal system (4.84) perturbed by the disturbance are uniformly bounded by (4.85) and (4.86) respectively. \square

Lemma 4.7 (Boundedness of the closed-loop barycenter task). *Assume that the conditions of Theorem 4.2 are satisfied. Then, the solutions of the perturbed system (4.82), with \mathbf{f} given by Eqs. (4.76a)–(4.76b) is uniformly bounded for disturbances $\mathbf{g}(t, \mathbf{x})$ satisfying the condition*

$$\|\mathbf{g}(t, \mathbf{x})\| \leq \delta, \quad (4.89)$$

that is, the magnitude of the perturbation is bounded by a sufficiently small value δ .

Proof. Since USGES is proven of the cascaded system Eqs. (4.76a)–(4.76b) it implies that the total cascaded system is both UGAS and ULES. Consequently, the system is ULES in a neighbourhood about the origin, inheriting the robustness properties of ULES systems. Thus, (Khalil; 2002, Lemma 9.2) can be used to conclude that for sufficiently small magnitudes of the nonvanishing perturbations, the solutions of Eqs. (4.76a)–(4.76b) will remain bounded. However, without knowing the Lyapunov function candidate of the total cascaded system, it is not possible to quantify the upper bound of the perturbation magnitude, meaning the robustness conclusion becomes a qualitative one. \square

It should be observed that it is not possible to prove robustness properties of the closed-loop barycenter task dynamics in Lemma 4.7 by (Pettersen; 2017, Lemma 12). This is because (Pettersen; 2017, Lemma 12) require the total system to satisfy the conditions of (Pettersen; 2017, Theorem 5), while the cascaded system Eqs. (4.76a)–(4.76b) satisfies only satisfies the conditions of (Pettersen; 2017, Proposition 9).

As the conditions of (Pettersen; 2017, Theorem 5) are Lyapunov *sufficient* conditions, they are *not* automatically *necessary* conditions for USGES. Consequently, it cannot be concluded that there exists a Lyapunov function candidate of the total cascaded system satisfying the conditions of (Pettersen; 2017, Theorem 5) from the fact that the cascaded system satisfy the conditions of (Pettersen; 2017, Proposition 9).

To be able to show the robustness of the total cascaded system using (Pettersen; 2017, Lemma 12), a new LFC must be found, and proven to satisfy the conditions of

(Pettersen; 2017, Theorem 5). However, this is non-trivial due to the linear interconnection term in (4.76a) which complicate the proof that \dot{V} is negative definite.

4.7 Path generation

In this section, a method for generating a θ -parametrized path for the barycenter task is presented. As stated in Section 1.3, the vessels must be able to follow a path denoted by waypoints. Most other traditional LOS methods operating with waypoints, e.g., see Fossen (2011) assume that the waypoints are connected by straight-line path segments, removing the need of parametrization. However, since the LOS method presented in Section 4.4.3 are designed to be able to follow curved paths, a method must be chosen for interpolating the path in-between the waypoints.

Path generation methods based on waypoints are not a new topic, and several existing methods exist. In Dubins (1957), it was shown that the shortest path, in time, between two configurations with constant speed is a path formed by straight lines and circular arc segments. These Dubins paths are a widely used method for connecting waypoints in the context of LOS methods. However, they have the drawback that a jump in the yaw rate r_d is experienced in the transitions between the straight line and circle segments, as the first derivative of the joined path is discontinuous, causing a small offset during cross-tracking Fossen (2011).

Another approach for path generation is to use interpolating methods. Many of these methods are based on piece-wise cubic polynomials, where several different methods for interpolating cubic polynomials exist, where each method will produce a different path depending on the rules and constraints used. Two of the most used methods are the *Piecewise Cubic Hermite Interpolation Polynomial* (PCHIP) Fritsch and Carlson (1980) and the *Cubic Spline* method, which are implemented as the `pchip` and `spline` functions in Matlab respectively. The resulting polynomials by the first method are created such that the first derivatives are continuous, and shape-preserving by selecting the slopes such that it respects monotonicity. However, the second derivatives are not guaranteed to be continuous, meaning jumps are possible. For the second method, the second derivatives are continuous, resulting in smoother polynomials than for the first method. However, they tend to have more oscillations if the original data is non-smooth, as shown in Fig. 4.5.

Consequently, to generate a θ -parametrized path from waypoints, the PCHIP interpolation method is chosen as this will generate a path with less oscillations and which is closer to straight lines. The resulting path for N waypoints will therefore

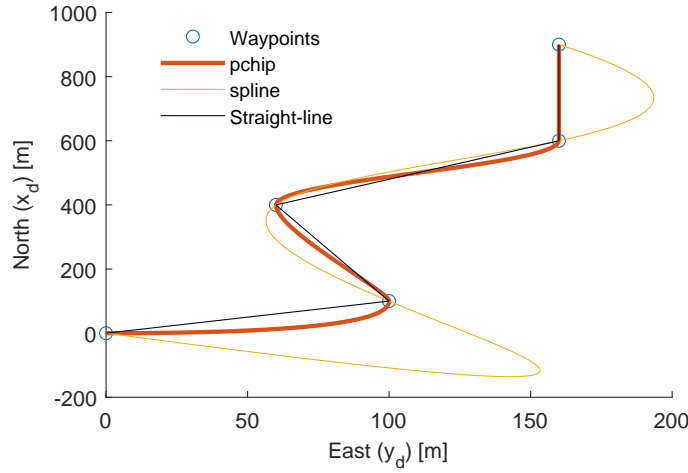


Figure 4.5: Waypoint interpolation methods

be a piece-wise cubic polynomial composed by $N - 1$ segments, where each segment may be described by the polynomials

$$x_p(\theta) = a_3\theta^3 + a_2\theta^2 + a_1\theta + a_0 \quad (4.90a)$$

$$y_p(\theta) = b_3\theta^3 + b_2\theta^2 + b_1\theta + b_0, \quad (4.90b)$$

where $(x_p(\theta), y_p(\theta)) \in P$ is the desired position of the barycenter along the path. Furthermore, the breaks $\theta_k \in \{0, 1, \dots, N\}$ of the polynomials are chosen according to Fossen (2011) such that the path through the waypoints (x_{k-1}, y_{k-1}) and (x_k, y_k) must satisfy

$$x_p(\theta_{k-1}) = x_{k-1}, \quad x_p(\theta_k) = x_k \quad (4.91a)$$

$$y_p(\theta_{k-1}) = y_{k-1}, \quad y_p(\theta_k) = y_k. \quad (4.91b)$$

Subsequently, as the θ -parametrized path is parametrized by a unit size path variable, the path update law (4.31) must be converted to unit size by

$$\dot{\theta} = \frac{\frac{1}{2}U_1 \cos(\chi_1 - \gamma_p) + \frac{1}{2}U_2 \cos(\chi_2 - \gamma_p) + k_{\theta} f_{\theta}(x_{pb}^p, y_{pb}^p)}{\sqrt{x_p'(\theta)^2 + y_p'(\theta)^2}}, \quad (4.92)$$

where $(\cdot)'$ denotes the partial derivative with respect to θ . Note how this only affects the implementation of the method, and not the theoretical results presented earlier, as it is related to the choice of path generation method, while the theoretical results

were performed for arbitrary paths.

5 | Simulations

In this chapter, several simulations are run in MATLAB/Simulink to see how the formation control method presented in Chapter 4 performs in different scenarios. First, several scenarios are performed with the vessel model and maneuvering controllers presented in Section 4.5, to investigate how the formation control method performs in a hypothetical ideal case. Next, the performance is evaluated using the more realistic vessel model and maneuvering controllers from Chapter 2. Then, the vessels are attached to the cable modeled in Chapter 3 to evaluate the formation control method performance for the total system. Finally, a discussion of the simulation results is presented.

5.1 Ideal case

In this section, several scenarios are tested using the ideal vessel model and maneuvering controllers presented in Section 4.5, to illustrate the theoretical stability analysis performed in Section 4.5. In the first scenario, the obstacle avoidance and formation tasks are deactivated, to demonstrate the isolated barycenter task performance on a sinusoidal path. Then, all tasks are activated to see the performance of the total method in the ideal case.

For both scenarios in this section, the vessels were subject to a constant irrotational ocean current with speed $V_{\max} = 1$ m/s with an angle $\beta_c = -135^\circ$ from the inertial frame, giving the ocean current components $V_x = V_y \approx -0.707$ m/s. The desired along-path speed is chosen constant to $u_d = 3$ m/s. Furthermore, to ensure that the dynamics of Odin and Frigg may be approximated by that of a displacement vessel, rendering the vessel model (4.59) valid, an upper restriction on the maximum surge speed reference from the NSB formation control method is set to $u_{\max} = 5$ m/s.

Using the model parameters of Odin, the upper bound of the path curvature may be found to be $\kappa_{\max} = Y_{\min}/X_{\max} \approx 0.0882$. The controller gains are chosen as $k_\psi = 1.2$, $k_r = 1.3$, $\lambda = 100$, $k_d = 10$, $k_u = 0.1$ and $k_e = 0.1$. Furthermore, the adaptive

gains are chosen as $\gamma_r = 5$ and $\gamma_u = 1$.

For the scenarios considered in this section, the path generation method described in Section 4.7 is not used. Instead, the desired path of the barycenter is defined as

$$P \triangleq \begin{cases} x_p(\theta) = \theta \\ y_p(\theta) = 300 \sin(0.005\theta), \end{cases} \quad (5.1)$$

which has maximum curvature $\max_{\theta \in P} |\kappa(\theta)| = 0.0075$. Hence, the constraint in Lemma 4.3 is satisfied as $\kappa_{\max} < Y_{\min}/X_{\max}$. Furthermore, the condition of Lemma 4.4 can be calculated to be $\mu > 49.5704$ m, which is satisfied by choosing $\mu = 50$ m.

For the obstacle avoidance task, the threshold for the minimum allowed distance between the vessels is chosen as $d_0 = 20$ m and the proportional gain as $\lambda_o = 1$. On request from FFI, the numerical value of the desired task function value is not given in this thesis, but chosen as $\sigma_{f,d}^p = [0 \quad -d_f]^T$, according to (4.20). This corresponds to that vessel 1 should be located at port side. Furthermore, the matrix of proportional gains are chosen as

$$\Lambda_f^p = \begin{bmatrix} 2.5 & 0 \\ 0 & 0.3 \end{bmatrix}, \quad (5.2)$$

which implies that an error in the along-track direction should be penalized more than in the cross-track direction. This is chosen to have the vessels maintain a better formation throughout the corners.

5.1.1 Only barycenter task active

In this scenario, the system is simulated with only the barycenter task being active to illustrate the theoretical results for the barycenter task presented in Section 4.5.2.

The resulting trajectories of both vessels and the barycenter trajectory are shown in Fig. 5.1. It can be observed from the yellow vessels that neither vessels' heading is parallel to the desired path. Instead, they maintain a non-zero sideslip angle to compensate for the ocean current, which is expected for underactuated vessels. Thus, the vessels' heading is not aligned with the path. Interestingly, the velocities are aligned, ensuring proper path following without any knowledge about the ocean current.

The path following errors of the different tasks are presented in Fig. 5.2, where it is shown that both the along-track x_{pb_p} and cross-track errors y_{pb_p} converge to zero for the barycenter task. From the last plot in Fig. 5.2 it can be seen that since the formation task is deactivated, the vessels will not maintain their desired

formation, but rather keep approximately their initial relative positions throughout the simulation while moving the barycenter along the desired path.

From Fig. 5.3, it can be seen that both the surge and heading states converge exponentially to their desired values. Furthermore, it can be observed that the sway velocity for both vessels is non-zero due to the curvature of the path and the ocean currents. However, they remain bounded throughout the simulation.

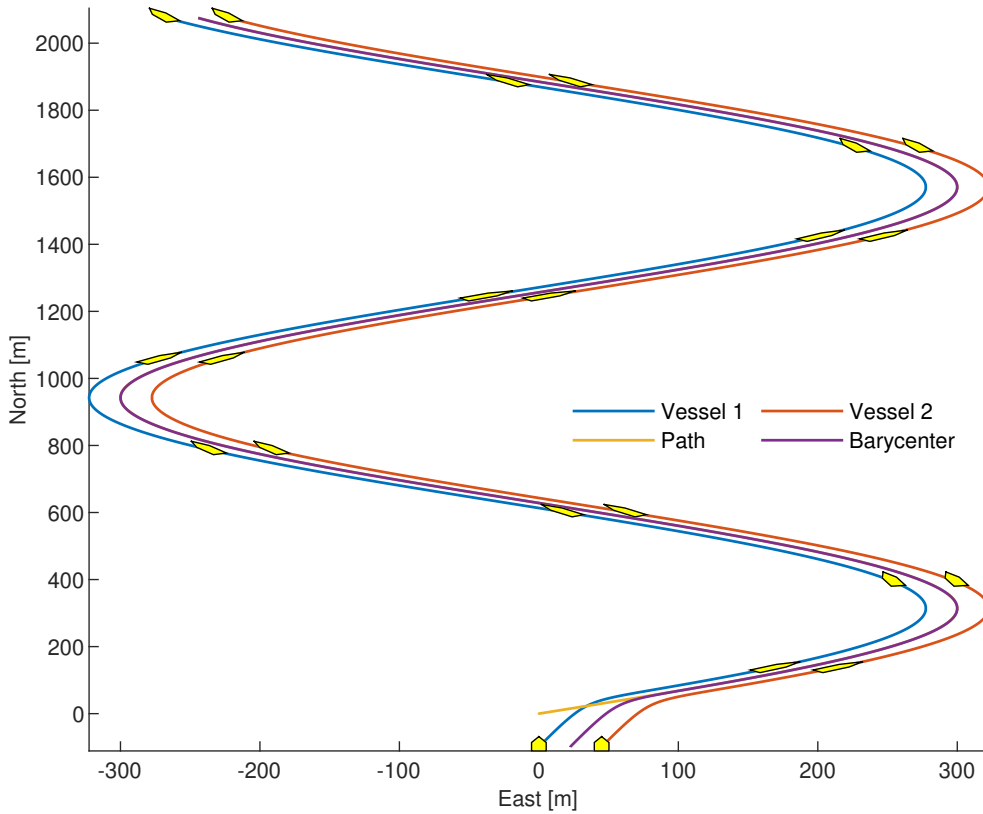


Figure 5.1: Path following of the desired sinusoidal path with only the barycenter task active.

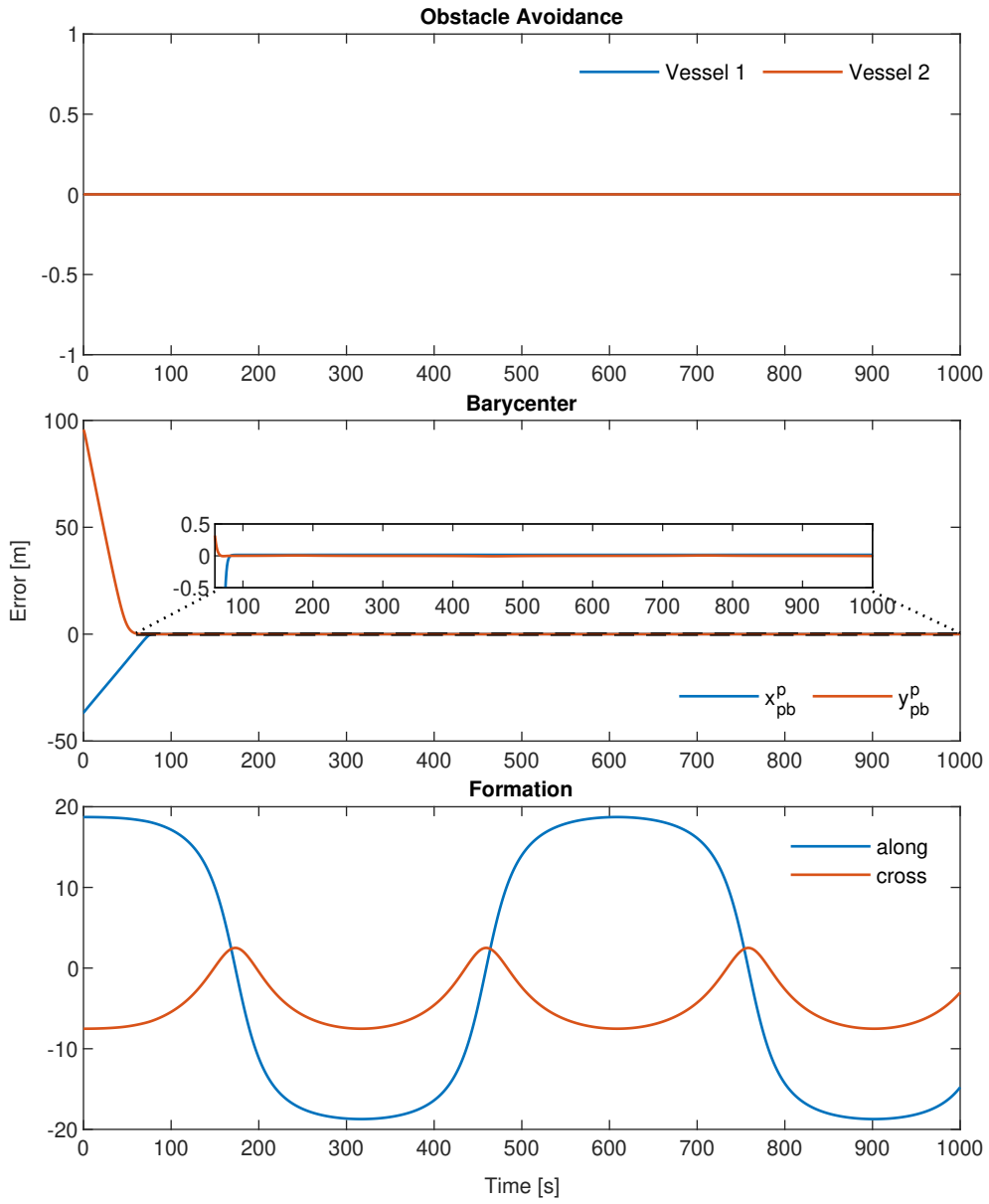


Figure 5.2: NSB errors of the desired sinusoidal path with only the barycenter task active.

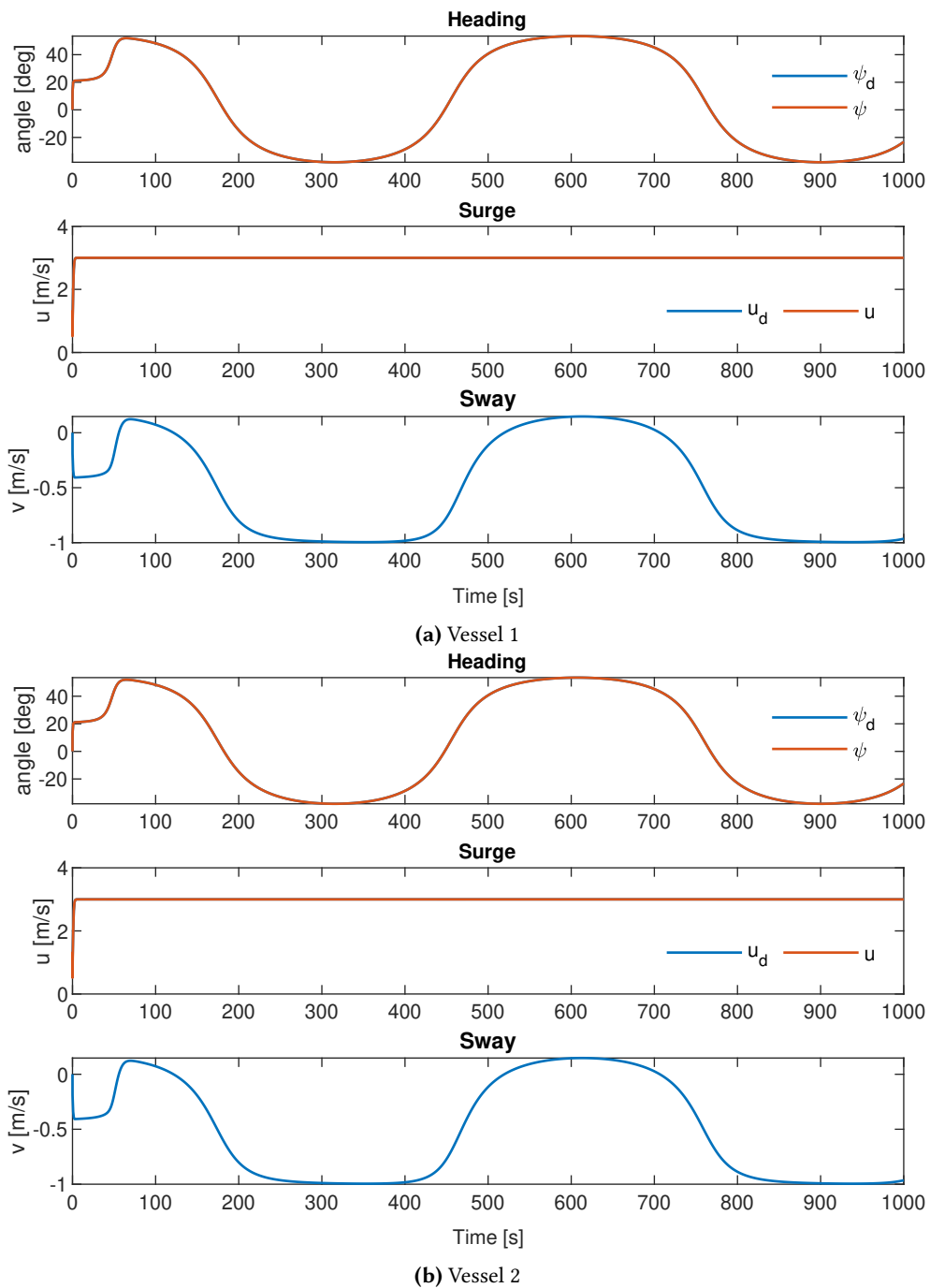


Figure 5.3: Desired vs. actual heading (top), surge (middle) and sway (bottom) of the desired sinusoidal path with only the barycenter task active.

5.1.2 All tasks active

In this scenario, the system is simulated with all tasks activated to illustrate the theoretical results for when the tasks are merged in Section 4.4.4.

The resulting trajectories of both vessels, and the barycenter trajectory are shown in Fig. 5.4. It can be observed that the vessels maintain their desired formation while making the barycenter follow the desired path. It can also be seen that the curved path and the ocean currents make both vessels operate with a non-zero sideslip angle.

The path following errors of the three tasks can be seen in Fig. 5.5. While the vessels can make the barycenter follow the path throughout the simulation, small increases can be seen for the formation task errors in the corners. It is mostly the along-track error that is affected, but a small increase can be seen for the cross-track error. However, whenever the path is almost straight, the formation task errors converge to zero, meaning the formation objective is obtained.

It is of little surprise that the along-track error is affected more than the cross-track error as the outer vessel needs to cover a much larger distance throughout the corner than the inner vessel. Thus, the inner vessel needs to slow down, while the outer vessel needs to increase its surge speed, as observed in Fig. 5.6. Here the desired and actual surge speed for the vessels increases above and decreases below the desired along-path speed of $u_d = 3$ m/s in the outer and inner corners respectively.

The magnitude of the error decreases with increasing values of Λ_f . However, with rising values, the resulting performance becomes more aggressive, with more extensive corrections for small errors, see the aggressive maneuver by the second vessel towards vessel one at the beginning of Fig. 5.4, and with the risk of introducing oscillations to the system, as experienced in Eek (2019). Therefore, a trade-off between formation task errors throughout corners and the risk of introducing oscillations to the system must be made.

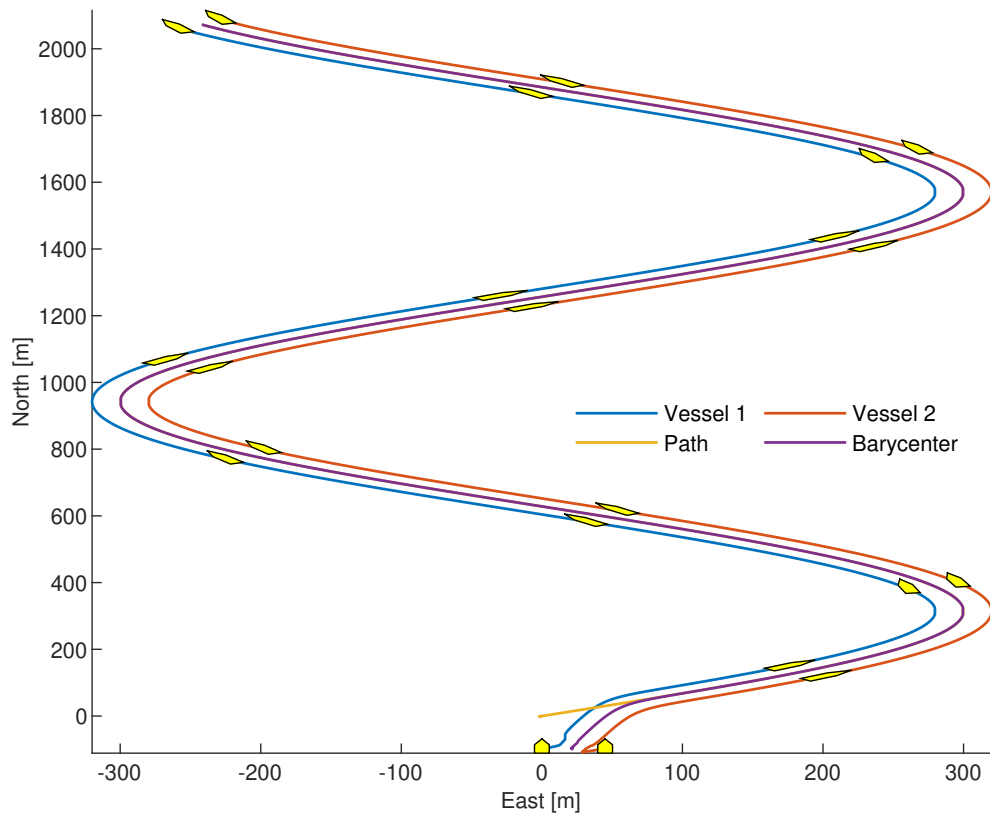


Figure 5.4: Path following of the desired sinusoidal path with all tasks active.

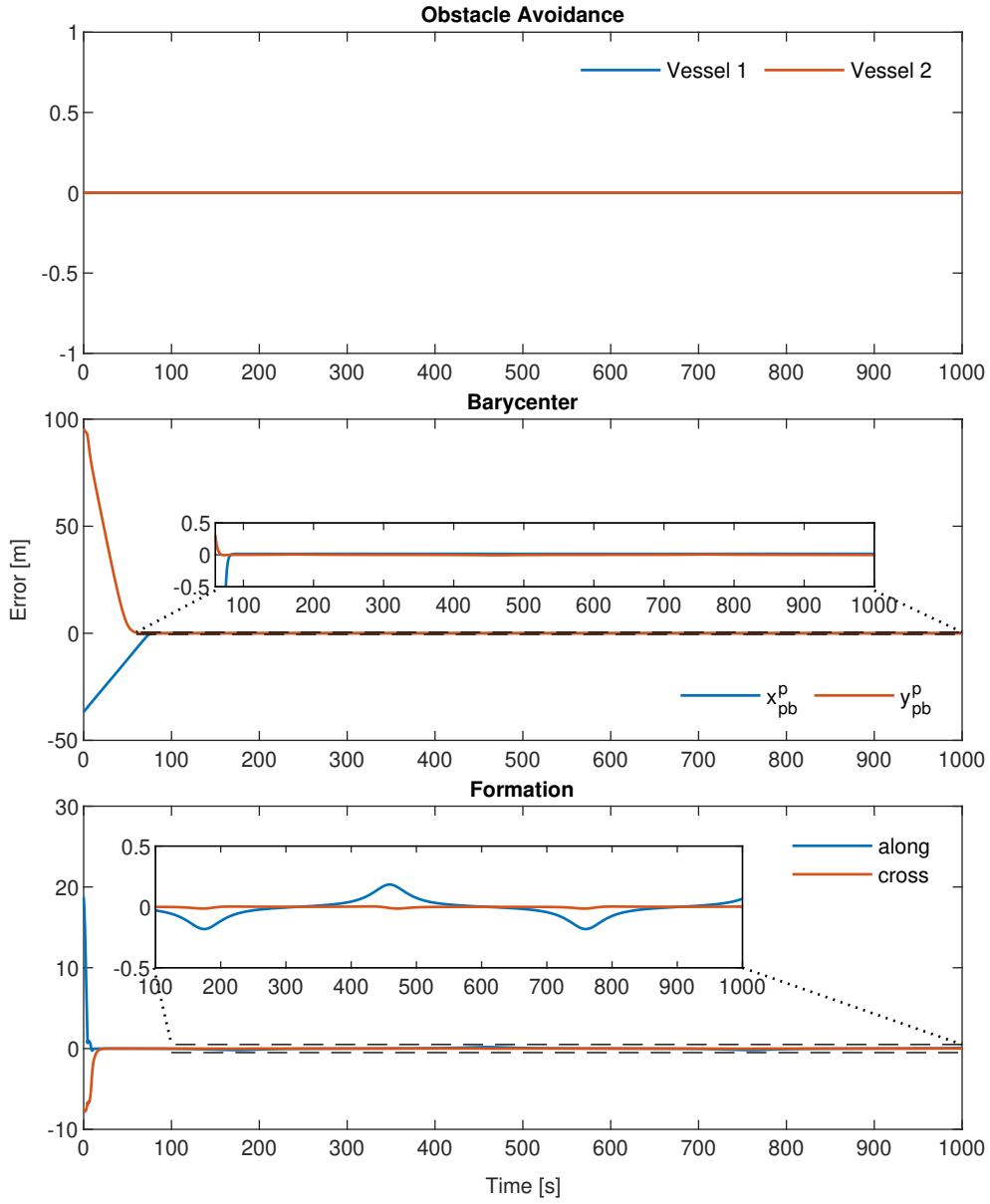
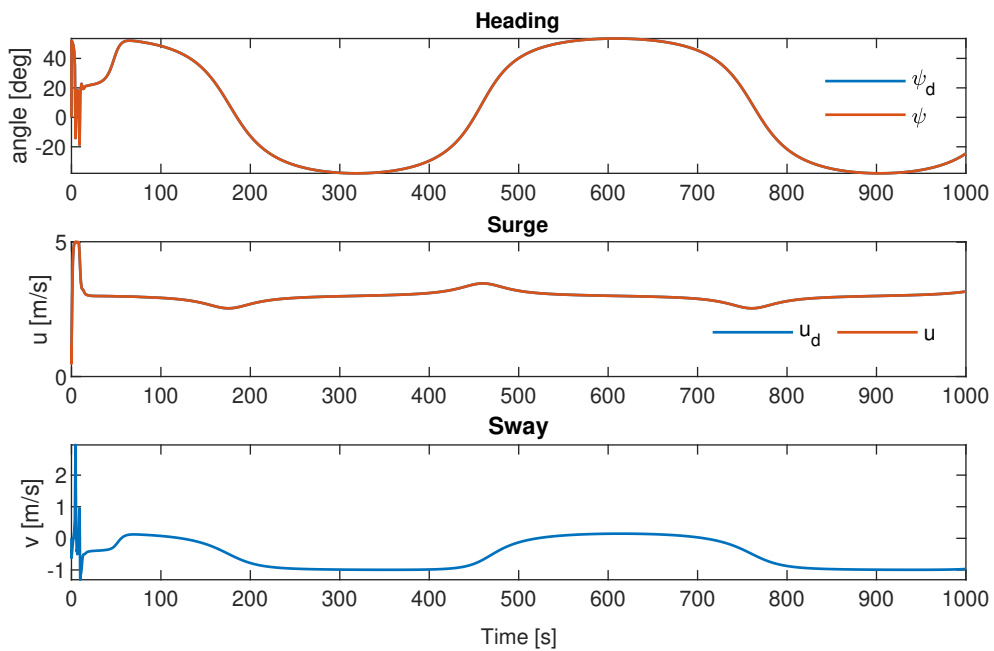
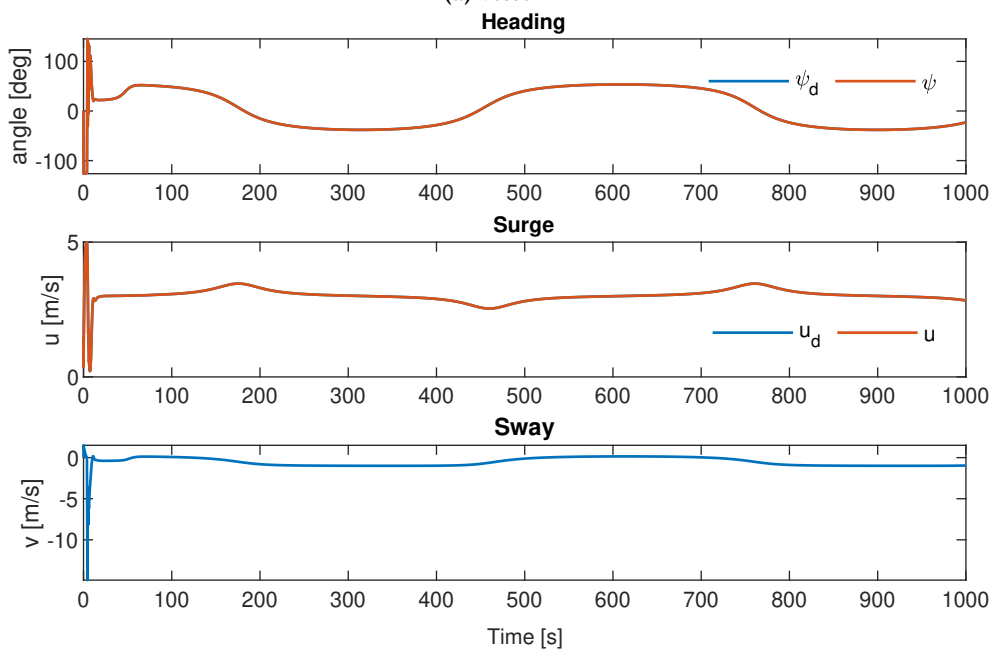


Figure 5.5: NSB errors of the desired sinusoidal path with all tasks active.



(a) Vessel 1



(b) Vessel 2

Figure 5.6: Desired vs. actual heading (top), surge (middle) and sway (bottom) of the desired sinusoidal path with all tasks active.

5.2 Realistic vessel model without cable

In this section, several scenarios are tested using the realistic vessel model and maneuvering controllers presented in Chapter 2 to illustrate how the formation control method performs using the vessel models of Odin and Frigg.

For all scenarios in this section, the vessels were subject to a constant irrotational ocean current with speed $V_{\max} = 1$ m/s with an angle $\beta_c = -135^\circ$ from the inertial frame, giving the ocean current components $V_x = V_y \approx -0.707$ m/s. The desired along-path speed is chosen constant to $u_d = 3$ m/s. Furthermore, to ensure that the dynamics of Odin and Frigg may be approximated by that of a displacement vessel, rendering the vessel model from Chapter 2 valid, an upper restriction on the maximum surge speed reference from the NSB formation control method is set to $u_{\max} = 5$ m/s.

As the constraints for the path curvature and lookahead distance in Lemmas 4.3–4.4 are calculated using the ideal vessel model, it is not possible to calculate the exact constraints for the realistic vessel model from Chapter 2. However, as the realistic model's performance will never be better than in the ideal case, constraints here must be equal, or more strict, than those in Section 5.1.

Simulating the system with the lookahead distance used in the ideal case, resulted in undesirable oscillations due to the lookahead distance being too small. This is likely caused by a slower vessel response, causing the vessels not to follow the rapid references generated with the lookahead distance used in the ideal case. Hence, a larger lookahead distance of $\mu = 1000$ m is chosen, which is well above the minimum threshold calculated previously, but necessary to avoid oscillations.

For the obstacle avoidance task, the threshold for the minimum allowed distance between the vessels is chosen as $d_0 = 20$ m and the proportional gain as $\lambda_o = 1$. The desired task function value of the formation task is chosen as in Section 5.1, but the numerical value is not given on request from FFI. Furthermore, the matrix of proportional gains are chosen as

$$\Lambda_f^p = \begin{bmatrix} 0.3 & 0 \\ 0 & 0.1 \end{bmatrix}. \quad (5.3)$$

The proportional gains of the formation task are notably lower than the values used in the ideal case. As the vessels' response is faster in the ideal case, selecting higher proportional gains is possible due to the high bandwidth of the maneuvering controllers. However, in the realistic case, the maneuvering controllers' bandwidth

will be lower, giving insufficient bandwidth separation between the NSB system and the maneuvering controllers for high proportional gains, introducing oscillations to the system as experienced in Eek (2019). Thus, the trade-off between formation task errors and the risk of introducing oscillations must be set lower, implying that higher formation task errors are expected in the corners than in the ideal case.

5.2.1 Sinusoidal path

In this scenario, the formation control method with the realistic vessel model is simulated with same path as in Section 5.1 to compare the performance with the ideal case.

The resulting trajectories of both vessels along with the barycenter trajectory are shown in Fig. 5.7. Moreover, it can be observed non-zero sideslip angles for the vessels to compensate for the unknown ocean current.

The path following errors of the three tasks can be seen in Fig. 5.8. Due to the more conservative choice of parameters, it can be seen that neither the barycenter nor formation task errors converge to zero in the curves. Due to the large lookahead distance, the vessels cannot keep the barycenter on the path throughout the corners, resulting in cross-track errors of almost 1 m. Similarly, due to the small proportional gain for the along-track formation, the resulting along-track errors for the formation task is up to almost 2 m.

From Fig. 5.9 it can be seen that the sway velocity for both vessels is non-zero due to the ocean currents and the curvature of the path. However, they remain bounded throughout the simulation. Furthermore, both the surge and heading states converge to their desired values, respectively. However, the heading controller for vessel one is especially affected by some oscillations during the first $t = 100$ s. Interestingly from Fig. 5.9a it can be seen that the surge rapidly increases to 5 m/s in the beginning, before converging to approximately 3 m/s for the rest of the simulation.

In Section 2.3 it was established that the generated yaw moment of the waterjet model is affected by the waterjet throttle demand, which is non-linear, and controlled by the surge maneuvering controller. Hence, the rapid change in the surge will result in a rapid change in the waterjets' throttle demand, with the implication that the generated yaw moment for a given nozzle demand will fluctuate, giving an under-damped response as the linear relationship in Section 2.3.1 is invalidated.

When the surge speed, and by extension the throttle demand, stabilizes, the linear relationship in the generated yaw moment from Section 2.3.1 again renders valid, ensuring approximately exponential tracking for the rest of the simulation.

The hypothesis that rapid changes in the surge dynamics cause the under-damped response of the heading controller is further supported by Fig. 5.9b. Here, the surge controller's initial response is less rapid, with fewer oscillations experienced for the heading controller.

However, no further attempts to improve the maneuvering controllers were made in this thesis as the current response was deemed sufficient for testing the formation control method.

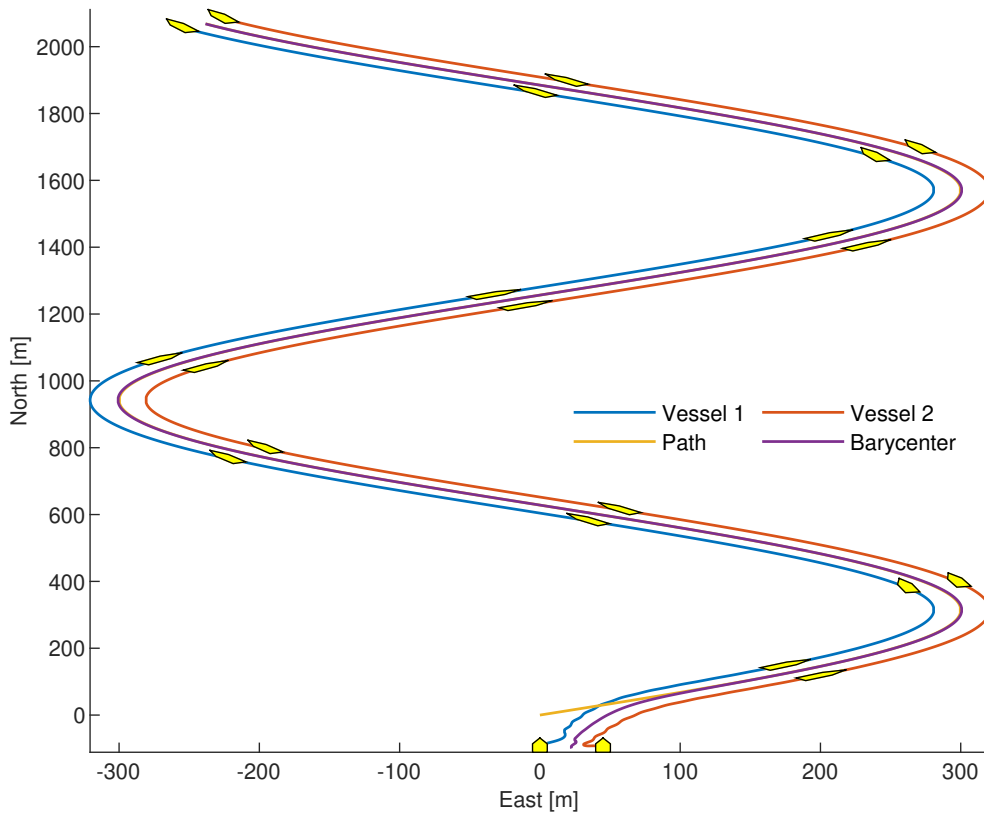


Figure 5.7: Path following of the desired sinusoidal path without cable.

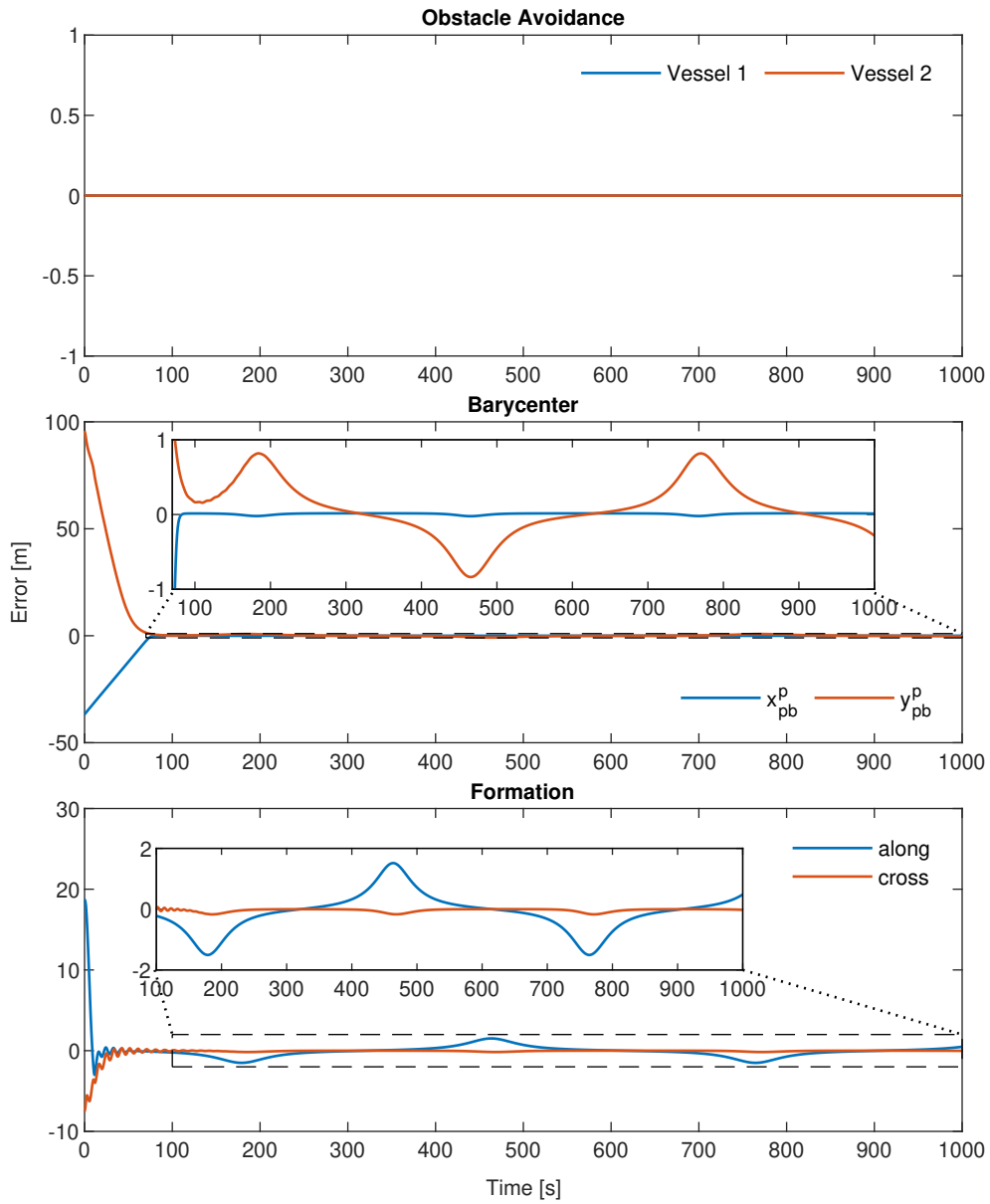


Figure 5.8: NSB errors of the desired sinusoidal path without cable.

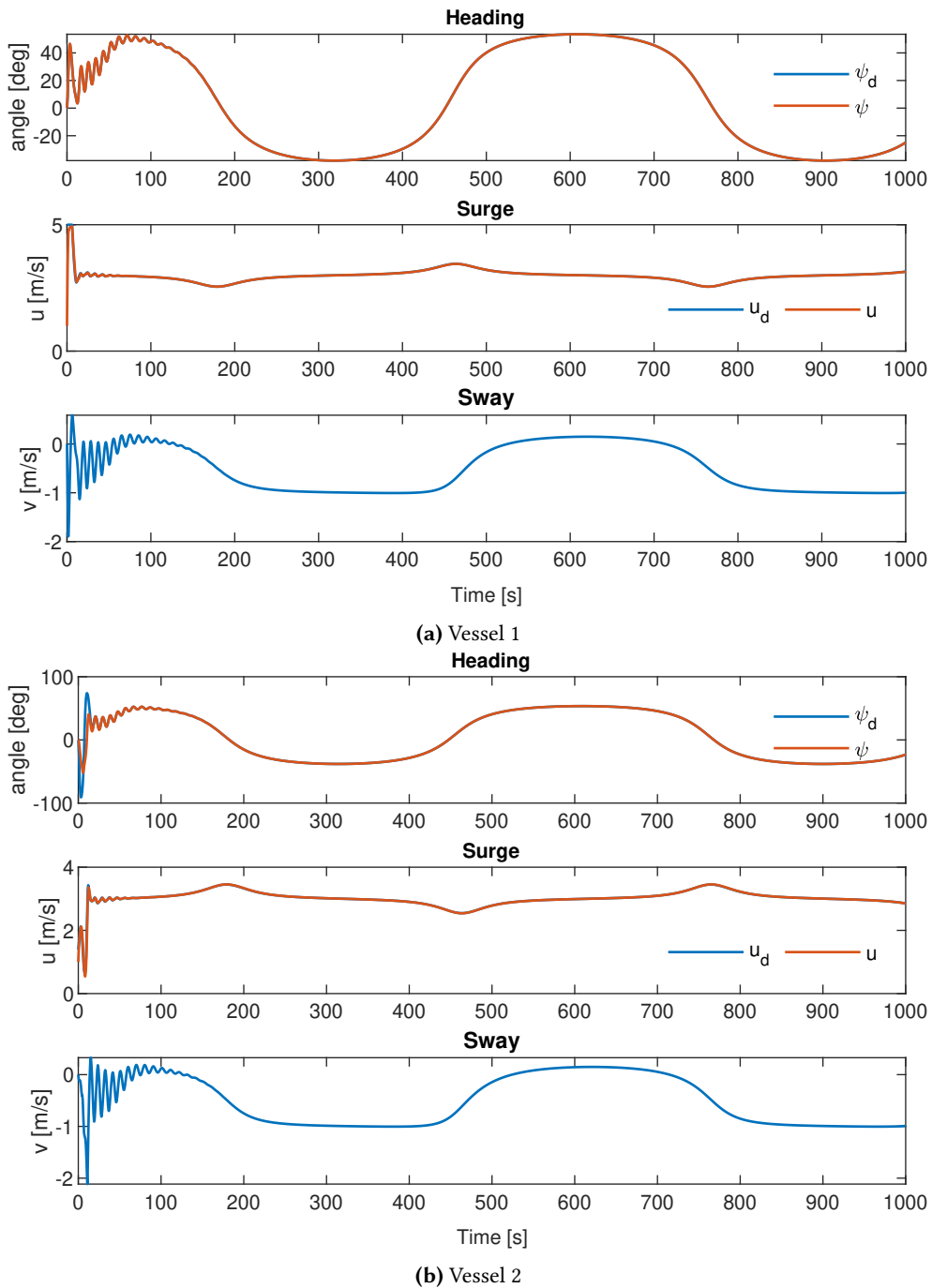


Figure 5.9: Desired vs. actual heading (top), surge (middle) and sway (bottom) of the desired sinusoidal path without cable.

5.2.2 Sweep

In this scenario, the formation control method is simulated to follow a U-shape path to replicate a more realistic path used during a mine-sweep application. The path used in this scenario is identical to that used during experiments in Section 6.3.

The resulting trajectories of both vessels and the barycenter trajectory are shown in Fig. 5.10. The vessels maintain a non-zero sideslip angle to follow the desired path by compensating for the ocean currents.

The path following errors for the three tasks can be seen in Fig. 5.11. It can be observed that all errors converge to zero on the straight-lines. However, especially the along-track formation task error experiences a rapid increase at the beginning of each turn, lower and upper left turns in Fig. 5.10. Due to the PCHIP interpolation method used to generate the path, a rapid change in the path's curvature is experienced in the transition between the different path segments, since only the first derivatives are continuous, causing a jump in the second derivative. Consequently, the outer vessel needs to traverse a much longer distance than the inner vessel, causing a spike in the along-track formation task error.

From Fig. 5.12 it can be seen that the outer vessel increases its surge speed to catch up, and the inner vessel slows down to wait. Although the outer vessel increases its surge speed, it is not limited by the maximum surge speed. The formation task along-track error could be decreased by changing the along-track proportional gain. However, due to the constraints, it is not reasonable to increase the proportional gain as this would introduce oscillations.

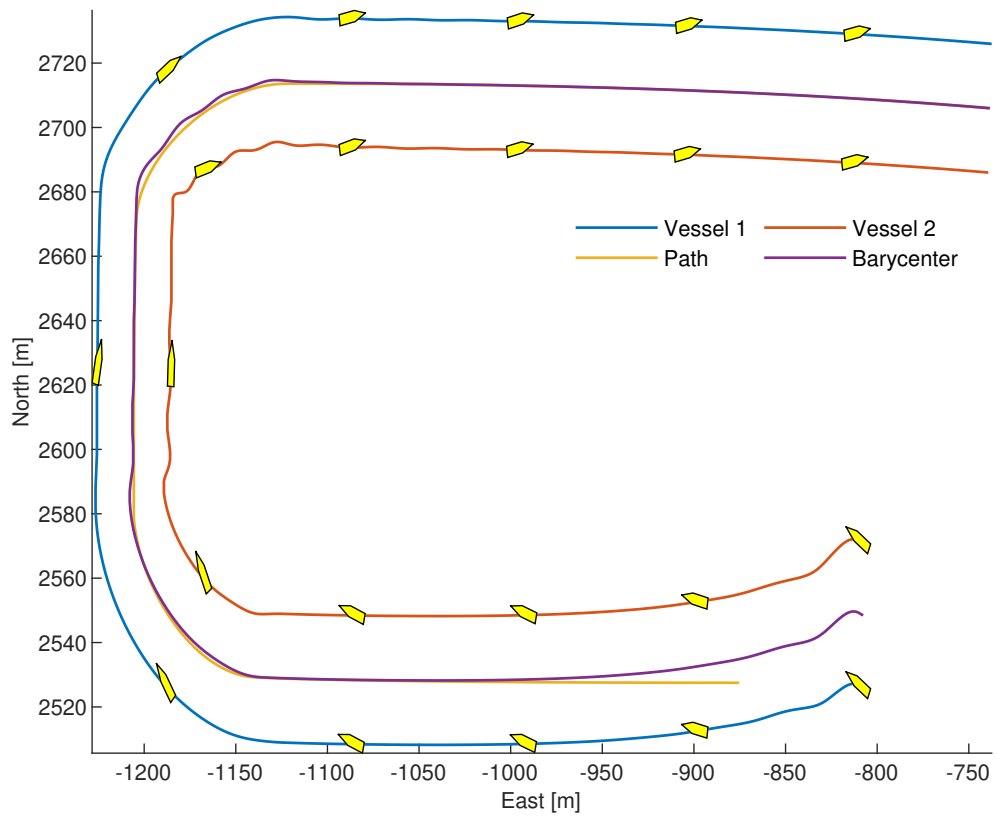


Figure 5.10: Path following of a path representing a mine-sweep without cable.

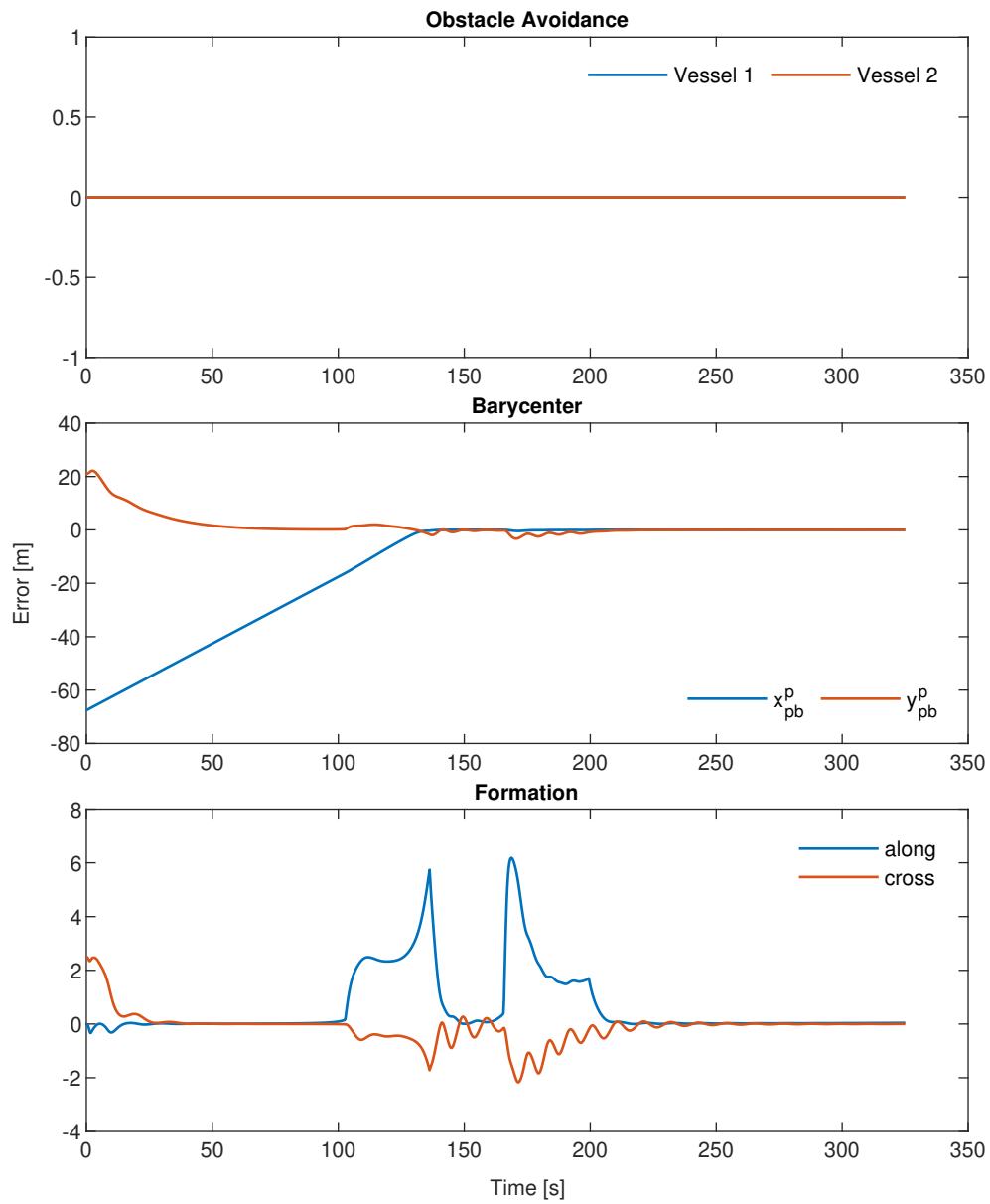


Figure 5.11: NSB errors of a path representing a mine-sweep without cable.

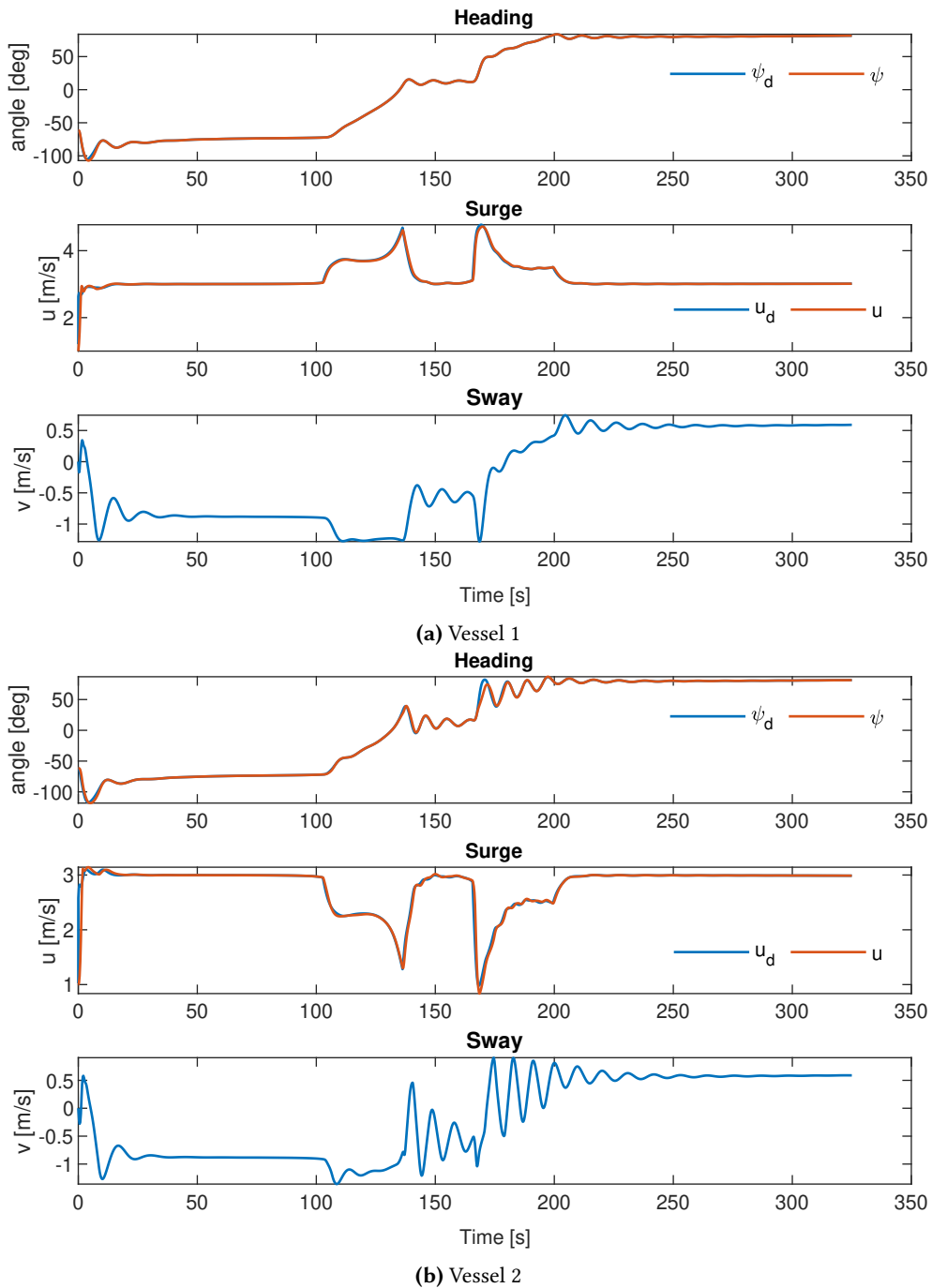


Figure 5.12: Desired vs. actual heading (top), surge (middle) and sway (bottom) of a path representing a mine-sweep without cable.

5.3 Realistic vessel model with cable

In this section, several scenarios are tested using the realistic vessel model and maneuvering controllers presented in Chapter 2, with the cable model presented in Chapter 3 connected to each vessel, to illustrate how the formation control method performs while being affected by the cable dynamics.

For all scenarios in this section, the cable model from Chapter 3 was used, with the parameters according to Section 3.5.2. From Chapter 3 it is known that both vessels and the cable must satisfy the position and velocity constraints (3.3) and (3.14) respectively, at all times. While this is ensured during the simulation, proper care must be made to ensure that the initial conditions also fulfill these constraints. This is solved by specifying the position and velocity for the first vessel, along with the link angles and velocities of the cable. The second's position and velocity are then calculated using the forward kinematics of the cable to ensure that the constraints are fulfilled.

For the remaining parameters, the same values as in Section 5.2 are used.

5.3.1 Sinusoidal path

In this scenario, the two vessels are simulated with the cable attached with the same sinusoidal path as before.

The resulting trajectories of both vessels and the cable along with the barycenter trajectory are shown in Fig. 5.13. It can be observed that the vessels are able to follow the desired path while maintaining their formation when they are towing a cable. Further, the influence by the ocean currents on the cable shape may be seen from the figure, where the cable shape does not follow directly behind vessel trajectories, but instead drifts a bit towards south-west due to the ocean current from north-east. Due to the ocean current's direction, it may be observed that the cable follows better behind the vessels in the right-turns than the left-turns, which is to be expected.

The path following errors of the three tasks can be seen in Fig. 5.14. It can be observed how the task errors are not much affected by the addition of the cable, and that the vessels are still able to achieve their objectives of keeping their formation and following the desired path.

Furthermore, it can be observed that there are still some oscillations on the heading and surge states in Fig. 5.15. However, since the cable acts similarly to a damper, the resulting oscillations are smaller, and fade out quicker, than in Section 5.2.1 for the same scenario without the cable.

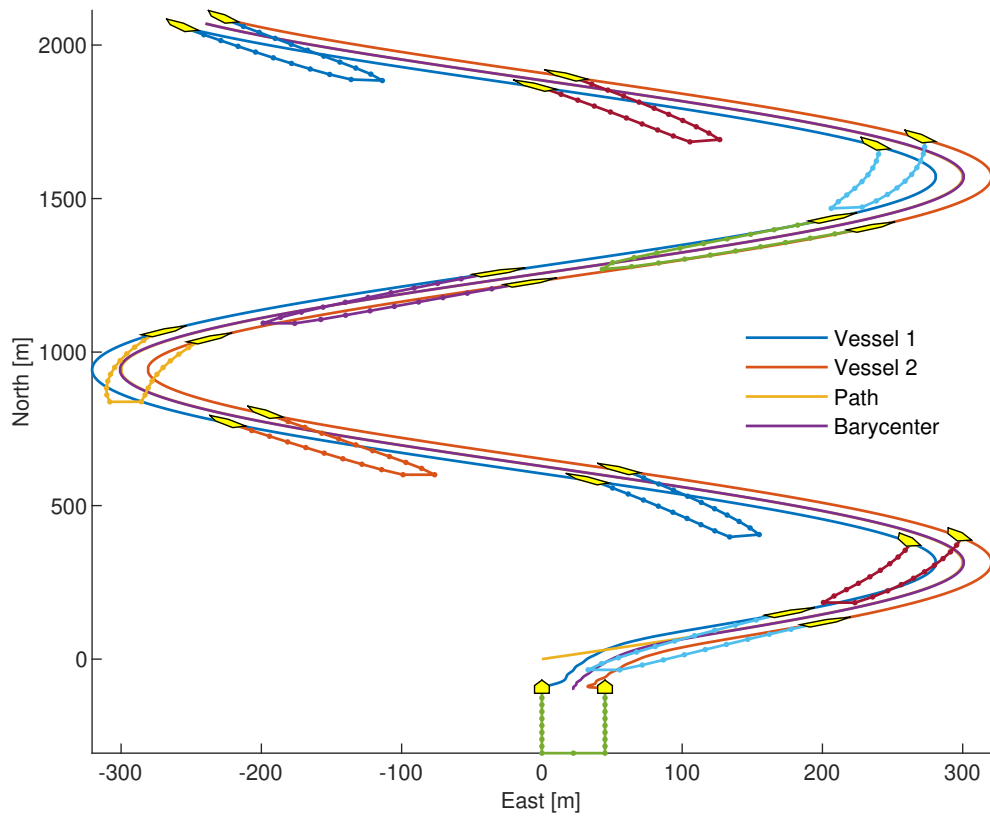


Figure 5.13: Path following of the desired sinusoidal path with the cable.

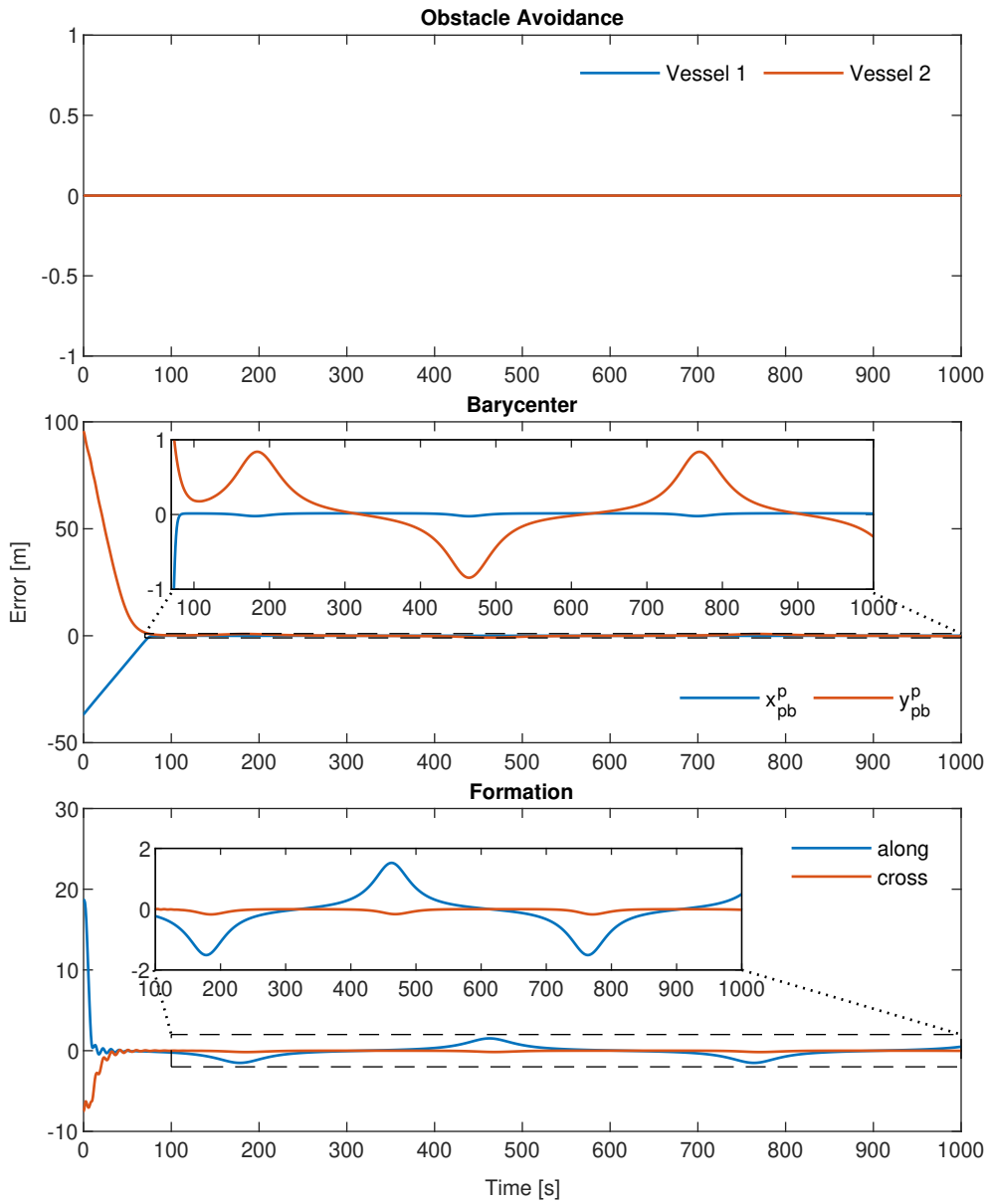


Figure 5.14: NSB errors of the desired sinusoidal path with the cable.

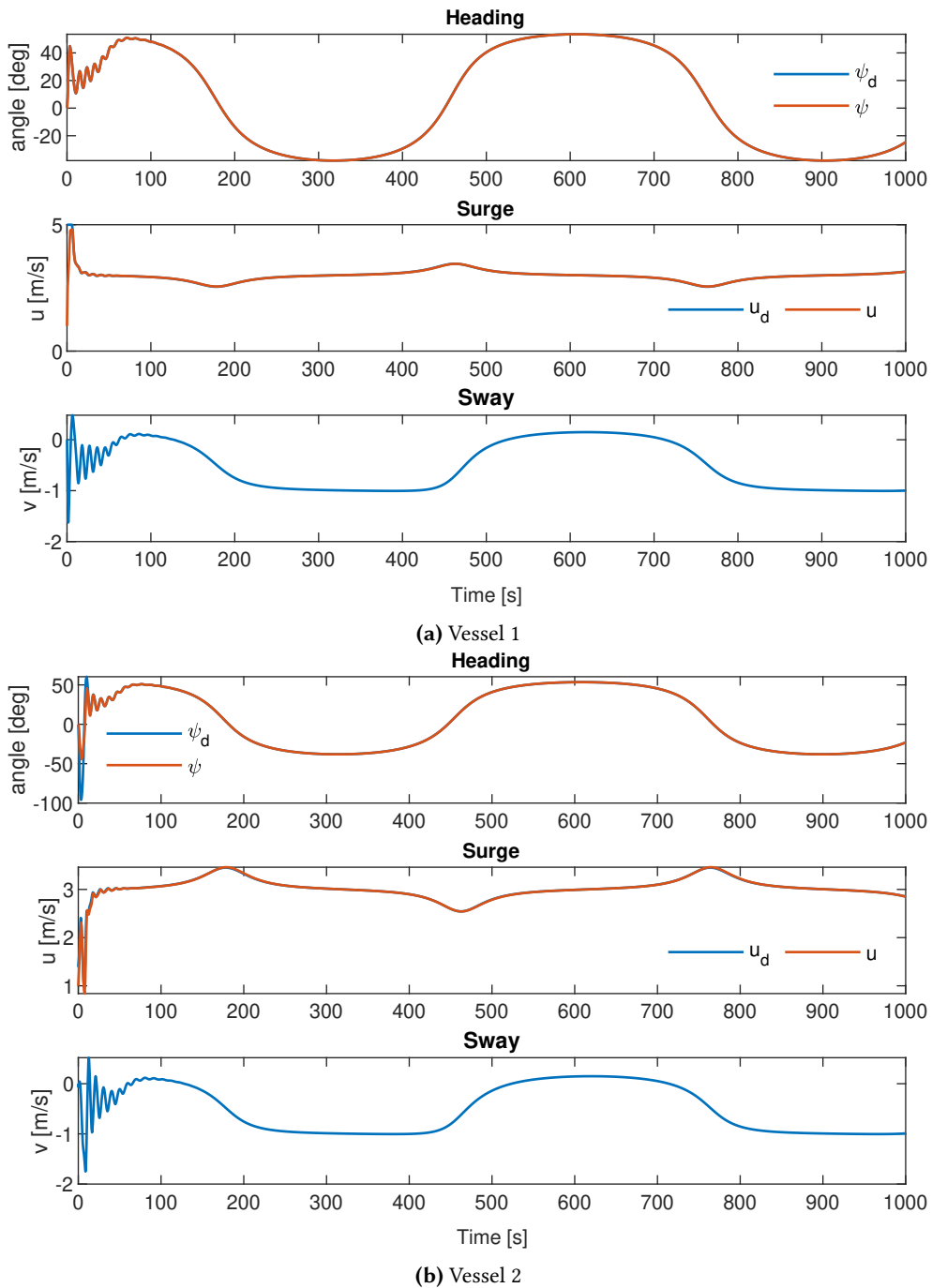


Figure 5.15: Desired vs. actual heading (top), surge (middle) and sway (bottom) of the desired sinusoidal path with the cable.

5.3.2 Sweep

In this scenario, the formation control method is simulated to follow a U-shape path to replicate a more realistic path used during a mine-sweep application with the cable attached.

The resulting trajectories of the vessels along with the barycenter trajectory and the cable are shown in Fig. 5.16. The cable is plotted in different colors to allow easier visualization of the cable shape at each step. While the vessels can converge to the desired path and maintain their desired formation on the straight lines, they are unable to follow the path throughout the turn. The error experienced throughout the turn is because the cable cannot follow the sharp corner due to the hydrodynamic drag forces and torques. Hence, the vessels must take a slightly larger turn radius, which can be seen in Fig. 5.16.

The corresponding path following errors for the three tasks can be seen in Fig. 5.17. The cross-track error for the barycenter task shows that the vessels are unable to follow the path throughout the turn. The maximum cross-track error during the turn is approximately -15 m. For the formation task, it can be observed errors up to 5 m and -9 m in the along-track and cross-track directions respectively.

In Fig. 5.18 it can be seen that while the surge references are followed almost entirely, a significant error in the heading can be observed during the turn. From towing the cable, the vessels will experience an additional torque in the yaw-dynamics. The extra torque from the cable prevents perfect tracking of the desired heading reference, which again prevents the vessels from following the desired path, as seen in Fig. 5.16.

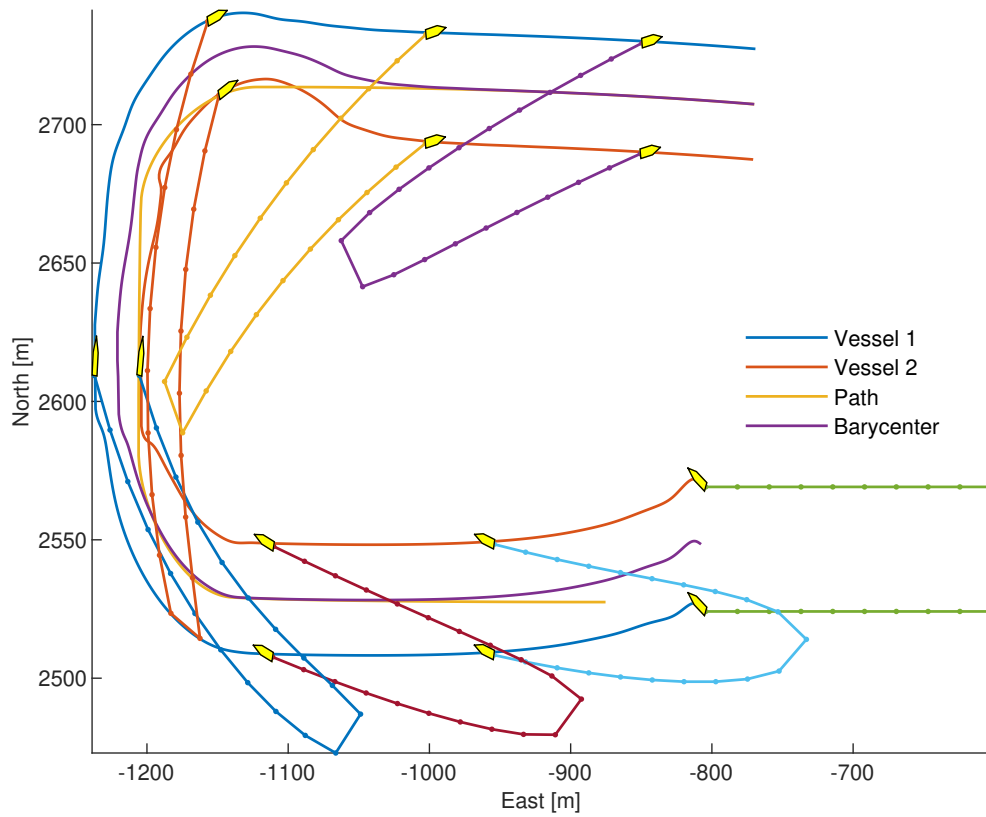


Figure 5.16: Path following of a path representing a mine-sweep with the cable. The cable is plotted in different color for easier visualization of the different time steps.

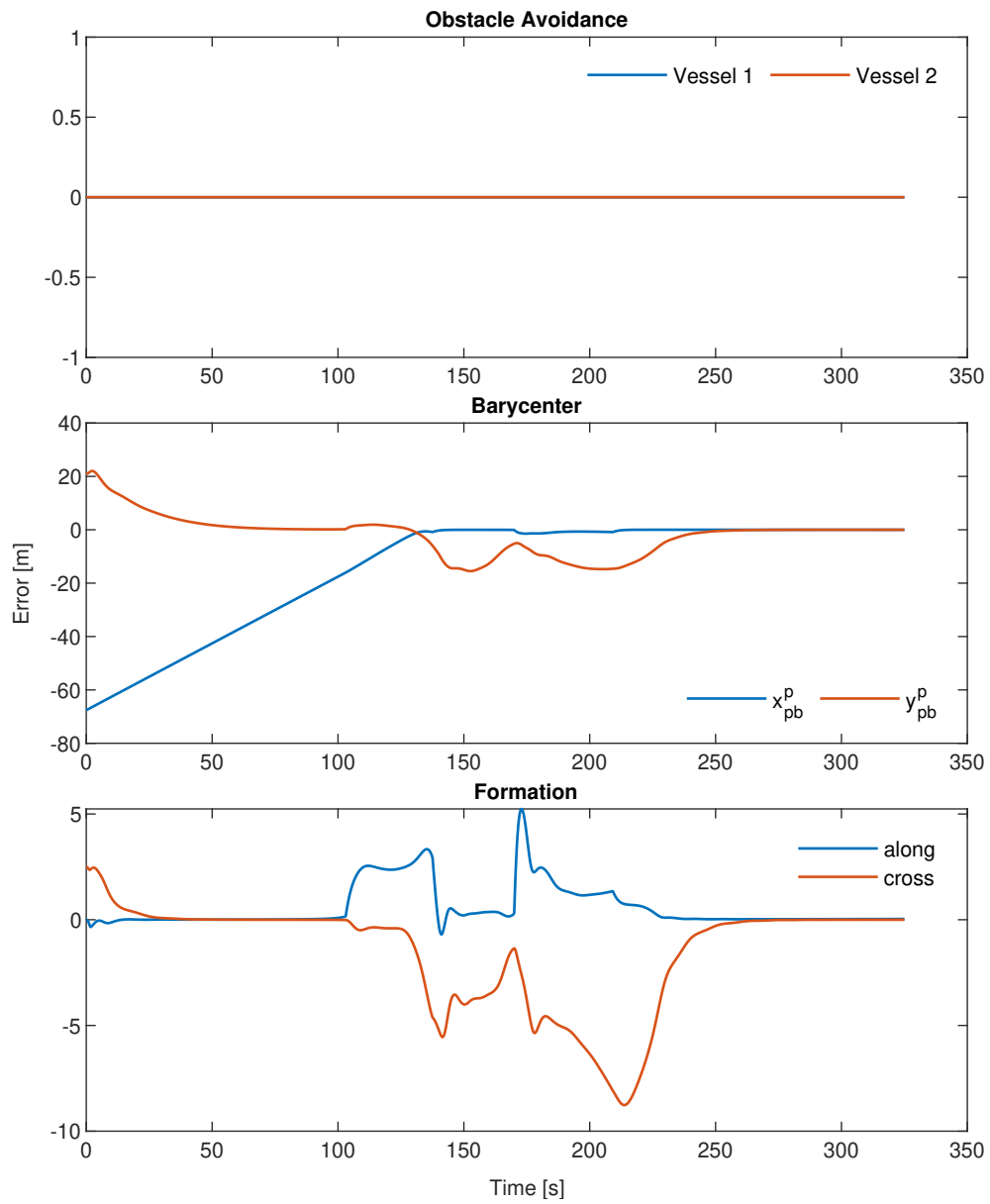


Figure 5.17: NSB errors of a path representing a mine-sweep with the cable.

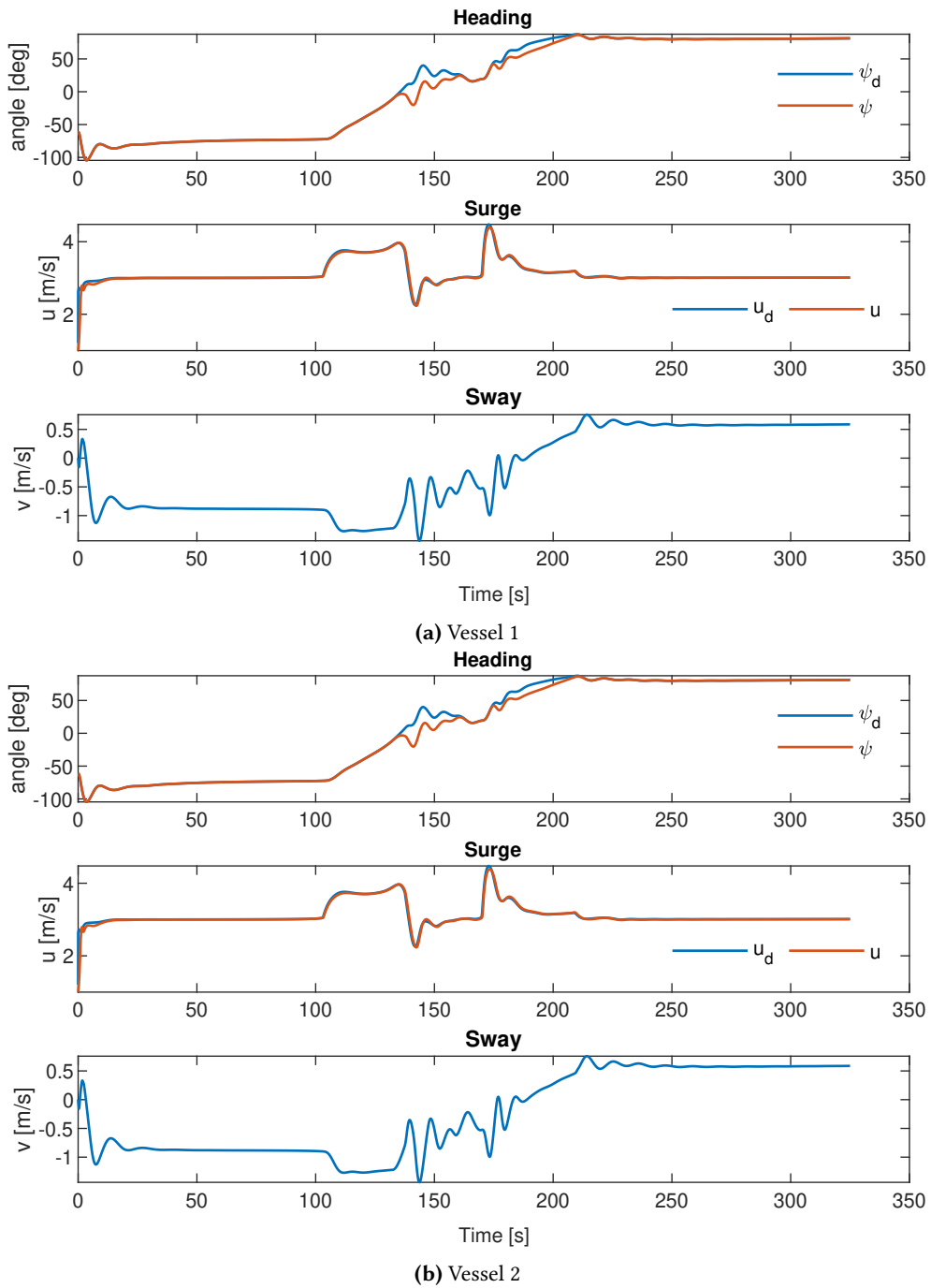


Figure 5.18: Desired vs. actual heading (top), surge (middle) and sway (bottom) of a path representing a mine-sweep with the cable.

5.4 Discussion

In the earlier scenarios, it was established that the ideal model in Section 5.1 outperformed the more realistic model in Section 5.2. The more realistic model suffers from a slower response than the ideal case due to the actuator dynamics and constraint of the waterjets. In the ideal case, on the other hand, no constraints were imposed on the actuators, implying the heading and surge autopilots could allocate their desired control forces and moments without any restrictions on magnitude and delays. The more inadequate response with the realistic model could also be due to the lack of a feedforward term in the maneuvering controllers. Especially the heading controller will suffer from this, as the feedforward term contains valuable information regarding the curvature, and derivative of the curvature.

It is well known that a controller tracking a time-varying reference should include a feedforward term with the second derivative of the reference for optimal tracking. Without this term, the resulting heading response will be delayed as the PD controller can only react once an error from the desired reference has occurred. Hence, it is believed that the addition of a feedforward term in the heading controller would be beneficial for the tracking performance, and by extension, the path following abilities. However, this is not possible now, as it requires a reformulation of the maneuvering controllers to operate on generalized control forces and include a control allocation method for converting the desired control forces into waterjet demands, see Section 2.4 and Eek (2019) for more details.

Another impressive result from the simulation study is how well the NSB method performed in the case where the cable dynamics were included. Although the formation control method was designed for the case without any cable, it performed well under the additional disturbances the cable imposed on the system. It should be noted that the required turn radius during Section 5.3.2 increased somewhat from Section 5.2.2, but this is believed to be caused by the additional drag caused by the cable, not the formation control method itself.

When selecting the drag coefficients of the cable, they were only tuned to match the recorded loads in Section 3.5.2. Hence, other aspects with the transient response, such as minimum turning radius and time constants for (de)accelerations, of the cable was not considered. From this, it can be concluded that it is likely that the model does not display accurately in these aspects.

From discussing this matter with FFI, information has been received that they have been able to perform turns with a similar radius with the mine-sweep in real-life

experiments. Consequently, it is believed that the resulting cable model, with the drag coefficients from Section 3.5.2, displays characteristics with more drag than what is experienced by the real-life sweep. The increased drag characteristics will again have a considerable impact on the vessel's performance in a scenario, including a turn such as Section 5.3.2. Therefore, it is expected that better choices of drag coefficients will result in better performance in the simulations.

6 | Experiments

In this chapter, results from experiments at sea with the two vessels Odin and Frigg are presented. First, a short introduction to the experiments is presented. Then, the implementation of the NSB method, with the rest of the autonomous systems of Odin and Frigg are discussed. Next, a brief discussion is given on the required sensors for realizing the formation control method. Finally, the results from full-scale experiments with Odin and Frigg are presented.

6.1 Introduction

It is well known that results obtained through simulations do not automatically transfer to the real-works as a simulation model will always fail to fully capture the actual dynamics of a system. Hence, the theoretical work in Chapter 4 and the simulations in Chapter 5 are no guarantee that the NSB method will work as intended in the real-world.

To investigate if the NSB formation control method fulfills FFI's criteria for the mine-sweep application, full-scale field experiments with the two vessels Odin and Frigg was performed. The experiments were performed in FFI's designated test area for autonomous operations outside of Horten in May 2020.

Unfortunately, the experiments had to be performed without the actual sweep as they were unavailable at the moment due to maintenance. Nevertheless, the experiments will still be useful to investigate the performance in real-life. The vessels Odin and Frigg deployed during the autonomous experiments in this chapter are depicted in Fig. 6.1.



Figure 6.1: Photo of Odin and Frigg during the experiments. Courtesy of FFI.

6.2 Implementation

In order to perform the full-scale experiments, the formation control method presented in Chapter 4 had to be implemented and integrated into the existing software systems of Odin and Frigg. The existing autonomy pipeline for Odin and Frigg utilizes the Robot Operating System (ROS) framework as the underlying messaging system. ROS is an open-source software framework commonly used for autonomous robot applications. The basic principles of ROS are that each task is run in parallel as separate *nodes* that communicate over *topics*. The architecture of ROS allows for a modular architecture, which greatly simplifies the overall software complexity. The reader is referred to Stanford Artificial Intelligence Laboratory et al. (2018) for more details of ROS.

The control system itself is implemented as a standalone C++ library with no external dependencies except Eigen, an open-source linear algebra library, Guennebaud et al. (2010), to ensure re-usability, maintainability, and portability. The library was then included in a ROS wrapper to communicate with the rest of the autonomous system. By separating the control system implementation from ROS, it allows re-use of the same implementation, by merely writing another wrapper, if it is desirable to replace ROS with another framework in the future.

An interesting aspect with the NSB method, as presented in Chapter 4, is that it is designed as a centralized control system, which receives sensor measurements from both vessels and outputs the desired velocities of each vessel, see Fig. 4.1. However, for this particular application, it is desirable to have a decentralized system to avoid

external dependencies besides the two vessels. Thus, the desired references for each vessel should be calculated onboard each vessel.

In order to decentralize the control system, the choice was made to implement the same centralized system on both vessels, with the implication that both vessels calculate the desired NSB velocities for the whole system. The velocity for each vessel is then extracted and decomposed into the desired surge and heading references, see Fig. 6.2. By running the same implementation on both vessels, and extracting the desired velocity for each vessel, this will be equivalent to running a single centralized system, under the assumption that both vessels receive the same sensor measurements.

In the implementation, Odin was chosen as vessel one, with Frigg being vessel two. Hence, according to Section 4.4.2, the desired task function value for the formation task is specified in terms of the desired along-track and cross-track offset for Odin.

During the experiments, the existing autopilots of Odin and Frigg, developed and tuned by FFI, were used. For controlling the heading, a PD controller was used, while a PI controller was used for the surge.

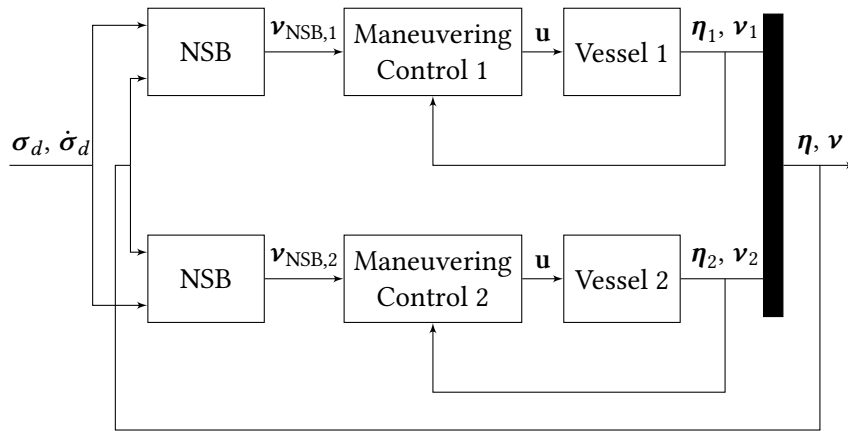


Figure 6.2: Overview of implemented decentralized NSB guidance system.

6.2.1 Available sensor measurements

The vessels Odin and Frigg are equipped with a great number of sensors for autonomous operation. The implementation relies on available measurements of the position and body-fixed velocities for both vessels. These measurements can easily be obtained through a Global Navigation Satellite System (GNSS) and an Inertial

Navigation System (INS). As it is common to be equipped with these sensors, the proposed NSB method should be realizable for most vessels.

The required sensor measurements are received from FFI's part of the autonomous system over ROS topics. The received position measurements are represented in a geographic coordinate system, by latitude, longitude, and elevation. Hence, they must be converted to local NED coordinates before they can be used in the NSB method. The conversion is done by using the first-order approximation of the WGS-85 ellipsoid given in Fossen and Perez (2004) and extracting the north and east positions. Further, the vessels' orientation in 6-DOF is represented using a quaternion. Hence, as only the 3-DOF representation is considered here, the vessels' heading is obtained by first converting the quaternion to Euler-angles, and then extracting the yaw angle.

Since both vessels run a decentralized version of the NSB method, each vessel must transmit its position and velocity to the other vessel periodically. Both vessels are equipped with a radio link, allowing inter-vessel communication between the autonomous systems on both vessels. During the experiments, the inter-vessel communication link was configured to transmit the position and velocity measurements at a frequency of 10 Hz. With a selected desired along-path surge speed of $u_d = 3$ m/s, this corresponds that each vessel will receive updated position and velocity measurements of the other vessel approximately every 30 cm on average.

6.3 Sweep

In this scenario, the vessels were set up to follow the same path as Section 5.3.2 and Section 5.2.2, which is close to what FFI expect an actual path would look like during a mine-sweep application. The vessels were loaded with the same NSB parameters as given in Section 5.2, except for the lookahead distance. Before performing the scenario presented here, several test runs were performed to tune the parameters. During the tuning process, it was discovered that the vessels could handle a lower lookahead distance than in the simulations without oscillations. The final choice of lookahead distance was therefore chosen as $\mu = 100$ m.

On the day of the experiments, it was forecasted wind on approximately 5 m/s from south-southeast. Furthermore, the sea level was relatively calm with almost no waves, as can be seen from Fig. 6.1. However, knowledge about the magnitude and direction of any potential ocean currents is unavailable, and therefore unknown. It should be noted that since the experiments were performed outdoors, knowledge about the environmental disturbances are not known in detail, implying the points

above are, at best, guesstimates of the actual environmental disturbances experienced during the experiments.

The resulting trajectories of Odin and Frigg, along with the barycenter trajectory is shown in Fig. 6.3. It can be observed that the vessels maintain the desired formation while following the path relatively well. However, a steady-state error on approximately 1 – 2 m can be observed for the cross-track error of the path following. Furthermore, it can be seen that both vessels are weathervaning with a non-zero sideslip angle towards the south. This is as expected as the steady-state error of the barycenter always is north of the desired path and due to the direction of the forecasted wind.

From Fig. 6.3 it can be seen that although the vessels manage to follow the first turn quite well, an overshoot is experienced during the last turn. The exact reason for this is unknown, but the tailwind could be a contributing factor, causing the vessels to not slow down the surge speed fast enough, causing the overshoot.

As the decentralized NSB method is running in parallel on both vessels, separate NSB errors for the three tasks are calculated online on each vessel. In the ideal case where both vessels have access to the same sensor measurements, the calculated errors from both vessels would be identical. However, as the position and velocity measurements are not shared continuously between the vessels, but rather at a frequency of 10 Hz, small differences in the calculated errors occur.

For completeness, the NSB errors for both vessels are included and can be seen in Fig. 6.4 and Fig. 6.5 for Odin and Frigg respectively. By comparing the two figures, it is clear that they are mostly similar. However, some differences can be observed for the calculated cross-track error for the formation task, where the errors calculate by Frigg are not centered about zero, unlike those from Odin.

The yaw, surge, and sway states of both vessels are given in Fig. 6.6. It can be seen from the detailed portion of the heading for both vessels that the yaw angle does not converge to the heading reference. Although it is not possible to conclude anything, it could be that this is the reason for the steady-state error experienced for the cross-track error of the barycenter task.

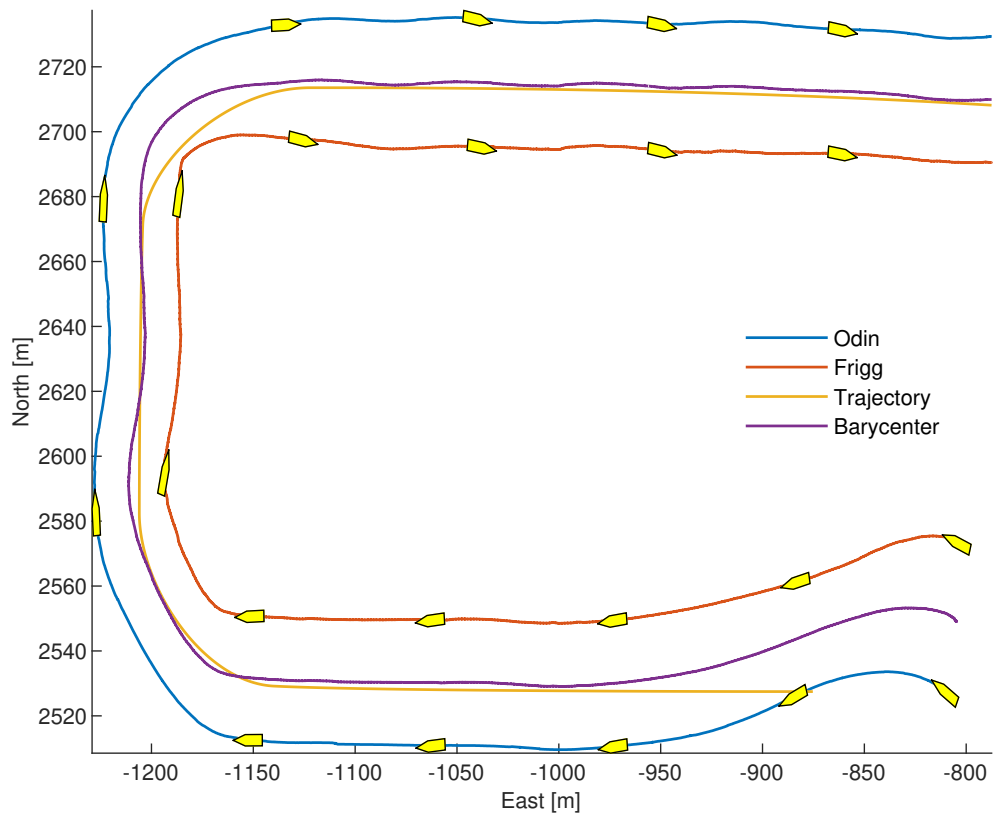


Figure 6.3: Path following of a path representing a mine-sweep.

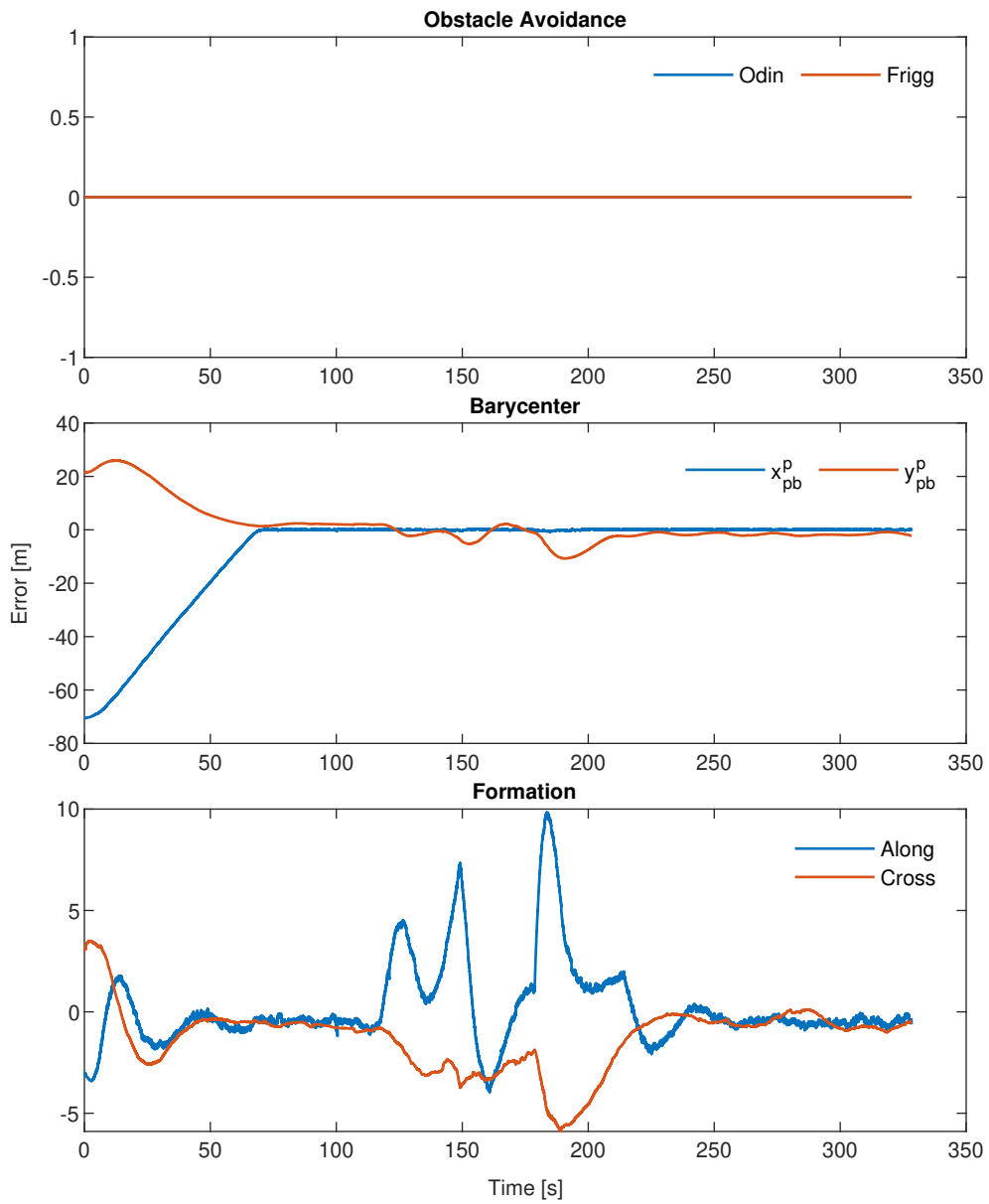


Figure 6.4: Online calculated NSB errors from Odin of a path representing a mine-sweep.

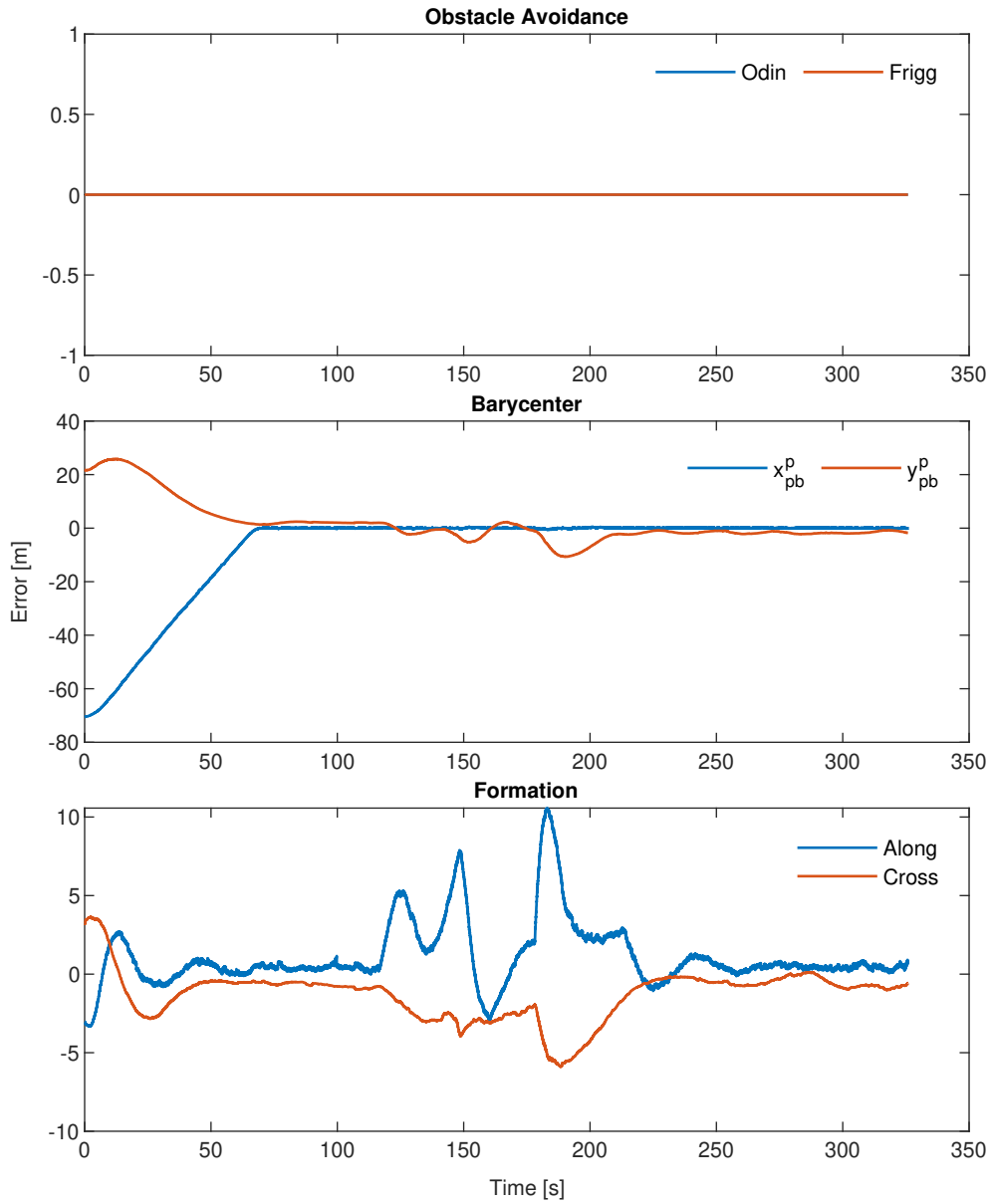


Figure 6.5: Online calculated NSB errors from Frigg of a path representing a mine-sweep.

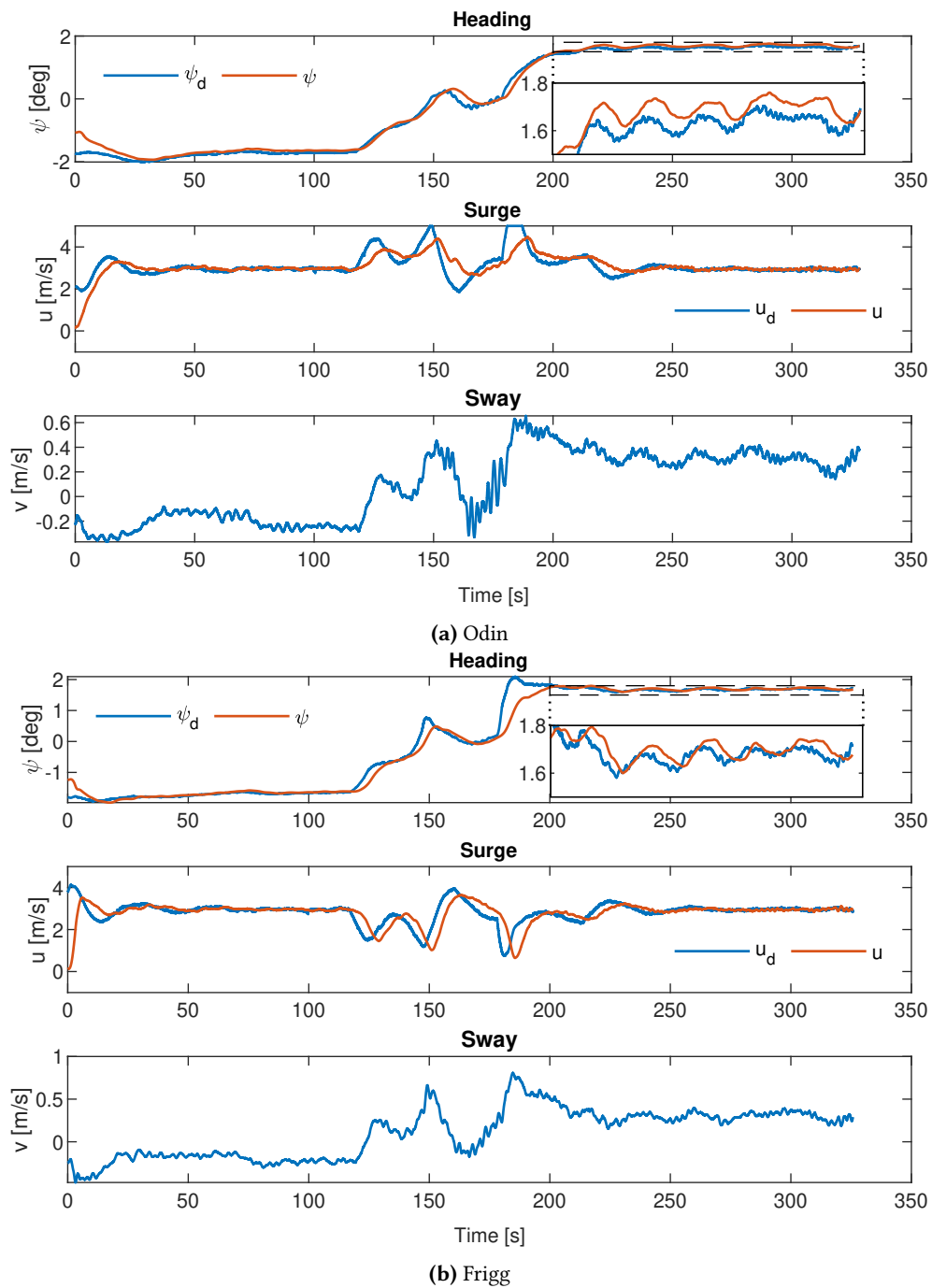


Figure 6.6: Desired vs. actual heading (top), surge (middle) and sway (bottom) of a path representing a mine-sweep.

6.4 Discussion

The most prominent part of the experimental results is the steady-state error for the cross-track barycenter error. The exact reasons for this steady-state error are unknown, but several potential factors have been identified. First, the wind, from the south-southeast, could be a contributing factor to the error, as the barycenter is always located on the north side of the desired path.

Another factor contributing to the steady-state error could be the lack of integral effects in the heading controller. In the detailed view of the top subplots in Fig. 6.6, it can be seen that the headings do not converge to their desired references. During the experiments, information was received from FFI that they are aware that the vessels, especially Odin, tends to drag towards starboard, which is verified by Fig. 6.6.

An interesting observation is that Odin was also used to perform the experimental results in Wiig et al. (2018), with the same PD controller. Here, the cross-track error converged toward zero without any steady-state error. The author of this thesis believes that the integral action in the ILOS guidance law compensated for the lack of an integral term in the heading autopilot. Hence, the failure of the heading controller's ability to track the reference entirely, was concealed by the integral action in the ILOS guidance law, making the cross-track error converge to zero nevertheless.

When comparing with the simulated scenarios, where the cross-track converged to zero, the heading autopilots used in Section 5.2 and Section 5.3 included an integral term. Furthermore, the PD controller used in the ideal case in Section 5.1 compensated for the ocean currents through the adaptive term.

To further investigate if the lack of integral action could be a contributing factor to the steady-state error, the scenario in Section 5.2.2 was repeated with a PD instead of PID controller for the heading. The resulting trajectories and NSB task errors are shown in Fig. 6.7 and Fig. 6.8 respectively. Interestingly, the cross-track error does not converge to zero, and a steady-state error can be seen, similar to what happened during the experiments. This is an indication that the lack of integral effect in the heading controllers on Odin and Frigg is a contributing factor to the steady-state cross-track error. It is, therefore, believed that changing to a PID controller for heading will increase the tracking capabilities of the heading reference, and improve the path following abilities of the barycenter task. Furthermore, it is believed that this will also improve the issue where both vessels have a tendency to drag towards starboard.

Regardless of the steady-state cross-track error, FFI has given indications that the experimental results are sufficient for the mine-sweep application. Therefore, it can be concluded that the full-scale experiments were successful.

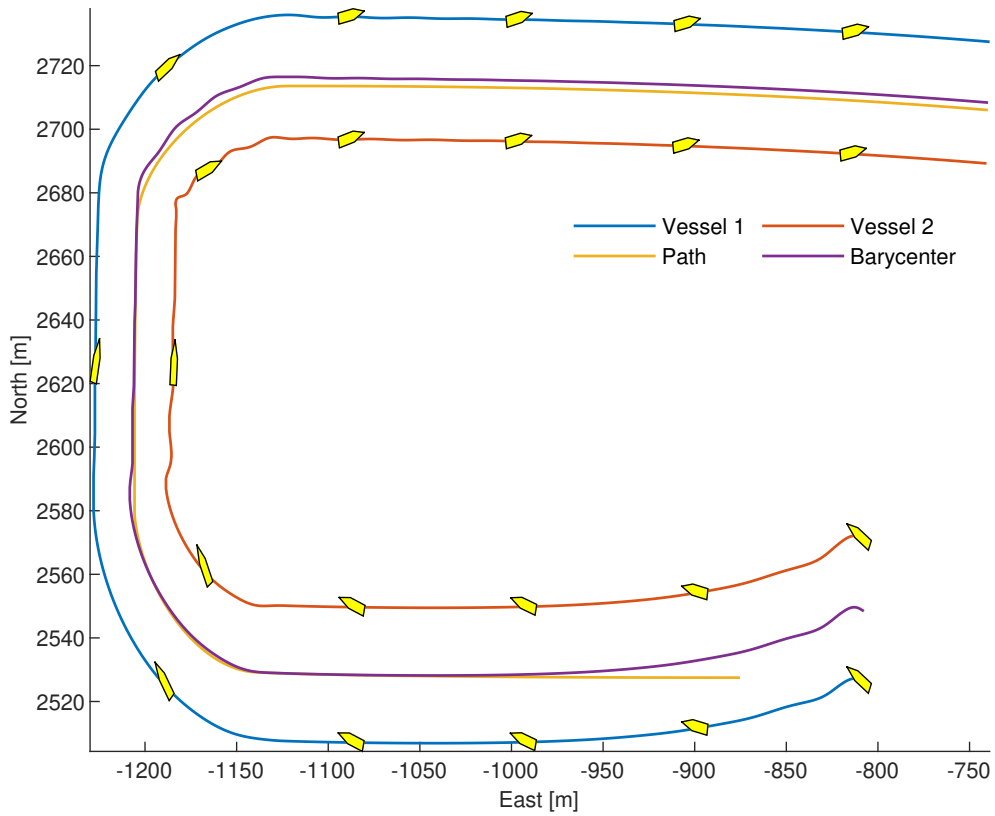


Figure 6.7: The simulated vessels and desired path with a PD-controller for heading

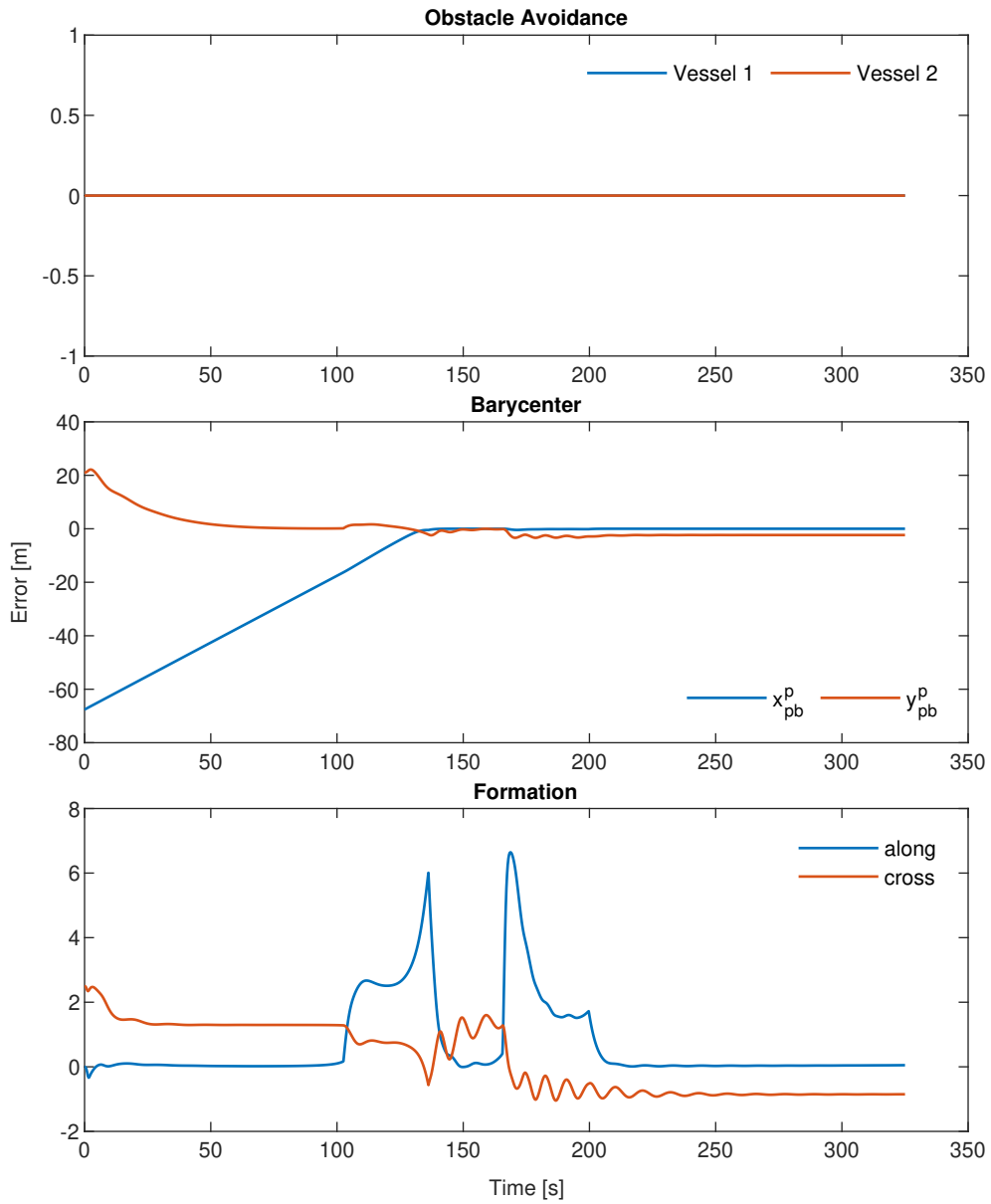


Figure 6.8: NSB errors with a PD-controller for heading

7 | Conclusion and Future Work

This chapter will conclude and suggest some further work based on the results and discussion presented in this thesis.

7.1 Conclusion

In this thesis, the topic of formation control of interconnected marine vessels was discussed. First, a mathematical model, based on Bhattacharya et al. (2011), describing the cable dynamics was proposed, with an improved hydrodynamic drag model for capturing the effects of ocean currents on the cable. The model was then verified against experimental data, which showed that it produces loads on the vessels within the same order of magnitude to experimental data.

Next, a behavioral method based on the null-space projection was designed, and a novel approach for the barycenter task, inspired by LOS methods, was proposed. Furthermore, a stability analysis of the closed-loop systems for the individual tasks, with the vessel model from Moe et al. (2016) was performed. The closed-loop error dynamics of the formation task was proven UGES, while USGES was established for the barycenter task, which is the best that can be achieved for LOS methods due to the kinematic representation, which introduces saturation through the trigonometric functions.

Then, the NSB method was implemented in MATLAB/Simulink. Through several simulation studies, the performance of the formation control method was investigated. First, the system was simulated with the vessel model and controllers from Moe et al. (2016) to illustrate the theoretical results, with great success. When only the barycenter is active, the task errors converge to zero, as expected from the theoretical results, while small errors are experienced for the along-track formation task errors when all tasks are active. Then, simulations were performed with the more realistic vessel model, both with and without the cable attached. The results were somewhat worse than in the ideal case, due to constraints not included in the vessel model

from Moe et al. (2016). In the case with the cable, the minimum turning radius of the interconnected vessels increased, but it is believed this is caused by improper tuning of the cable parameters as only experimental data on the loads was available. Nevertheless, similar results were obtained for both with and without the cable, suggesting the NSB methods manage to perform well when disturbed by the cable dynamics.

Finally, the NSB method was implemented in C++ and integrated into the existing autonomous systems of Odin and Frigg through a ROS interface. It was then verified through full-scale experiments at sea with Odin and Frigg, which gave promising results. Although a steady-state error was experienced for the barycenter task's cross-track error, it is believed to be caused by the lack of integral action in the heading controllers used on Odin and Frigg, not by the NSB method itself. Unfortunately, experiments with the sweep were not possible, as they were not available at the time. Nevertheless, due to the promising results, indications have been received from FFI that further experiments of the NSB method, with the sweep, are planned later.

7.2 Further work

In this section, suggestions to further work is presented. It should be noted that the proposals are not listed in prioritized order.

- **Improve drag coefficients:** To improve the transient response of the cable, better parameter estimation should be performed for the drag coefficients. Better drag coefficients will likely enhance the transient response of the cable, e.g., through turns, giving more accurate and realistic results in simulations.
- **Investigate robustness properties:** More thorough investigations of the closed-loop system of the barycenter task, Lemma 4.7, should be performed to quantify the upper bound of the disturbance's magnitude. One possibility could be to follow the approach of (Wiig et al.; 2018, Theorem 2) and show that the total system, including the disturbance, is UGAS, and therefore bounded. However, this requires to show that the interconnection term from the disturbance satisfies (Loría and Panteley; 2005, Assumption 4), which could be difficult.
- **Lookahead independent of cross-track error:** In the proof of Lemma 4.3, it was shown that the lookahead distance (4.38) could be chosen independently of the cross-track error. Removing the cross-track error from (4.38) could lead

to faster convergence of the cross-track error as the lookahead distance will be smaller, giving more rapid steering towards the desired path.

- **Avoid collision with the cable:** At the moment, NSB is unaware of where the cable is, and could, in theory, output desired references causing the vessels to collide, or run over, the cable. If the vessels, and cable/sweep, are positioned "nicely" initially, the possibility of this happening is believed to be small. Nevertheless, it could still be nice to investigate this further from an integrity point of view.
- **Investigate other formation control methods such as LOS:** Other formation control methods than NSB does also exist. An attempt to combine the LOS method for curved paths in Belleter et al. (2019) with Belleter and Pettersen (2014) to create a LOS formation control method for curved paths was made during this thesis. Due to the limited time scope, it was not possible to conclude the analysis of the closed-loop stability properties, and the work related to this method is thus not included in the thesis. However, simulation results look promising, and the method should be investigated further.
- **Investigate the possibility of using predictive methods such as MPC:** Within the field of formation control, most of the research has been focused on reactive methods. However, it was seen in both the simulation and experimental results that the vessels were not able to follow the desired path correctly throughout turns. Here, a predictive method such as MPC could be useful as the vessels' trajectories through the turns could be predicted, making it possible to generate surge and heading references, which could result in better performance than in reactive approaches.
- **Add integral action in the heading controllers of Odin and Frigg:** As discussed in Section 6.4, the addition of integral action in the heading controllers would likely decrease, or remove, the steady-state error in the cross-track error for the barycenter task. Although this is not a must, it should be considered if a better path following is desired.
- **Better tuning of the NSB parameters:** Due to limited time during the experiments, better performance can likely be achieved by spending some more time tuning the NSB parameters.
- **Experiments with sweep:** To evaluate the performance of the NSB method

for the intended mine-sweep application, experiments should be performed with the sweep.

References

- Angeli, D. and Sontag, E. D. (1999). Forward completeness, unboundedness observability, and their lyapunov characterizations, *Systems & Control Letters* **38**(4-5): 209–217.
- Antonelli, G., Arrichiello, F. and Chiaverini, S. (2005). EXPERIMENTAL KINEMATIC COMPARISON OF BEHAVIORAL APPROACHES FOR MOBILE ROBOTS, *IFAC Proceedings Volumes* **38**(1): 295–300.
- Antonelli, G., Arrichiello, F. and Chiaverini, S. (2008). Stability analysis for the null-space-based behavioral control for multi-robot systems, *2008 47th IEEE Conference on Decision and Control*, IEEE.
- Antonelli, G. and Chiaverini, S. (2003). Kinematic control of a platoon of autonomous vehicles, *2003 IEEE International Conference on Robotics and Automation (Cat. No.03CH37422)*, IEEE.
- Antonelli, G. and Chiaverini, S. (2006). Kinematic control of platoons of autonomous vehicles, *IEEE Transactions on Robotics* **22**(6): 1285–1292.
- Arkin, R. C. (1989). Motor schema – based mobile robot navigation, *The International Journal of Robotics Research* **8**(4): 92–112.
- Arrichiello, F. (2006). *Coordination Control of Multiple Mobile Robots*, PhD thesis, UNIVERSITA DEGLI STUDI DI CASSINO.
- Arrichiello, F., Chiaverini, S. and Fossen, T. (2006a). *Formation Control of Marine Surface Vessels Using the Null-Space-Based Behavioral Control*, Springer Berlin Heidelberg, Berlin, Heidelberg, pp. 1–19.
- Arrichiello, F., Chiaverini, S. and Fossen, T. (2006b). Formation control of underactuated surface vessels using the null-space-based behavioral control, *2006 IEEE/RSJ International Conference on Intelligent Robots and Systems*, IEEE.

- Arrichiello, F., Heidarsson, H., Chiaverini, S. and Sukhatme, G. S. (2010). Cooperative caging using autonomous aquatic surface vehicles, *2010 IEEE International Conference on Robotics and Automation*, IEEE.
- Arrichiello, F., Heidarsson, H. K., Chiaverini, S. and Sukhatme, G. S. (2011). Cooperative caging and transport using autonomous aquatic surface vehicles, *Intelligent Service Robotics* **5**(1): 73–87.
- Arrichiello, F., Sarkar, S., Chiaverini, S. and Antonelli, G. (2018). Dynamic modelling of a streamer of hydrophones towed with an autonomous underwater vehicle, *Modelling and Simulation for Autonomous Systems*, Springer International Publishing, pp. 179–192.
- Balch, T. and Arkin, R. (1998). Behavior-based formation control for multirobot teams, *IEEE Transactions on Robotics and Automation* **14**(6): 926–939.
- Belleter, D. J. (2016). *Control of Underactuated Marine Vehicles in the Presence of Environmental Disturbances*, PhD thesis, NTNU.
- Belleter, D. J. W., Maghenem, M., Paliotta, C. and Pettersen, K. Y. (2018). Observer based path following for underactuated marine vessels in the presence of ocean currents: A global approach - with proofs, *CoRR* **abs/1810.06974**.
- Belleter, D., Maghenem, M. A., Paliotta, C. and Pettersen, K. Y. (2019). Observer based path following for underactuated marine vessels in the presence of ocean currents: A global approach, *Automatica* **100**: 123–134.
- Belleter, D. and Pettersen, K. (2014). Path following for formations of underactuated marine vessels under influence of constant ocean currents, *53rd IEEE Conference on Decision and Control*, IEEE.
- Bhattacharya, S. (2020a). Un-documented code for Cooperative control of autonomous surface vehicles for oil skimming and cleanup. <http://www.subhrajit.net/files/Projects-Work/OilBoom{ }Catenary{ }2010/icra2011{ }codes.zip>.
- Bhattacharya, S. (2020b). Web page, Subhrajit Bhattacharya, Lehigh University. <https://www.lehigh.edu/~sub216/publications>.
- Bhattacharya, S., Heidarsson, H., Sukhatme, G. S. and Kumar, V. (2011). Cooperative control of autonomous surface vehicles for oil skimming and cleanup, *2011 IEEE International Conference on Robotics and Automation*, IEEE.

- Børhaug, E., Pavlov, A., Panteley, E. and Pettersen, K. Y. (2011). Straight line path following for formations of underactuated marine surface vessels, *IEEE Transactions on Control Systems Technology* **19**(3): 493–506.
- Børhaug, E., Pavlov, A. and Pettersen, K. Y. (2006). Cross-track formation control of underactuated surface vessels, *Proceedings of the 45th IEEE Conference on Decision and Control*, IEEE.
- Børhaug, E., Pavlov, A. and Pettersen, K. Y. (2008). Integral LOS control for path following of underactuated marine surface vessels in the presence of constant ocean currents, *2008 47th IEEE Conference on Decision and Control*, IEEE.
- Breivik, M., Hovstein, V. E. and Fossen, T. I. (2008). Ship formation control: A guided leader-follower approach, *IFAC Proceedings Volumes* **41**(2): 16008–16014.
- Brooks, R. (1986). A robust layered control system for a mobile robot, *IEEE Journal on Robotics and Automation* **2**(1): 14–23.
- Caharija, W., Candeloro, M., Pettersen, K. Y. and Sørensen, A. J. (2012). Relative velocity control and integral LOS for path following of underactuated surface vessels, *IFAC Proceedings Volumes* **45**(27): 380–385.
- Dubins, L. E. (1957). On curves of minimal length with a constraint on average curvature, and with prescribed initial and terminal positions and tangents, *American Journal of Mathematics* **79**(3): 497–516.
- Eek, Å. (2019). Formation control of underactuated surface vessels in the presence of ocean currents. Unpublished, TTK4550 - specialization project.
- Egeland, O. and Gravdahl, J. (2002). *Modeling and Simulation for Automatic Control*, Marine Cybernetics.
- Fossen, T. I. (2011). *Handbook of Marine Craft Hydrodynamics and Motion Control*, John Wiley & Sons, Ltd.
- Fossen, T. I. and Perez, T. (2004). Marine systems simulator (mss).
URL: <https://github.com/cybergalactic/MSS>
- Fossen, T. I. and Pettersen, K. Y. (2014). On uniform semiglobal exponential stability (USGES) of proportional line-of-sight guidance laws, *Automatica* **50**(11): 2912–2917.

- Fredriksen, E. and Pettersen, K. Y. (2006). Global κ -exponential way-point maneuvering of ships: Theory and experiments, *Automatica* **42**(4): 677 – 687.
- Fritsch, F. N. and Carlson, R. E. (1980). Monotone piecewise cubic interpolation, *SIAM Journal on Numerical Analysis* **17**(2): 238–246.
- Gerdt, M. (2015). *A Survey on Optimal Control Problems with Differential-Algebraic Equations*, Springer International Publishing, Cham, pp. 103–161.
- Giron-Sierra, J. M., Gheorghita, A. T., Angulo, G. and Jimenez, J. F. (2014). Towing a boom with two USVs for oil spill recovery: Scaled experimental development, *2014 13th International Conference on Control Automation Robotics & Vision (ICARCV)*, IEEE.
- Giron-Sierra, J. M., Gheorghita, A. T. and Jimenez, J. F. (2015). Fully automatic boom towing by unmanned ships: Experimental study, *OCEANS 2015 - MTS/IEEE Washington*, IEEE.
- Guennebaud, G., Jacob, B. et al. (2010). Eigen v3, <http://eigen.tuxfamily.org>.
- Ihle, I.-A. F., Arcak, M. and Fossen, T. I. (2006). Passivity-based designs for synchronized path following, *Proceedings of the 45th IEEE Conference on Decision and Control*, IEEE.
- Ihle, I.-A., Jouffroy, J. and Fossen, T. (2006). *Robust Formation Control of Marine Craft Using Lagrange Multipliers*, Springer Berlin Heidelberg, Berlin, Heidelberg, pp. 113–129.
- Iwata, S., Oki, T. and Takamatsu, M. (2019). Index reduction for differential-algebraic equations with mixed matrices, *Journal of the ACM* **66**(5): 1–34.
- Jimenez, J. (2016). Notes on the development of a model for spill boom towing.
- Jimenez, J. and Giron-Sierra, J. M. (2018). MODELLING THE AUTOMATIC DEPLOYMENT OF OIL-SPILL BOOMS: A SIMULATION SCENARIO FOR SEA CLEANING, *2018 Winter Simulation Conference (WSC)*, IEEE.
- Jiménez, J. L., Hernández, G., Campos, I. and Del-Valle, G. (2005). Newtonian and canonical analysis of the motion of a rope falling from a table, *European Journal of Physics* **26**(6): 1127–1137.
- Johansen, V. (2007). *Modelling of flexible slender systems for real-time simulation and control applications*, PhD thesis, NTNU.

- Khalil, H. K. (2002). *Nonlinear systems; 3rd ed.*, Prentice-Hall, Upper Saddle River, NJ.
- Kheiri, M., Païdoussis, M. and Amabili, M. (2013). A nonlinear model for a towed flexible cylinder, *Journal of Sound and Vibration* **332**(7): 1789–1806.
- Kyrkjebø, E. (2007). *Motion Coordination of Mechanical Systems: Leader-Follower Synchronization of Euler-Lagrange Systems using Output Feedback Control*, PhD thesis, NTNU.
- Lapierre, L. and Soetanto, D. (2007). Nonlinear path-following control of an AUV, *Ocean Engineering* **34**(11-12): 1734–1744.
- Lapierre, L., Soetanto, D. and Pascoal, A. (2003). Coordinated motion control of marine robots, *IFAC Proceedings Volumes* **36**(21): 217–222.
- Loría, A. and Panteley, E. (2005). 2 cascaded nonlinear time-varying systems: Analysis and design, *Advanced Topics in Control Systems Theory*, Springer London, pp. 23–64.
- Markaroglu, H., Guzelkaya, M., Eksin, I. and Yesil, E. (2006). Tracking time adjustment in back calculation anti-windup scheme, *ECMS 2006 Proceedings edited by: W. Borutzky, A. Orsoni, R. Zobel*, ECMS.
- Midtgaard, Ø. and Nakjem, M. (2016). Unmanned systems for stand-off underwater mine hunting, *Proceedings of the Undersea Defence Technology Conference (UDT) Europe 2016*.
- Moe, S., Pettersen, K. Y., Fossen, T. I. and Gravdahl, J. T. (2016). Line-of-sight curved path following for underactuated USVs and AUVs in the horizontal plane under the influence of ocean currents, *2016 24th Mediterranean Conference on Control and Automation (MED)*, IEEE.
- Pereda, F. J., de Marina, H. G., Giron-Sierra, J. M. and Jimenez, J. (2011). Towards automatic oil spill confinement with autonomous marine surface vehicles, *OCEANS 2011 IEEE - Spain*, IEEE.
- Pettersen, K. Y. (2017). Lyapunov sufficient conditions for uniform semiglobal exponential stability, *Automatica* **78**: 97–102.
- Shmoylova, E., Gerhard, J., Postman, E. and Roche, A. (2013). Simplification of differential algebraic equations by the projection method, *EOOLT*.
- Skjetne, R., Moi, S. and Fossen, T. (2002). Nonlinear formation control of marine craft, *Proceedings of the 41st IEEE Conference on Decision and Control, 2002.*, IEEE.

Stanford Artificial Intelligence Laboratory et al. (2018). Robotic operating system.

URL: <https://www.ros.org>

The Mathworks, I. (2020a). Solve differential algebraic equations (DAEs). <https://se.mathworks.com/help/matlab/math/solve-differential-algebraic-equations-daes.html>.

The MathWorks, I. (2020b). *Symbolic Math Toolbox*. <https://www.mathworks.com/help/symbolic>.

Wiig, M. S., Pettersen, K. Y., Ruud, E.-L. M. and Krogstad, T. R. (2018). An integral line-of-sight guidance law with a speed-dependent lookahead distance, *2018 European Control Conference (ECC)*, IEEE.

Wolfram Research, I. (2020). Wolfram language. <https://www.wolfram.com/language>.

Appendices

A | Stability proofs

The following appendix contains the proofs of Lemmas 4.2–4.4. To improve the readability, the proofs are left out from the main text, and instead included here.

A.1 Proof of Lemma 4.2

The proof follows along the lines of (Belleter et al.; 2018, Lemma 1).

First, as the closed-loop system of Eqs. (4.76b)–(4.76d) is UGES by Proposition 4.4, they are trivially forward complete.

Next, as the vector $[\tilde{X}_{2,i}^T \ \kappa(\theta) \ u_{d,i} \ \dot{u}_{d,i} \ u_c \ v_c]^T$ is bounded, there exist some scalar $\beta_0 \in \mathbb{R}_{>0}$ such that $\|[\tilde{X}_{2,i}^T \ \kappa(\theta) \ u_{d,i} \ \dot{u}_{d,i} \ u_c \ v_c]^T\| \leq \beta_0$. Furthermore, from (4.74) it can be concluded the existence of some positive functions $a_{r_d}(\cdot)$ and $b_{r_d}(\cdot)$ such that

$$|r_d(\cdot)| \leq a_{r_d}(\mu, \beta_0)|v| + b_{r_d}(\mu, \beta_0) \quad (\text{A.1})$$

Then, choosing the LFC, omitting subscripts for simplicity

$$V_1(v) = \frac{1}{2}v^2 \quad (\text{A.2})$$

whose time derivative along the solutions of (4.76e) is

$$\begin{aligned} \dot{V}_1(v) &= X(u_d + \tilde{u}, u_c)r_d v + X(u_d + \tilde{u}, u_c)\tilde{r}v \\ &\quad + Y(u_d + \tilde{u}, u_c)v^2 - Y(u_d + \tilde{u}, u_c)v_c v \end{aligned} \quad (\text{A.3})$$

Using Young's inequality, it can be shown that the following bound holds for $\dot{V}_1(v)$

$$\begin{aligned} \dot{V}_1(v) &\leq Y(u_d + \tilde{u}, u_c)v^2 \\ &\quad + X(u_d + \tilde{u}, u_c)(\tilde{r}^2 + v^2) \\ &\quad + X(u_d + \tilde{u}, u_c)(r_d^2 + v^2) \end{aligned}$$

$$- Y(u_d + \tilde{u}, u_c)(v_c^2 + v^2) \quad (\text{A.4})$$

$$\leq \alpha V + \beta \quad (\text{A.5})$$

where $\alpha \in \mathbb{R}_{\geq 0}$, $\beta \in \mathbb{R}_{\geq 0}$ are positive scalars. As (A.5) is scalar, the comparison lemma (Khalil; 2002, Lemma 3.4) may be used to bound the solutions of (A.5) by the scalar linear system

$$\dot{x} = \alpha x + \beta \quad (\text{A.6})$$

whose solution is equal to

$$x(t) = \frac{\|x(t_0)\| \alpha + \beta}{\alpha} e^{\alpha(t-t_0)} - \frac{\beta}{\alpha}. \quad (\text{A.7})$$

Hence, by the comparison lemma, the solutions of (A.5) must be upper bounded by

$$V_1(v) \leq \frac{\|x(t_0)\| \alpha + \beta}{\alpha} e^{\alpha(t-t_0)} - \frac{\beta}{\alpha}. \quad (\text{A.8})$$

As $V(v)$ is defined for all t up to $t_{\max} = \infty$, it follows that v must also be defined up to $t_{\max} = \infty$. In the same way as Belleter et al. (2018), the solutions of (4.76e) thus fulfills the definition of forward completeness in Angeli and Sontag (1999) and forward completeness of the solution of (4.76e) can be concluded.

Having established forward completeness of Eqs. (4.76b)–(4.76e), only the forward completeness of (4.76a) remains before forward completeness may be concluded for the whole closed-loop system (4.76). To show forward completeness of the along- and cross-track error dynamics, consider the LFC

$$V_2 = \frac{1}{2} \left(x_{pb}^p \right)^2 + \frac{1}{2} \left(y_{pb}^p \right)^2, \quad (\text{A.9})$$

whose derivative along the solutions of (4.76a) is

$$\dot{V}_2 = -k_\theta \frac{\left(x_{pb}^p \right)^2}{\sqrt{1 + \left(x_{pb}^p \right)^2}} - \frac{1}{2} (U_{d,1} + U_{d,2}) \frac{\left(y_{pb}^p \right)^2}{\sqrt{\Delta^2 + \left(y_{pb}^p \right)^2}} + G_1(\cdot) y_{pb}^p \quad (\text{A.10})$$

$$\leq G_1(\cdot) y_{pb}^p + \left(x_{pb}^p \right)^2 \quad (\text{A.11})$$

Using Young's inequality, along with the bounds on $G_1(\cdot)$ from (4.44) the following bound is obtained

$$\dot{V}_2 \leq V_2 + \frac{1}{2} \zeta_1^2 (U_{d,1}, U_{d,2}) \left\| \begin{bmatrix} \tilde{\psi}_1 & \tilde{u}_1 & \tilde{\psi}_2 & \tilde{u}_2 \end{bmatrix}^T \right\|^2 \quad (\text{A.12})$$

$$\leq V_2 + \sigma_2 \left(v_1, v_2, \tilde{\psi}_1, \tilde{u}_1, \tilde{\psi}_2, \tilde{u}_2 \right), \quad (\text{A.13})$$

where $\sigma_2(\cdot) \in \mathcal{K}_\infty$. By viewing the arguments of $\sigma_2(\cdot)$ as inputs to the along- and cross-track error dynamics, (Angeli and Sontag; 1999, Corollary 2.11) is satisfied by (A.12) and forward completeness of the solutions of (4.76a) can be concluded. Similarly to Belleter et al. (2018), the arguments of $\sigma_2(\cdot)$ are all forward complete, and are therefore valid input signals according to Angeli and Sontag (1999). Forward completeness for the whole closed-loop system (4.76) is therefore established, and the proof of Lemma 4.2 is complete.

A.2 Proof of Lemma 4.3

This proof follows along the lines of (Belleter et al.; 2018, Lemma 2).

Recall the sway dynamics (4.76e):

$$\begin{aligned} \dot{v}_i &= X(u_{d,i} + \tilde{u}_i, u_c)r_{d,i} + X(u_{d,i} + \tilde{u}_i, u_c)\tilde{r}_i \\ &+ Y(u_{d,i} + \tilde{u}_i, u_c)v_i - Y(u_{d,i} + \tilde{u}_i, u_c)v_c. \end{aligned} \quad (\text{A.14})$$

Considering the following Lyapunov function candidate $V(v_i) = \frac{1}{2}v_i^2$, whose time derivative along the solutions of (4.76e) is

$$\begin{aligned} \dot{V} &= v_i\dot{v}_i = X(u_{d,i} + \tilde{u}_i, u_c)r_{d,i}v_i + X(u_{d,i} + \tilde{u}_i, u_c)\tilde{r}_i v_i \\ &+ Y(u_{d,i} + \tilde{u}_i, u_c)v_i^2 - Y(u_{d,i} + \tilde{u}_i, u_c)v_c v_i \end{aligned} \quad (\text{A.15})$$

$$\begin{aligned} &\leq X(u_{d,i}, u_c)r_{d,i}v_i + a_x\tilde{u}_i r_{d,i}v_i + X(u_{d,i}, u_c)\tilde{r}_i v_i + a_x\tilde{u}_i\tilde{r}_i v_i \\ &+ Y(u_{d,i}, u_c)v_i^2 + a_y\tilde{u}_i v_i^2 - Y(u_{d,i}, u_c)v_c v_i - a_y\tilde{u}_i v_c v_i, \end{aligned} \quad (\text{A.16})$$

where the following fact, which can be concluded to hold for $X(u, u_c)$ and $Y(u, u_c)$ from Eqs. (C.2)–(C.3) is used:

$$X(u, u_c) = a_x u + b_x u_c + c_x \quad (\text{A.17})$$

$$Y(u, u_c) = a_y u + b_y u_c + c_y. \quad (\text{A.18})$$

Next, consider the term $r_{d,i}v_i$ using the expression for r_d in (4.74), omitting subscripts for simplicity

$$r_d v = \kappa(\theta)\dot{\theta}v + \frac{\dot{u}_d}{u_d^2 + v^2}v^2 - \frac{u_d\dot{v}v}{u_d^2 + v^2}$$

$$\begin{aligned}
& - \frac{v}{\Delta^2 + (y_{pb}^p)^2} \left[\Delta \dot{y}_{pb}^p - y_{pb}^p \left(\frac{\partial \Delta}{\partial x_{pb}^p} \dot{x}_{pb}^p + \frac{\partial \Delta}{\partial y_{pb}^p} \dot{y}_{pb}^p \right) \right] \quad (\text{A.19}) \\
& = \kappa(\theta) v \left(\frac{1}{2} U_1 \cos(\chi_1 - \gamma_p) + \frac{1}{2} U_2 \cos(\chi_2 - \gamma_p) + \frac{k_\theta x_{pb}^p}{\sqrt{1 + (x_{pb}^p)^2}} \right) \\
& \quad + \frac{\dot{u}_d}{u_d^2 + v^2} v^2 - \frac{u_d v}{u_d^2 + v^2} (X(u, u_c) r + Y(u, u_c) v - Y(u, u_c) v_c) \\
& \quad - \frac{\Delta v}{\Delta^2 + (y_{pb}^p)^2} \left(-\frac{1}{2} (U_{d,1} + U_{d,2}) \frac{y_{pb}^p}{\sqrt{\Delta^2 + (y_{pb}^p)^2}} - \kappa(\theta) \dot{\theta} x_{pb}^p + G_1(\cdot) \right) \\
& \quad + \frac{y_{pb}^p v}{\Delta^2 + (y_{pb}^p)^2} \left[\frac{\partial \Delta}{\partial x_{pb}^p} \left(-\frac{k_\theta x_{pb}^p}{\sqrt{1 + (x_{pb}^p)^2}} + \dot{\theta} \kappa(\theta) y_{pb}^p \right) \right. \\
& \quad \left. + \frac{\partial \Delta}{\partial y_{pb}^p} \left(-\frac{1}{2} (U_{d,1} + U_{d,2}) \frac{y_{pb}^p}{\sqrt{\Delta^2 + (y_{pb}^p)^2}} - \kappa(\theta) \dot{\theta} x_{pb}^p + G_1(\cdot) \right) \right]. \quad (\text{A.20})
\end{aligned}$$

Now, introduce a term $F(\tilde{\mathbf{X}}_1, \tilde{\mathbf{X}}_2, \Delta, \theta, u_d, \dot{u}_d, v, v_c, u_c, r)$ to collect all terms that grows linearly with v and the terms that grow quadratically with v but vanish when $\tilde{\mathbf{X}}_1$ and $\tilde{\mathbf{X}}_2$ are zero:

$$\begin{aligned}
r_d v & = v \left[1 + \frac{\Delta x_{pb}^p}{\Delta^2 + (y_{pb}^p)^2} \right] \kappa(\theta) \left(\frac{1}{2} U_1 \cos(\chi_1 - \gamma_p) + \frac{1}{2} U_2 \cos(\chi_2 - \gamma_p) \right) \\
& \quad - \frac{u_d}{u_d^2 + v^2} Y(u, u_c) v^2 + F(\tilde{\mathbf{X}}_1, \tilde{\mathbf{X}}_2, \Delta, \theta, u_d, \dot{u}_d, v, v_c, u_c, r), \quad (\text{A.21})
\end{aligned}$$

where the expression for $\dot{\theta}$ has been inserted in the second last term on the third line in (A.20) to extract the second term in the first parenthesis on the first line of (A.21)

and $F(\cdot)$ is given by

$$\begin{aligned}
F(\cdot) = v & \left[\kappa(\theta) \frac{k_\theta x_{pb}^p}{\sqrt{1 + (x_{pb}^p)^2}} + \frac{\dot{u}_d}{u_d^2 + v^2} v^2 - \frac{u_d v}{u_d^2 + v^2} (X(u, u_c)r - Y(u, u_c)v_c) \right. \\
& - \frac{\Delta}{\Delta^2 + (y_{pb}^p)^2} \left(-\frac{1}{2} (U_{d,1} + U_{d,2}) \frac{y_{pb}^p}{\sqrt{\Delta^2 + (y_{pb}^p)^2}} - \kappa(\theta) \frac{k_\theta (x_{pb}^p)^2}{\sqrt{1 + (x_{pb}^p)^2}} + G_1(\cdot) \right) \\
& - \frac{y_{pb}^p v}{\Delta^2 + (y_{pb}^p)^2} \left[\frac{\partial \Delta}{\partial x_{pb}^p} \frac{k_\theta x_{pb}^p}{\sqrt{1 + (x_{pb}^p)^2}} \right. \\
& \left. \left. + \frac{\partial \Delta}{\partial y_{pb}^p} \left(-\frac{1}{2} (U_{d,1} + U_{d,2}) \frac{y_{pb}^p}{\sqrt{\Delta^2 + (y_{pb}^p)^2}} + G_1(\cdot) \right) \right] \right]. \tag{A.22}
\end{aligned}$$

Observe how all terms with partial derivatives of Δ and $\dot{\theta}$ are cancelled due to skew-symmetry from the definition of the lookahead distance (4.38)

$$\begin{aligned}
& \frac{\Delta}{x_{pb}^p} \dot{\theta} \kappa(\theta) y_{pb}^p - \frac{\Delta}{y_{pb}^p} \dot{\theta} \kappa(\theta) x_{pb}^p = \\
& = \frac{x_{pb}^p}{\sqrt{1 + (x_{pb}^p)^2 + (y_{pb}^p)^2}} \dot{\theta} \kappa(\theta) y_{pb}^p - \frac{y_{pb}^p}{\sqrt{1 + (x_{pb}^p)^2 + (y_{pb}^p)^2}} \dot{\theta} \kappa(\theta) x_{pb}^p = 0. \tag{A.23}
\end{aligned}$$

Furthermore, from (A.22) it can be seen that the function $F(\cdot)$ may be upper bounded by the following inequality

$$|F(\cdot)| \leq F_2(\tilde{\mathbf{X}}_1, \tilde{\mathbf{X}}_2, \Delta, \theta, u_d, \dot{u}_d, v, v_c, u_c, r) v^2 + F_1(\tilde{\mathbf{X}}_1, \tilde{\mathbf{X}}_2, \Delta, \theta, u_d, \dot{u}_d, v, v_c, u_c, r) |v|, \tag{A.24}$$

where $F_{1,2}(\cdot)$ are positive functions with

$$F_2(\mathbf{0}, \mathbf{0}, \Delta, \theta, u_d, \dot{u}_d, v, v_c, u_c, r) = 0. \tag{A.25}$$

Consequently, the term $r_d v$ may be upper bounded as

$$r_{d,i} v_i \leq |v_i| \left[\left| 1 + \frac{\Delta x_{pb}^p}{\Delta^2 + (y_{pb}^p)^2} \right| |\kappa(\theta)| \frac{1}{2} (|U_i| + |U_j|) + |F(\cdot)| - \frac{u_{d,i}}{u_{d,i}^2 + v_i^2} Y(u_i, u_c) v_i^2 \right] \quad (\text{A.26})$$

$$\leq |v_i| \left[\left| 1 + \frac{\Delta x_{pb}^p}{\Delta^2 + (y_{pb}^p)^2} \right| |\kappa(\theta)| \frac{1}{2} (|u_i| + |v_i| + |u_j| + |v_j|) + |F(\cdot)| - \frac{u_{d,i}}{u_{d,i}^2 + v_i^2} Y(u_i, u_c) v_i^2 \right] \quad (\text{A.27})$$

$$\leq \frac{1}{2} \left[\left| 1 + \frac{\Delta x_{pb}^p}{\Delta^2 + (y_{pb}^p)^2} \right| |\kappa(\theta)| v_i^2 - \frac{u_{d,i}}{u_{d,i}^2 + v_i^2} Y(u_i, u_c) v_i^2 + |F(\cdot)| \right] + \frac{1}{2} \left[\left| 1 + \frac{\Delta x_{pb}^p}{\Delta^2 + (y_{pb}^p)^2} \right| |\kappa(\theta)| (|u_i| + |u_j| + |v_j|) |v_i| \right] \quad (\text{A.28})$$

$$\leq |\kappa(\theta)| v_i^2 - \frac{u_{d,i}}{u_{d,i}^2 + v_i^2} Y(u_i, u_c) v_i^2 + |F(\cdot)| + |\kappa(\theta)| (|u_i| + |u_j| + |v_j|) |v_i|, \quad (\text{A.29})$$

where it has been used the following boundedness properties

$$\left[\left| 1 + \frac{\Delta x_{pb}^p}{\Delta^2 + (y_{pb}^p)^2} \right| \right] \leq 2. \quad (\text{A.30})$$

Remark A.1. To be able to have $|F(\cdot)|$ be upper bounded by a quadratic function of v , it is necessary to choose Δ dependent on x_{pb}^p in (4.38). However, contrary to Belleter et al. (2019), the lookahead distance (4.38) could be chosen independently of y_{pb}^p as the guidance law (4.39) does not include the ocean current compensation term g . The proof of this is found in Section A.2.1.

Substituting this into (A.16) gives

$$\begin{aligned} \dot{V} \leq & [|\kappa(\theta)| X(u_{d,i}, u_c) + Y(u_i, u_c)] v_i^2 + a_x \tilde{u}_i r_{d,i} v_i + X(u_{d,i}, u_c) \tilde{r}_i v_i + a_x \tilde{u}_i \tilde{r}_i v_i \\ & + Y(u_{d,i}, u_c) v_i^2 + a_y \tilde{u}_i v_i^2 - Y(u_{d,i}, u_c) v_c v_i - a_y \tilde{u}_i v_c v_i \end{aligned}$$

$$+ X(u_{d,i}, u_c) \left[|F(\cdot)| + |\kappa(\theta)| (|u_i| + |u_j| + |v_j|) \right] |v_i|. \quad (\text{A.31})$$

On the manifold where $(\tilde{X}_1, \tilde{X}_2) = \mathbf{0}$, (A.31) simplifies to

$$\begin{aligned} \dot{V} \leq & [|\kappa(\theta)|X_{\max} + Y_{\min}] v_i^2 \\ & + X(u_{d,i}, u_c) \left[F_1(\mathbf{0}, \mathbf{0}, \Delta, \theta, u_d, \dot{u}_d, v, v_c, u_v) + |\kappa(\theta)| (|u_i| + |u_j| + |v_j|) \right] |v_i|. \end{aligned} \quad (\text{A.32})$$

For sufficiently large v_i , it can be observed that the quadratic term in is dominant. Consequently, boundedness of (A.32) is guaranteed as long it is negative definite for sufficiently large v_i , that is

$$|\kappa(\theta)|X_{\max} + Y_{\min} < 0, \quad (\text{A.33})$$

which are true whenever the maximum curvature satisfies (4.77). As \dot{V} is negative for sufficiently large v_i , this implies that V decreases for sufficiently large v_i . Furthermore given the definition $V(v_i) = \frac{1}{2}v_i^2$, a decrease in V implies a decrease in v_i^2 and again in v_i . In other words, v_i cannot increase above a certain threshold because this will make the quadratic term of (A.32) dominant preventing further increase of v_i . Hence, v_i is bounded near the manifold where $(\tilde{X}_1, \tilde{X}_2) = \mathbf{0}$, concluding the proof of Lemma 4.3.

A.2.1 Importance of the choice of lookahead distance in Eq. (4.38)

The necessity for choosing Δ dependent on x_{pb}^p in (4.38) becomes evident from (A.20). If Δ is chosen independently of x_{pb}^p and y_{pb}^p , (A.20) reduces to

$$\begin{aligned} r_d v = & \kappa(\theta) v \left(\frac{1}{2} U_1 \cos(\chi_1 - \gamma_p) + \frac{1}{2} U_2 \cos(\chi_2 - \gamma_p) + \frac{k_\theta x_{pb}^p}{\sqrt{1 + (x_{pb}^p)^2}} \right) \\ & + \frac{\dot{u}_d}{u_d^2 + v^2} v^2 - \frac{u_d v}{u_d^2 + v^2} \left(X(u, u_c) r + Y(u, u_c) v - Y(u, u_c) v_c \right) \\ & - \frac{\Delta v}{\Delta^2 + (y_{pb}^p)^2} \left(-\frac{1}{2} (U_{d,1} + U_{d,2}) \frac{y_{pb}^p}{\sqrt{\Delta^2 + (y_{pb}^p)^2}} - \kappa(\theta) \dot{\theta} x_{pb}^p + G_1(\cdot) \right), \end{aligned} \quad (\text{A.34})$$

as the partial derivatives of Δ with respect to x_{pb}^p and y_{pb}^p in this case will be zero. Now, looking more closely at the term

$$v \frac{\Delta \kappa(\theta) \dot{\theta} x_{pb}^p}{\Delta^2 + (y_{pb}^p)^2}. \quad (\text{A.35})$$

Focusing on the vessel i . Inserting the expression for $\dot{\theta}$, and isolating the part independent of x_{pb}^p and depending on the part $U_{d,i}$:

$$v_i \frac{\Delta \kappa(\theta) x_{pb}^p}{\Delta^2 + (y_{pb}^p)^2} \frac{1}{2} U_i \cos(\chi_i - \gamma_p). \quad (\text{A.36})$$

As $U_i = \sqrt{u_i^2 + v_i^2}$, the growth of U_i is proportional with v_i , implying that the growth of (A.36) can be represented by

$$v_i^2 \frac{\Delta \kappa(\theta) x_{pb}^p}{\Delta^2 + (y_{pb}^p)^2}. \quad (\text{A.37})$$

If Δ is chosen independently of x_{pb}^p it is clear how this term will go to infinity for large values of x_{pb}^p . If Δ is chosen to grow at least linearly with x_{pb}^p then this term will go to a constant as

$$\lim_{x_{pb}^p \rightarrow \infty} \frac{\kappa(\theta) (x_{pb}^p)^2}{(x_{pb}^p)^2 + (y_{pb}^p)^2} = 1, \quad (\text{A.38})$$

or to zero if Δ grows more than linear in x_{pb}^p . Hence, if this would be the case, $r_d v$ could grow unbounded with x_{pb}^p making it impossible to show boundedness of the sway dynamics.

In Belleter et al. (2018) it was shown that the lookahead distance also needed to be chosen dependent on $y_{b/p}$, as a term that could grow unbounded in $y_{b/p}$ near the manifold where $g = -(y_{b/p} + 1)$ was shown to exist. However, since the proposed method in this thesis is based on absolute velocities, the extra term g , which was used to compensate for the ocean currents, is not present in the expression (A.20). Proving this is straight forward. Assume that Δ depends only on x_{pb}^p , then (A.20)

reduces to

$$\begin{aligned}
r_d v = & \kappa(\theta) v \left(\frac{1}{2} U_1 \cos(\chi_1 - \gamma_p) + \frac{1}{2} U_2 \cos(\chi_2 - \gamma_p) + \frac{k_\theta x_{pb}^p}{\sqrt{1 + (x_{pb}^p)^2}} \right) \\
& + \frac{\dot{u}_d}{u_d^2 + v^2} v^2 - \frac{u_d v}{u_d^2 + v^2} (X(u, u_c) r + Y(u, u_c) v - Y(u, u_c) v_c) \\
& - \frac{\Delta v}{\Delta^2 + (y_{pb}^p)^2} \left(-\frac{1}{2} (U_{d,1} + U_{d,2}) \frac{y_{pb}^p}{\sqrt{\Delta^2 + (y_{pb}^p)^2}} - \kappa(\theta) \dot{\theta} x_{pb}^p + G_1(\cdot) \right) \\
& + \frac{y_{pb}^p v}{\Delta^2 + (y_{pb}^p)^2} \left[\frac{\partial \Delta}{\partial x_{pb}^p} \left(-\frac{k_\theta x_{pb}^p}{\sqrt{1 + (x_{pb}^p)^2}} + \dot{\theta} \kappa(\theta) y_{pb}^p \right) \right]. \tag{A.39}
\end{aligned}$$

Using the same approach as earlier, the term

$$v \frac{\partial \Delta}{\partial x_{pb}^p} \kappa(\theta) \dot{\theta} \frac{(y_{pb}^p)^2}{\Delta^2 + (y_{pb}^p)^2} \tag{A.40}$$

may be isolated, which with the same reasoning as before reduces to

$$v_i^2 \frac{\partial \Delta}{\partial x_{pb}^p} \kappa(\theta) \frac{(y_{pb}^p)^2}{\Delta^2 + (y_{pb}^p)^2}. \tag{A.41}$$

It is clear how this term is bounded for all values of y_{pb}^p even if Δ depends only on x_{pb}^p . When comparing this to the term from Belleter et al. (2018):

$$\frac{v_r^2}{C_r} \frac{\partial \Delta}{\partial x_{b/p}} \kappa(\theta) \frac{\Delta y_{b/p} (y_{b/p} + g)}{(\Delta^2 + (y_{b/p} + g)^2)^{3/2}}, \tag{A.42}$$

it is clear how this could grow unbounded in $y_{b/p}$ near the manifold where $g = -(y_{b/p} + 1)$ as the term in this case would reduce to

$$\frac{v_r^2}{C_r} \frac{\partial \Delta}{\partial x_{b/p}} \kappa(\theta) \frac{\Delta y_{b/p}}{(\Delta^2 + 1)^{3/2}}, \tag{A.43}$$

which can only be bounded by choosing Δ dependent on $y_{b/p}$.

However, as the term (A.41) does not include the term g there are no manifold where it can grow unbounded in y_{pb}^p , implying the lookahead distance (4.38) could be chosen independently of y_{pb}^p .

A.3 Proof of Lemma 4.4

This proof follows along the lines of (Belleter et al.; 2018, Lemma 3).

Recall the sway dynamics (4.76e):

$$\begin{aligned} \dot{v}_i &= X(u_{d,i} + \tilde{u}_i, u_c)r_{d,i} + X(u_{d,i} + \tilde{u}_i, u_c)\tilde{r}_i \\ &\quad + Y(u_{d,i} + \tilde{u}_i, u_c)v_i - Y(u_{d,i} + \tilde{u}_i, u_c)v_c. \end{aligned} \quad (\text{A.44})$$

Considering the following Lyapunov function candidate $V(v_i) = \frac{1}{2}v_i^2$, whose time derivative along the solutions of (4.76e) is

$$\begin{aligned} \dot{V} &= v_i\dot{v}_i = X(u_{d,i} + \tilde{u}_i, u_c)r_{d,i}v_i + X(u_{d,i} + \tilde{u}_i, u_c)\tilde{r}_i v_i \\ &\quad + Y(u_{d,i} + \tilde{u}_i, u_c)v_i^2 - Y(u_{d,i} + \tilde{u}_i, u_c)v_c v_i \end{aligned} \quad (\text{A.45})$$

$$\begin{aligned} &\leq X(u_{d,i}, u_c)r_{d,i}v_i + a_x\tilde{u}_i r_{d,i}v_i + X(u_{d,i}, u_c)\tilde{r}_i v_i + a_x\tilde{u}_i\tilde{r}_i v_i \\ &\quad + Y(u_{d,i}, u_c)v_i^2 + a_y\tilde{u}_i v_i^2 - Y(u_{d,i}, u_c)v_c v_i - a_y\tilde{u}_i v_c v_i, \end{aligned} \quad (\text{A.46})$$

where the following fact, which can be concluded to hold for $X(u, u_c)$ and $Y(u, u_c)$ from Eqs. (C.2)–(C.3) is used:

$$X(u, u_c) = a_x u + b_x u_c + c_x \quad (\text{A.47})$$

$$Y(u, u_c) = a_y u + b_y u_c + c_y. \quad (\text{A.48})$$

Next, consider the term $r_{d,i}v_i$ using the expression for r_d in (4.74), omitting subscripts for simplicity

$$\begin{aligned} r_d v &= \kappa(\theta)\dot{\theta}v + \frac{\dot{u}_d}{u_d^2 + v^2}v^2 - \frac{u_d\dot{v}v}{u_d^2 + v^2} \\ &\quad - \frac{v}{\Delta^2 + (y_{pb}^p)^2} \left[\Delta \dot{y}_{pb}^p - y_{pb}^p \left(\frac{\partial \Delta}{\partial x_{pb}^p} \dot{x}_{pb}^p + \frac{\partial \Delta}{\partial y_{pb}^p} \dot{y}_{pb}^p \right) \right] \end{aligned} \quad (\text{A.49})$$

$$\begin{aligned}
&= \kappa(\theta)v \left(\frac{1}{2}U_1 \cos(\chi_1 - \gamma_p) + \frac{1}{2}U_2 \cos(\chi_2 - \gamma_p) + \frac{k_\theta x_{pb}^p}{\sqrt{1 + (x_{pb}^p)^2}} \right) \\
&\quad + \frac{\dot{u}_d}{u_d^2 + v^2} v^2 - \frac{u_d v}{u_d^2 + v^2} \left(X(u, u_c)r + Y(u, u_c)v - Y(u, u_c)v_c \right) \\
&\quad - \frac{\Delta v}{\Delta^2 + (y_{pb}^p)^2} \left(-\frac{1}{2}(U_{d,1} + U_{d,2}) \frac{y_{pb}^p}{\sqrt{\Delta^2 + (y_{pb}^p)^2}} - \kappa(\theta)\dot{\theta}x_{pb}^p + G_1(\cdot) \right) \\
&\quad + \frac{y_{pb}^p v}{\Delta^2 + (y_{pb}^p)^2} \left[\frac{\partial \Delta}{\partial x_{pb}^p} \left(-\frac{k_\theta x_{pb}^p}{\sqrt{1 + (x_{pb}^p)^2}} + \dot{\theta}\kappa(\theta)y_{pb}^p \right) \right. \\
&\quad \left. + \frac{\partial \Delta}{\partial y_{pb}^p} \left(-\frac{1}{2}(U_{d,1} + U_{d,2}) \frac{y_{pb}^p}{\sqrt{\Delta^2 + (y_{pb}^p)^2}} - \kappa(\theta)\dot{\theta}x_{pb}^p + G_1(\cdot) \right) \right]. \quad (\text{A.50})
\end{aligned}$$

Now, introduce a term $H(\tilde{\mathbf{X}}_1, \tilde{\mathbf{X}}_2, \Delta, \theta, u_d, \dot{u}_d, v, v_c, u_c, r)$ to collect all terms that have less than quadratic growth in v and/or vanish when $\tilde{\mathbf{X}}_2 = 0$.

$$\begin{aligned}
r_d v &= \kappa(\theta)v \left[1 + \frac{x_{pb}^p}{\Delta^2 + (y_{pb}^p)^2} \right] \left(\frac{1}{2}U_1 \cos(\chi_1 - \gamma_p) + \frac{1}{2}U_2 \cos(\chi_2 - \gamma_p) \right) \\
&\quad - \frac{\Delta v}{\Delta^2 + (y_{pb}^p)^2} \left(-\frac{1}{2}(U_{d,1} + U_{d,2}) \frac{y_{pb}^p}{\sqrt{\Delta^2 + (y_{pb}^p)^2}} + G_1(\cdot) \right) \\
&\quad - \frac{\Delta y_{pb}^p}{\Delta^2 + (y_{pb}^p)^2} \frac{\partial \Delta}{\partial y_{pb}^p} \left(-\frac{1}{2}(U_{d,1} + U_{d,2}) \frac{y_{pb}^p}{\sqrt{\Delta^2 + (y_{pb}^p)^2}} + G_1(\cdot) \right) \\
&\quad - \frac{u_d}{u_d^2 + v^2} Y(u, u_c)v^2 + H(\cdot) \quad (\text{A.51})
\end{aligned}$$

where

$$\begin{aligned}
H(\cdot) = v & \left[\kappa(\theta) \frac{k_\theta x_{pb}^p}{\sqrt{1 + (x_{pb}^p)^2}} + \frac{\dot{u}_d v}{u_d^2 + v^2} - \frac{u_d v}{u_d^2 + v^2} (X(u, u_c)r - Y(u, u_c)v_c) \right. \\
& \left. + \frac{\Delta}{\Delta^2 + (y_{pb}^p)^2} \kappa(\theta) \frac{k_\theta (x_{pb}^p)^2}{\sqrt{1 + (x_{pb}^p)^2}} - \frac{y_{pb}^p}{\Delta^2 + (y_{pb}^p)^2} \frac{\partial \Delta}{\partial x_{pb}^p} \frac{k_\theta x_{pb}^p}{\sqrt{1 + (x_{pb}^p)^2}} \right]. \quad (\text{A.52})
\end{aligned}$$

Similarly to Section A.2, all terms with partial derivatives of Δ and $\dot{\theta}$ are cancelled due to skew-symmetry due to the choice of lookahead distance (4.38). Consequently, the term $r_d v$ may be upper bounded as

$$\begin{aligned}
r_{d,i} v_i & \leq |v_i| \left| \left[1 + \frac{\Delta x_{pb}^p}{\Delta^2 + (y_{pb}^p)^2} \right] \right| |\kappa(\theta)| \frac{1}{2} (|U_i| + |U_j|) \\
& + |v_i| \left| \frac{1}{\Delta} \right| \frac{1}{2} (|U_{d,i}| + |U_{d,j}| + |G_1(\cdot)|) \\
& + |v_i| \left| \frac{y_{pb}^p}{\Delta^2 + (y_{pb}^p)^2} \right| \frac{1}{2} (|U_{d,i}| + |U_{d,j}| + |G_1(\cdot)|) \\
& - \frac{u_{d,i}}{u_{d,i}^2 + v_i^2} Y(u_i, u_c) v_i^2 + |H(\cdot)|. \quad (\text{A.53})
\end{aligned}$$

Next, substituting the following inequalities

$$\left| \frac{y_{pb}^p}{\Delta^2 + (y_{pb}^p)^2} \right| \leq \left| \frac{1}{\Delta} \right| \quad (\text{A.54})$$

$$|U_{d,i}| \leq 4(|u_i| + |v_i| + |\tilde{u}_i|), \quad (\text{A.55})$$

the bound on $r_d v$ in (A.53) may further be given as

$$r_{d,i} v_i \leq \frac{1}{2} v_i^2 \left| \left[1 + \frac{\Delta x_{pb}^p}{\Delta^2 + (y_{pb}^p)^2} \right] \right| |\kappa(\theta)| + \frac{1}{2} |v_i| \left| \left[1 + \frac{\Delta x_{pb}^p}{\Delta^2 + (y_{pb}^p)^2} \right] \right| |\kappa(\theta)| |u_i|$$

$$\begin{aligned}
& + \frac{1}{2}|v_i| \left| \left| 1 + \frac{\Delta x_{pb}^p}{\Delta^2 + (y_{pb}^p)^2} \right| \right| |\kappa(\theta)| |U_j| - \frac{u_{d,i}}{u_{d,i}^2 + v_i^2} Y(u_i, u_c) v_i^2 + |H(\cdot)| \\
& + |v_i| \left| \frac{2}{\Delta} \right| \left(2(|u_i| + |v_i|) + \frac{1}{2}|\tilde{u}_i| + 2(|u_j| + |v_j|) + \frac{1}{2}|\tilde{u}_j| + |G_1(\cdot)| \right) \quad (\text{A.56})
\end{aligned}$$

$$\leq v_i^2 \left[\frac{1}{2} |\kappa(\theta)| \left| \left| 1 + \frac{\Delta x_{pb}^p}{\Delta^2 + (y_{pb}^p)^2} \right| \right| + \frac{4}{\Delta} \right] - \frac{u_{d,i}}{u_{d,i}^2 + v_i^2} Y(u_i, u_c) v_i^2 + \Phi(\cdot) \quad (\text{A.57})$$

$$\leq v_i^2 \left[|\kappa(\theta)| + \frac{4}{\Delta} \right] - \frac{u_{d,i}}{u_{d,i}^2 + v_i^2} Y(u_i, u_c) v_i^2 + \Phi(\cdot), \quad (\text{A.58})$$

where the inequality (A.30) is used, and the function $\Phi(\cdot)$ is introduced to collect the remaining terms that have less than quadratic growth in v_i and/or vanish when $\tilde{\mathbf{X}}_2 = 0$. From the definitions of $\Phi(\cdot)$ and $H(\cdot)$ it is obvious that there exists some positive bounded functions $F_{0,2}(\tilde{\mathbf{X}}_1, \tilde{\mathbf{X}}_2, \Delta, \theta, u_d, \dot{u}_d, v, v_c, u_c, r)$ such that

$$\Phi(\cdot) \leq F_2(\cdot) v_i^2 + F_2(\cdot) |v_i| + F_0(\cdot), \quad (\text{A.59})$$

with

$$F_2(\tilde{\mathbf{X}}_1, \mathbf{0}, \Delta, \theta, u_d, \dot{u}_d, v, v_c, u_c, r) = 0. \quad (\text{A.60})$$

Hence, substituting the bound (A.58) into (A.46), the following bound for the Lyapunov function candidate derivative is obtained

$$\begin{aligned}
\dot{V} & \leq X(u_{d,i}, u_c) \left(\left[|\kappa(\theta)| + \frac{4}{\Delta} \right] v_i^2 + \Phi(\cdot) \right) + a_x \tilde{u}_i r_{d,i} v_i + X(u_{d,i}, u_c) \tilde{r}_i v_i + a_x \tilde{u}_i \tilde{r}_i v_i \\
& + Y(u_{d,i}, u_c) v_i^2 + a_y \tilde{u}_i v_i^2 - Y(u_{d,i}, u_c) v_c v_i - a_y \tilde{u}_i v_c v_i - \frac{u_{d,i}}{u_{d,i}^2 + v_i^2} Y(u_i, u_c) v_i^2
\end{aligned} \quad (\text{A.61})$$

$$\begin{aligned}
& \leq \left(X(u_{d,i}, u_c) \left[|\kappa(\theta)| + \frac{4}{\Delta} \right] - Y(u_{d,i}, u_c) \right) v_i^2 + a_x \tilde{u}_i r_{d,i} v_i + X(u_{d,i}, u_c) \tilde{r}_i v_i + a_x \tilde{u}_i \tilde{r}_i v_i \\
& + a_y \tilde{u}_i v_i^2 - Y(u_{d,i}, u_c) v_c v_i - a_y \tilde{u}_i v_c v_i + X(u_{d,i}, u_c) \Phi(\cdot). \quad (\text{A.62})
\end{aligned}$$

On the manifold where $\tilde{\mathbf{X}}_2 = 0$, the following bound is obtained

$$\begin{aligned}
\dot{V} & \leq \left(X_{\max} \left[\kappa_{\max} + \frac{4}{\Delta} \right] - Y_{\min} \right) v_i^2 \\
& + X(u_{d,i}, u_c) \left(F_1(\tilde{\mathbf{X}}_1, \mathbf{0}, \Delta, \theta, u_d, \dot{u}_d, v, v_c, u_c, r) |v_i| \right. \\
& \left. + F_0(\tilde{\mathbf{X}}_1, \mathbf{0}, \Delta, \theta, u_d, \dot{u}_d, v, v_c, u_c, r) \right). \quad (\text{A.63})
\end{aligned}$$

For sufficiently large v_i , it can be observed that the quadratic term is dominant. Hence, boundedness of v_r near the manifold $\tilde{X}_2 = 0$ is guaranteed whenever the following condition holds

$$X_{\max} \left[\kappa_{\max} + \frac{4}{\Delta} \right] - Y_{\min} < 0, \quad (\text{A.64})$$

such that the quadratic term is negative definite. Using the lookahead distance definition (4.38), it can be seen that this condition is fulfilled whenever

$$\mu > \frac{4X_{\max}}{Y_{\min} - \kappa_{\max}X_{\max}}. \quad (\text{A.65})$$

Furthermore, observe how this is well defined as the denominator is nonzero and positive whenever the condition from Lemma 4.3 is satisfied. As \dot{V} is negative definite for sufficiently large magnitudes of v_i near the manifold $\tilde{X}_2 = 0$, the Lyapunov function candidate $V(v_i) = \frac{1}{2}v_i^2$ must decrease for sufficiently large v_i , and by extension, the magnitude of v_i must decrease for sufficiently large v_i . Hence, v_i is bounded near the manifold where $\tilde{X}_2 = 0$ if the constant part of the lookahead distance μ is chosen accordingly to the condition in Lemma 4.4.

B | Derivations of expressions

In this appendix, thorough derivations of various expressions throughout the thesis are presented. The derivations are left out in their respective locations throughout the thesis for readability, and instead given here in their full length.

B.1 Derivations of Eq. (4.30)

This sections presents the derivations of (4.30). Taking the time derivative of (4.29a) gives

$$\begin{aligned} \dot{x}_{pb}^p &= (\dot{x}_b - \dot{x}_p) \cos \gamma_p - (x_b - x_p) \dot{\gamma}_p \sin \gamma_p \\ &\quad + (\dot{y}_b - \dot{y}_p) \sin \gamma_p + (y_b - y_p) \dot{\gamma}_p \cos \gamma_p. \end{aligned} \quad (\text{B.1})$$

Using the fact that $\dot{\gamma}_p = \kappa(\theta)\dot{\theta}$, and by inserting the barycenter kinematics (4.28), the above equation may be rearranged to

$$\begin{aligned} \dot{x}_{pb}^p &= \dot{x}_b \cos \gamma_p - \dot{x}_p \cos \gamma_p + \dot{y}_b \sin \gamma_p - \dot{y}_p \sin \gamma_p \\ &\quad + \kappa(\theta)\dot{\theta} [(y_b - y_p) \sin \gamma_p - (x_b - x_p) \cos \gamma_p] \end{aligned} \quad (\text{B.2})$$

$$\begin{aligned} &= \frac{1}{2} \left[u_1 \cos \psi_1 - v_1 \sin \psi_1 + u_2 \cos \psi_2 - v_2 \sin \psi_2 \right] \cos \gamma_p \\ &\quad + \frac{1}{2} \left[u_1 \sin \psi_1 + v_1 \cos \psi_1 + u_2 \sin \psi_2 + v_2 \cos \psi_2 \right] \sin \gamma_p \\ &\quad + \kappa(\theta)\dot{\theta} y_{pb}^p - \dot{x}_p \cos \gamma_p - \dot{y}_p \sin \gamma_p. \end{aligned} \quad (\text{B.3})$$

Next, it is known that the kinematics of vessel i may be expressed in terms of the total speed $U = \sqrt{u^2 + v^2}$ and the course χ_i as

$$u_i \cos \psi_i - v_i \sin \psi_i = U_i \cos \chi_i \quad (\text{B.4})$$

$$u_i \sin \psi_i + v_i \cos \psi_i = U_i \sin \chi_i. \quad (\text{B.5})$$

Furthermore, by taking a closer look at the two last terms in (B.3) it can be observed that $\dot{x}_p \cos \gamma_p + \dot{y}_p \sin \gamma_p$ represents the movement of \mathbf{p}_p along the path, and thus is equal to $\dot{\theta}$. Thus, (B.3) may be further simplified to

$$\begin{aligned} \dot{x}_{pb}^p &= \frac{1}{2} \left[U_1 \cos \chi_1 + U_2 \cos \chi_2 \right] \cos \gamma_p \\ &\quad + \frac{1}{2} \left[U_1 \sin \chi_1 + U_2 \sin \chi_2 \right] \sin \gamma_p - \dot{\theta} \left(1 - \kappa(\theta) \dot{\theta} y_{pb}^p \right) \end{aligned} \quad (\text{B.6})$$

$$= \frac{1}{2} U_1 \cos (\chi_1 - \gamma_p) + \frac{1}{2} U_2 \cos (\chi_2 - \gamma_p) - \dot{\theta} (1 - \kappa(\theta) y_{pb}^p), \quad (\text{B.7})$$

where the trigonometric sum formula has been used to obtain the last equation, which is the expression given in (4.30a). Similarly, the cross-track error dynamics are obtained by taking the time derivative of (4.29b)

$$\begin{aligned} \dot{y}_{pb}^p &= -(\dot{x}_b - \dot{x}_p) \sin \gamma_p - (x_b - x_p) \dot{\gamma}_p \cos \gamma_p \\ &\quad + (\dot{y}_b - \dot{y}_p) \cos \gamma_p - (y_b - y_p) \dot{\gamma}_p \sin \gamma_p \end{aligned} \quad (\text{B.8})$$

$$\begin{aligned} &= -\dot{x}_b \sin \gamma_p + \dot{x}_p \sin \gamma_p + \dot{y}_b \cos \gamma_p - \dot{y}_p \cos \gamma_p \\ &\quad - \kappa(\theta) \dot{\theta} \left[(x_b - x_p) \cos \gamma_p + (y_b - y_p) \sin \gamma_p \right] \end{aligned} \quad (\text{B.9})$$

$$\begin{aligned} &= -\dot{x}_b \sin \gamma_p + \dot{y}_b \cos \gamma_p - \kappa(\theta) \dot{\theta} x_{pb}^p \\ &\quad + \dot{x}_p \sin \gamma_p - \dot{y}_p \cos \gamma_p. \end{aligned} \quad (\text{B.10})$$

Again, take a closer look at the last two terms. While they in (B.3) represented the movement of \mathbf{p}_p along the path, the two last terms in (B.10) represents the movement of \mathbf{p}_p perpendicular to the path. As \mathbf{p}_p is obviously on the path at all times by definition, these terms are equal to zero. Next, by inserting the barycenter kinematics, and performing the same rearrangements as for the along-path error dynamics, the following expression is obtained

$$\begin{aligned} \dot{y}_{pb}^p &= -\frac{1}{2} \left[u_1 \cos \psi_1 - v_1 \sin \psi_1 + u_2 \cos \psi_2 - v_2 \sin \psi_2 \right] \sin \gamma_p \\ &\quad + \frac{1}{2} \left[u_1 \sin \psi_1 + v_1 \cos \psi_1 + u_2 \sin \psi_2 + v_2 \cos \psi_2 \right] \cos \gamma_p \\ &\quad - \kappa(\theta) \dot{\theta} x_{pb}^p \end{aligned} \quad (\text{B.11})$$

$$\begin{aligned} &= -\frac{1}{2} \left[U_1 \cos \chi_1 + U_2 \cos \chi_2 \right] \sin \gamma_p \\ &\quad + \frac{1}{2} \left[U_1 \sin \chi_1 + U_2 \sin \chi_2 \right] \cos \gamma_p - \kappa(\theta) \dot{\theta} x_{pb}^p \end{aligned} \quad (\text{B.12})$$

$$= \frac{1}{2} U_1 \sin (\chi_1 - \gamma_p) + \frac{1}{2} U_2 \sin (\chi_2 - \gamma_p) - \kappa(\theta) \dot{\theta} x_{pb}^p, \quad (\text{B.13})$$

which is identical to (4.30b).

B.2 Derivations of Eq. (4.41)

This section presents the derivations of (4.41). First, rewriting the trigonometric terms of (4.30b) as, omitting subscripts

$$U \sin(\chi - \gamma_p) = U \sin(\psi + \beta - \gamma_p) \quad (\text{B.14})$$

$$= U [\sin(\psi - \gamma_p) \cos \beta + \cos(\psi - \gamma_p) \sin \beta]. \quad (\text{B.15})$$

$$= u \sin(\psi - \gamma_p) + v \cos(\psi - \gamma_p) \quad (\text{B.16})$$

$$= [u_d + \tilde{u}] \sin(\psi - \gamma_p) + v \cos(\psi - \gamma_p), \quad (\text{B.17})$$

where the total speed U was be decomposed into the surge and sway speed through the crab angle. Next, a trick is performed by converting the first sinusoidal term and the cosinusoidal term into amplitude-phase form by using the following trigonometric identities

$$A \sin(\omega t) + B \cos(\omega t) = C \sin(\omega t + \phi) \quad (\text{B.18a})$$

$$C = \sqrt{A^2 + B^2} \quad (\text{B.18b})$$

$$\phi = \arctan\left(\frac{B}{A}\right). \quad (\text{B.18c})$$

Here, $A = u_d$, $B = v$ giving $\phi = \arctan\left(\frac{v}{u_d}\right) = \beta_d$ and $C = \sqrt{u_d^2 + v^2} = U_d$, where β_d is the desired crab angle. Thus, (B.17) may be written as

$$U \sin(\chi - \gamma_p) = U_d \sin(\psi + \beta_d - \gamma_p) + \tilde{u} \sin(\psi - \gamma_p) \quad (\text{B.19})$$

$$= U_d \sin(\psi_d + \tilde{\psi} + \beta_d - \gamma_p) + \tilde{u} \sin(\psi - \gamma_p). \quad (\text{B.20})$$

Using (B.20), (4.30b) can be written as

$$\begin{aligned} \dot{y}_{pb}^p &= \frac{1}{2} U_{d,1} \sin(\psi_{d,1} + \tilde{\psi}_1 + \beta_{d,1} - \gamma_p) \\ &\quad + \frac{1}{2} U_{d,2} \sin(\psi_{d,2} + \tilde{\psi}_2 + \beta_{d,2} - \gamma_p) \\ &\quad - \kappa(\theta) \dot{\theta} x_{pb}^p \\ &\quad + \frac{1}{2} \tilde{u}_1 \sin(\psi_1 - \gamma_p) + \frac{1}{2} \tilde{u}_2 \sin(\psi_2 - \gamma_p), \end{aligned} \quad (\text{B.21})$$

which is identical to (4.40). Then, substituting the guidance law (4.39) into the first term of (B.20), again omitting subscript indexes

$$U_d \sin(\psi_d + \tilde{\psi} + \beta_d - \gamma_p) = U_d \sin\left(-\arctan\left(\frac{y_{pb}^p}{\Delta}\right) + \tilde{\psi}\right) \quad (\text{B.22})$$

$$\begin{aligned} &= U_d \left[\sin\left(-\arctan\left(\frac{y_{pb}^p}{\Delta}\right)\right) \cos \tilde{\psi} + \cos\left(-\arctan\left(\frac{y_{pb}^p}{\Delta}\right)\right) \sin \tilde{\psi} \right] \\ &+ U_d \sin\left(-\arctan\left(\frac{y_{pb}^p}{\Delta}\right)\right) - U_d \sin\left(-\arctan\left(\frac{y_{pb}^p}{\Delta}\right)\right). \end{aligned} \quad (\text{B.23})$$

Further, by inserting the trigonometric identity

$$\sin\left(\arctan\left(\frac{x}{y}\right)\right) = \frac{x}{\sqrt{x^2 + y^2}}, \quad (\text{B.24})$$

into (B.23) the following expression is obtained

$$\begin{aligned} U_d \sin(\psi_d + \tilde{\psi} + \beta_d - \gamma_p) &= -U_d \sin(\psi_{d,1} + \tilde{\psi}_1 + \beta_{d,1} - \gamma_p) \\ &- \kappa(\theta) \dot{\theta} x_{pb}^p + G_2(\tilde{\psi}, \tilde{u}, \psi_d, U_d, y_{pb}^p), \end{aligned} \quad (\text{B.25})$$

with

$$\begin{aligned} G_2(\tilde{\psi}, \tilde{u}, \psi_d, U_d, y_{pb}^p) &= U_d \left(1 - \cos \tilde{\psi}\right) \sin\left(\arctan\left(\frac{y_{pb}^p}{\Delta}\right)\right) + \tilde{u} \sin(\psi - \gamma_p) \\ &+ U_d \cos\left(\arctan\left(\frac{y_{pb}^p}{\Delta}\right)\right) \sin \tilde{\psi}. \end{aligned} \quad (\text{B.26})$$

Inserting (B.25) into (B.21) gives the expression given in (4.41)

$$\begin{aligned} \dot{y}_{pb}^p &= -\frac{1}{2} (U_{d,1} + U_{d,2}) \frac{y_{pb}^p}{\sqrt{\Delta^2 + (y_{pb}^p)^2}} \\ &- \kappa(\theta) \dot{\theta} x_{pb}^p + G_1(\tilde{\psi}_1, \tilde{u}_1, \psi_{d,1}, U_{d,1}, \tilde{\psi}_2, \tilde{u}_2, \psi_{d,2}, U_{d,2}, y_{pb}^p), \end{aligned} \quad (\text{B.27})$$

with

$$G_1(\cdot) = \frac{1}{2} G_2(\tilde{\psi}_1, \tilde{u}_1, \psi_{d,1}, U_{d,1}, y_{pb}^p) + \frac{1}{2} G_2(\tilde{\psi}_2, \tilde{u}_2, \psi_{d,2}, U_{d,2}, y_{pb}^p). \quad (\text{B.28})$$

B.3 Derivations of Eq. (4.64)

To find an expression for the closed-loop error dynamics for the formation task function, start with the differential relationship (4.3)

$$\dot{\boldsymbol{\sigma}} = \mathbf{J}_f \mathbf{v} \quad (\text{B.29})$$

$$= \mathbf{J}_f (\mathbf{v}_d + \tilde{\mathbf{v}}). \quad (\text{B.30})$$

Then, inserting the CLIK control law (4.5) gives (4.63)

$$\dot{\boldsymbol{\sigma}} = -\Lambda \tilde{\boldsymbol{\sigma}} - \mathbf{J}_f \tilde{\mathbf{v}}. \quad (\text{B.31})$$

Next, the perturbing term will be expressed as a function of the error states of the autopilots (4.60). It is known that the velocity vector may be expressed using the total speed and the course of the vessel, omitting vessel indexes

$$\mathbf{v} = \begin{bmatrix} U \cos(\chi) \\ U \sin(\chi) \end{bmatrix}, \quad (\text{B.32})$$

and similarly, the desired velocity may be expressed by substituting the total speed and course with the desired total speed and course respectively. The velocity error $\tilde{\mathbf{v}}$ may therefore be expressed as

$$\tilde{\mathbf{v}} = \begin{bmatrix} U_1 \cos(\chi_1) - U_{d,1} \cos(\chi_{d,1}) \\ U_1 \sin(\chi_1) - U_{d,1} \sin(\chi_{d,1}) \\ U_2 \cos(\chi_2) - U_{d,2} \cos(\chi_{d,2}) \\ U_2 \sin(\chi_2) - U_{d,2} \sin(\chi_{d,2}) \end{bmatrix} \quad (\text{B.33})$$

Now, consider the x components of (B.33), omitting vessel indexes. Using (B.5), they can be expressed using the surge and sway speed of the vessel

$$U \cos(\chi) - U_d \cos(\chi_d) = u \cos(\psi_d + \tilde{\psi}) - v \sin(\psi_d + \tilde{\psi}) \\ - (u_d \cos \psi_d - v \sin \psi_d) \quad (\text{B.34})$$

$$= (u_d + \tilde{u}) \left[\cos \psi_d \cos \tilde{\psi} - \sin \psi_d \sin \tilde{\psi} \right] \\ + v \left[\sin \psi_d \cos \tilde{\psi} - \cos \psi_d \sin \tilde{\psi} \right] \\ - (u_d \cos \psi_d - v \sin \psi_d) \quad (\text{B.35})$$

$$\begin{aligned}
&= \tilde{u} \cos \psi_d \cos \tilde{\psi} - \tilde{u} \sin \psi_d \sin \tilde{\psi} \\
&\quad - (u_d \cos \psi_d - v \sin \psi_d) (1 - \cos \tilde{\psi}) \\
&\quad - (u_d \sin \psi_d + v \cos \psi_d) \sin \tilde{\psi} \tag{B.36}
\end{aligned}$$

Next, the middle two lines of the last expression is transformed into amplitude-phase form by using (B.18c) and the corresponding trigonometric identities for cosine

$$A \cos(\omega t) + B \sin(\omega t) = C \cos(\omega t - \phi) \tag{B.37a}$$

$$C = \sqrt{A^2 + B^2} \tag{B.37b}$$

$$\phi = \arctan\left(-\frac{B}{A}\right). \tag{B.37c}$$

$$\begin{aligned}
U \cos(\chi) - U_d \cos(\chi_d) &= \tilde{u} \cos \psi_d \cos \tilde{\psi} - \tilde{u} \sin \psi_d \sin \tilde{\psi} \\
&\quad + U_d \cos(\psi_d + \beta_d) (1 - \cos \tilde{\psi}) \\
&\quad - U_d \sin(\psi_d + \beta_d) \sin \tilde{\psi} \tag{B.38}
\end{aligned}$$

$$= G_3(\tilde{\psi}, \tilde{u}, \psi_d, U_d, \beta_d). \tag{B.39}$$

By repeating the process for the y components of (B.33)

$$\begin{aligned}
U \sin(\chi) - U_d \sin(\chi_d) &= u \sin(\psi_d + \tilde{\psi}) + v \cos(\psi_d + \tilde{\psi}) \\
&\quad - (u_d \sin \psi_d + v \cos \psi_d) \tag{B.40}
\end{aligned}$$

$$\begin{aligned}
&= (u_d + \tilde{u}) \left[\sin \psi_d \cos \tilde{\psi} - \cos \psi_d \sin \tilde{\psi} \right] \\
&\quad + v \left[\cos \psi_d \cos \tilde{\psi} - \sin \psi_d \sin \tilde{\psi} \right] \\
&\quad - (u_d \sin \psi_d + v \cos \psi_d) \tag{B.41}
\end{aligned}$$

$$\begin{aligned}
&= \tilde{u} \sin \psi_d \cos \tilde{\psi} + \tilde{u} \cos \psi_d \sin \tilde{\psi} \\
&\quad - (u_d \sin \psi_d + v \cos \psi_d) (1 - \cos \tilde{\psi}) \\
&\quad + (u_d \cos \psi_d - v \sin \psi_d) \sin \tilde{\psi} \tag{B.42}
\end{aligned}$$

$$\begin{aligned}
&= \tilde{u} \sin \psi_d \cos \tilde{\psi} + \tilde{u} \cos \psi_d \sin \tilde{\psi} \\
&\quad - U_d \sin(\psi_d + \beta_d) (1 - \cos \tilde{\psi}) \\
&\quad - U_d \cos(\psi_d + \beta_d) \sin \tilde{\psi} \tag{B.43}
\end{aligned}$$

$$= G_4(\tilde{\psi}, \tilde{u}, \psi_d, U_d, \beta_d). \tag{B.44}$$

The velocity error (B.33) may therefore be expressed accordingly to (4.64)

$$\dot{\tilde{\sigma}} = -\Lambda\tilde{\sigma} - \mathbf{J}_f \begin{bmatrix} G_3 \left(\tilde{\psi}_1, \tilde{\mathbf{u}}_1, \psi_{d,1}, u_{d,1}, v_1 \right) \\ G_4 \left(\tilde{\psi}_1, \tilde{\mathbf{u}}_1, \psi_{d,1}, u_{d,1}, v_1 \right) \\ G_3 \left(\tilde{\psi}_2, \tilde{\mathbf{u}}_2, \psi_{d,2}, u_{d,2}, v_2 \right) \\ G_4 \left(\tilde{\psi}_2, \tilde{\mathbf{u}}_2, \psi_{d,2}, u_{d,2}, v_2 \right) \end{bmatrix}, \quad (\text{B.45})$$

with the expressions for $G_{3,4}(\cdot)$ given in (B.39) and (B.44) respectively.

C | Vessel model expressions

$$\boldsymbol{\phi}_u^T(\psi, r) = \begin{bmatrix} -\frac{d_{11}+2d_{11}^q u}{m_{11}} \cos(\psi) - \frac{m_{11}^A - m_{22}^A}{m_{11}} r \sin(\psi) \\ -\frac{d_{11}+2d_{11}^q u}{m_{11}} \sin(\psi) + \frac{m_{11}^A - m_{22}^A}{m_{11}} r \cos(\psi) \\ -d_{11}^q \cos^2(\psi) \\ -d_{11}^q \sin^2(\psi) \\ -2d_{11}^q \cos(\psi) \sin(\psi) \end{bmatrix} \quad (\text{C.1})$$

$$X(u, u_c) = \frac{1}{\Gamma} \left(m_{33} \left(-d_{23} - m_{11}(u - u_c) - m_{11}^{RB} u_c \right) + m_{23} d_{33} + m_{23} \left(m_{23}(u - u_c) + m_{23}^{RB} u_c + m_{22}^A u_c \right) \right) \quad (\text{C.2})$$

$$Y(u, u_c) = \frac{1}{\Gamma} \left(-m_{33} d_{22} + m_{23} d_{32} + m_{23} \left(m_{22}^A - m_{11}^A \right) (u - u_c) \right) \quad (\text{C.3})$$

$$F_r(u, v, r) = \frac{m_{22}}{\Gamma} \left(-(m_{22}v - m_{23}r) u + m_{11}uv - d_{32}v - d_{33}r \right) - \frac{m_{23}}{\Gamma} \left(-m_{11}ru - d_{22}v - d_{23}r \right) \quad (\text{C.4})$$

where, $\Gamma = m_{22}m_{33} - m_{23}^2 > 0$. Further, the function $\boldsymbol{\phi}_r^T(u, v, r, \psi) = [\phi_{r1} \ \dots \ \phi_{r5}]$ is given by

$$\begin{bmatrix} \phi_{r1} \\ \phi_{r2} \end{bmatrix} = \begin{bmatrix} \cos(\psi) & -\sin(\psi) \\ \sin(\psi) & \cos(\psi) \end{bmatrix} \begin{bmatrix} a_1 \\ a_2 \end{bmatrix} \quad (\text{C.5})$$

$$\phi_{r3} = -\frac{m_{22}}{\Gamma} \left(m_{11}^A - m_{22}^A \right) \cos(\psi) \sin(\psi) \quad (\text{C.6})$$

$$\phi_{r4} = \frac{m_{22}}{\Gamma} \left(m_{11}^A - m_{22}^A \right) \cos(\psi) \sin(\psi) \quad (\text{C.7})$$

$$\phi_{r5} = \frac{m_{22}}{\Gamma} \left(m_{11}^A - m_{22}^A \right) (1 - 2 \sin^2(\psi)) \quad (\text{C.8})$$

where

$$a_1 = \frac{m_{22}}{\Gamma} \left((m_{11}^A - m_{22}^A) v + (m_{23}^A - m_{22}^A) r \right) - \frac{m_{23}}{\Gamma} m_{11}^A r \quad (\text{C.9})$$

$$a_2 = \frac{m_{22}}{\Gamma} \left(d_{32} - (m_{11}^A - m_{22}^A) u \right) - \frac{m_{23}}{\Gamma} d_{22}. \quad (\text{C.10})$$

